

NORTHWESTERN UNIVERSITY

Investigating Functional Extension of Optical Coherence Tomography for
Spectroscopic Analysis of Blood Oxygen Saturation

A DISSERTATION

SUBMITTED TO THE GRADUATE SCHOOL
IN PARTIAL FULFILLMENT OF THE REQUIREMENTS

for the degree

DOCTOR OF PHILOSOPHY

Field of Biomedical Engineering

By

Siyu Chen

EVANSTON, ILLINOIS

June 2017

© Copyright by Siyu Chen 2017
All Rights Reserved

Abstract

Investigating Functional Extension of Optical Coherence Tomography for Spectroscopic Analysis of Blood Oxygen Saturation

Siyu Chen

Over the past two decades, optical coherence tomography (OCT) has been successfully applied to various fields of biomedical researching and clinical studies, including cardiology, urology, dermatology, dentistry, oncology, and most successfully, ophthalmology. This dissertation seeks to extend the current OCT practice, which is still largely morphology-based, into a new dimension, functional analysis of metabolic activities *in vivo*. More specifically, the investigation is focused on retrieving blood oxygen saturation (sO_2) using intrinsic hemoglobin optical absorption contrast.

Most mammalian cells rely on aerobic respiration to support cellular function, which means they consume oxygen to create adenosine triphosphate (ATP). Metabolic rate of oxygen (MRO_2), a key hemodynamic parameter, characterizes how much oxygen is consumed during a given period of time, reflecting the metabolic activity of the target tissue. For example, retinal neurons are highly active and almost entirely rely on the moment-to-moment oxygen supply from retinal

circulations. Thus, variation in MRO_2 reveals the instantaneous activity of these neurons, shedding light on the physiological and pathophysiological change of cellular functions. Eventually, measuring MRO_2 can potentially provide a biomarker for early-stage disease diagnosis, and serve as one benchmark for evaluating effectiveness of medical intervention during disease management.

Essential in calculating MRO_2 , blood sO_2 measurements using spectroscopic OCT analysis has been attempted as early as 2003. OCT is intrinsically sensitive to the blood optical absorption spectrum due to its wide-band illumination and detection scheme relying on back-scattered photon. However, accurate retrieval of blood sO_2 using conventional near infrared (NIR) OCT systems *in vivo* has remained challenging. It was not until the development of OCT systems using visible light illumination (vis-OCT) when accurate measurement of blood sO_2 was reported in live animals *in situ*. Thus, one question demanding immediate investigation is how the choice of illumination wavelength bands affect the performance of OCT oximetry. This is addressed using two approaches, (1) a numerical study using Monte Carlo methods, and (2) animal experiments involving the development of a vis- and NIR- dual band OCT imaging system. It is indicated that visible light is more suitable for OCT oximetry applications due to the higher absorption contrast between oxyhemoglobin and deoxyhemoglobin. The accuracy of OCT retinal oximetry is established to be around 5 percentage points (pp) regardless of physiological variation of blood sO_2 , vessel diameter, and is robust over a reasonable selection of sampling geometry. Despite the higher optical scattering experienced in the visible wavelength range, vis-OCT also demonstrated comparable or better imaging capability in terms of resolving anatomical features, imaging resolution, and retrieving other functional indicators such as blood flow.

Besides retrieving blood sO_2 from vessels directly visualized in structural OCT images, the possibility of using dynamic motion contrast to enhance otherwise non-resolvable micro vessels is investigated. Using this approach, it is subsequently proved that OCT angiography (OCTA) encodes blood absorption contrast and can be used to calculate sO_2 within microvasculature. For the first time, measurements of relative sO_2 change are reported in choroidal capillaries following inhalation oxygen challenge.

This dissertation also represents a translational study that seeks to move technologies developed in the laboratory into real clinical applications. A vis-OCT imaging system with integrated scanning laser ophthalmoscope (SLO) is developed for human subjects. This prototype system can provide three-dimensional (3D) structural images and cross-sections of human fundus similar to that from commercial NIR-OCT systems. In addition, blood sO_2 within retinal circulation is successfully retrieved from healthy subjects following spectroscopic analysis. To improve the accuracy of sO_2 measurements, a statistical model is formulized. This model describes the noise intensity distribution in Fourier domain (FD) OCT amplitude image, which enables retrieving unbiased true OCT intensity from low signal-to-noise ratio (SNR) images.

Finally, a vis-OCT microscope is developed to monitor dynamic changes within the cerebral circulation following ischemic stroke. This study demonstrates the application of vis-OCT beyond ophthalmic imaging, and serves as a proof of concept that vis-OCT has the potential to be employed in a wide-array of biomedical research.

Acknowledgement

I would like to first thank my advisor Dr. Hao Zhang. He is a great mentor as well as a friend. He has great vision of research and constantly inspired me to explore beyond the current frontier. As a mentor, he always welcomes new ideas, providing any support to realize them. As a friend, he shared his experience as a successful independent researcher and guided me to find my own career path. He pushes me move forward when I felt satisfied with my results; he cheers me up and helps me when the experiments failed. Without him, this dissertation could never be finished.

I would like to thank my committee members for their constant support over years. Dr. Robert Linsenmeier is a very knowledgeable scientists. I learned a lot from our discussions and his course, *Advanced Physiology*. He also taught me that a great scientist should be brave enough to admit the limitation of his/her knowledge, which is a philosophy I would remember forever. Dr. Cheng Sun gave me lots of advice on my experiments and we had countless fruitful discussion I took Dr. Vadim Backman's course, *Advanced Optics*, during my first year. Though it was a challenging class, I learned a lot about electrodynamics and light scattering theory from his teaching. His solid understanding in physics encouraged me to work harder in the mathematical and physical aspects in my dissertation work.

I would like to thank Dr. Ji Yi, a postdoctoral fellow during my first three years of PhD study. He taught me the fundamentals of optical coherence tomography. His skills and passion over scientific research greatly influenced me and inspired me to follow his successful path as a

researcher. I would also like to thank my lab mates for their constant inspiration and fruitful discussions. I enjoyed every moment working with them. They shared my joy when I published my first paper and relieved my frustrations when my project went sideways. You enriched my life as a PhD student, filling the black-and-white academic life with shades of color.

Lastly, I thank my family, my mother and father, and my grandparents, for their endless love and support, and their every selfless sacrifice for their son.

Table of Contents

Abstract.....	3
Investigating functional extension of optical coherence tomography for spectroscopic analysis of blood oxygen saturation.....	3
Acknowledgement	6
Table of Contents.....	8
List of Tables	13
List of Figures.....	14
CHAPTER 1	20
Introduction.....	20
1.1 Development and principles of OCT	21
1.2 Functional aspects of OCT imaging.....	29
1.2.1 Polarization sensitive OCT (PS-OCT).....	30
1.2.2 Doppler OCT and OCT flowmetry	32
1.2.3 Spectroscopic OCT and OCT oximetry	34
1.3 Challenges of OCT	37
1.3.1 Multiple scattering	37
1.3.2 Imaging resolution	37
1.3.3 Imaging contrast.....	38
1.3.4 Noise and speckle in OCT imaging	39

1.3.5 Selection of wavelength bands in OCT imaging	9
1.4 Scope of the dissertation	40
1.4.1 Organization of the dissertation	40
CHAPTER 2	42
Illumination wavelength and its effects on anatomical and functional OCT imaging	42
2.1 Introduction.....	43
2.2 Investigating the optimal wavelength band and accuracy of OCT oximetry: a Monte Carlo study .	45
2.2.1 Monte Carlo simulation model and algorithms.....	46
2.2.2 Simulation results.....	55
2.2.3 Discussion.....	61
2.3 Comparing anatomical and functional imaging capability between visible-light and NIR OCT using a dual-band system.....	63
2.3.1 Material and Methods	63
2.3.2 Results.....	67
2.2.3 Discussion.....	74
2.4 Summary	76
CHAPTER 3	77
Label-free retinal angiography and angiograph-based oximetry	77
3.1 Introduction.....	77
3.2 Theoretical formulation of OCT angiography-based oximetry	80
3.3 Material and Methods	83

3.3.1 Scanning protocol for vis-OCT angiography	10
3.3.1 Scanning protocol for vis-OCT angiography	83
3.3.2 Phantom experiment preparation	84
3.3.3 Animal preparation	84
3.3.4 Vis-OCT imaging of retinal microvasculature.....	85
3.4 Results.....	90
3.4.1 Phantom experiment verification	90
3.4.2 Vis-OCT angiographic imaging using dynamic contrast.....	92
3.4.3 Measuring absolute retinal circulation sO ₂ using spectroscopic OCTA	95
3.4.4 Measuring relative sO ₂ change in choriocapillaris using OCTA	96
3.5 Discussion	97
CHAPTER 4	100
A combined SLO/OCT ophthalmological imaging system for human subjects	100
4.1 Introduction.....	101
4.2 Developing the hardware platform for vis-OCT imaging.....	105
4.2.1 A combined visible-light SLO/OCT ophthalmoscope prototype for imaging human subjects	105
4.2.2 Imaging acquisition protocols	107
4.2.3 Laser safety considerations	108
4.2.4 Human subject recruitment	109
4.2.5 Data processing	110
4.2.6 Results.....	111
4.3 Retrieving retinal circulation sO ₂ using spectroscopic analysis on vis-OCT images	119

	11
4.3.1 Spectroscopic analysis	119
4.3.2 Statistical modeling of noises in OCT amplitude images	120
4.3.3 Vis-OCT oximetry on healthy subjects.....	129
4.4 Discussion.....	135
CHAPTER 5	138
Vis-OCT applications beyond ophthalmological imaging.....	138
5.1 Introduction.....	138
5.2 Material and Methods	141
5.2.1 System design	141
5.2.2 Animal preparation and surgery.....	142
5.2.3 Vis-OCT angiographic protocol and angiogram.....	145
5.2.4 Vis-OCT angiography-based oximetry	146
5.2.5 Quantitative fluorescence microscopy	148
5.3 Results.....	149
5.3.1 Vis-OCT angiography.....	149
5.3.2 Vis-OCT angiography-based oximetry in brain cortex.....	151
5.3.3 Quantitative measurement of blood Rose Bengal concentration	154
5.4. Discussion.....	155
CHAPTER 6	158
Conclusion and future work.....	158
6.1 Conclusion	158

	12
6.2 Future work.....	161
6.2.1 Investigating the impact of visible light illumination on retinal hemodynamic response.....	161
6.2.2 Angiographic-based OCT oximetry in human subjects	162
6.2.3 Improving the functionality and hardware implementation of the vis-OCT prototype	163
6.2.4 Extend the OCT intensity model to include speckles	164
References.....	165
Appendix A.....	177
Maximum permissible exposures for ocular safety of OCT systems using broad-band visible light illumination, calculated based on ANSI Z136.1-2000 standard	177
Vita.....	181

List of Tables

Table 2.1	Optical properties (μ_a [cm^{-1}], μ_s [cm^{-1}], and g [-]) of solid ocular tissue used in the Monte Carlo Simulation.....	47
Table 2.2	Optical properties of whole blood within the simulated wavelength bands. All coefficients are of unit [cm^{-1}].....	50
Table 3.1	Summary of data processing procedures to extract sO ₂	89
Table 4.1	Reduction on sO ₂ measurement error ($\Delta\sigma$) using statistical fitting (SF) against arithmetic mean (AM). sO ₂ values are mean \pm S.D of 10 measurements.....	135

List of Figures

- Figure 1.1** The Michaleson interferometer. (a) The actual experimental setup for the 1887 Michelson-Morley experiment. (b) Equivalent optial path for the Michaleson interferometer. E_I : incidence electric field. E_r : reflected electric field from the reference arm. E_s : reflected electric field from the sampling arm. E_d : combined field in the detection arm.22
- Figure 2.1** Simplified eye model used in the numerical Monte Carlo study. (a) Schematic diagram of a human eyeball duing OCT imagng. (b) Dimensions and relative positions of the four simulated layer structures from the posterior segment (not to scale). A cylindrcal blood vessel is imbeded in the retina layer parallel to surface.47
- Figure 2.2** Flowchart of the implemented Monte Carlo simulation algorithm for generating spectroscopic MC-OCT signal.52
- Figure 2.3** (a) A sample simulated MC-OCT B-scan imaging. The labeled structures corresponds well to the constructed four-layer eye model. (b) Mean and standard deviation of back-scattered intensity (I_b) from 10 simulation runs at each photon density level.....55
- Figure 2.4** Normalized back-scattered intenisty (I_b) from (a) visible wavelength range; and (b) NIR wavelength range. The solid line is obtained by least sqaures fitting all spectral points against known whole blood compound attenuation coefficients. The algorithm does not converge for NIR data, and one representative case is plotted in (b).57
- Figure 2.5** Normalized compound attenuation coefficient μ_t for (a) visible wavelenth range; and (b) NIR wavelength ange. The red dahsed curve represents fully oxygenated blood μ_{t_OxyB} ; the blue dot-dash curve represents fully deoxygenated blood μ_{t_DeOxyB} ; the green solid line represents whole blood compound attenuation cooeffiecient when $sO_2 = 70\%$58
- Figure 2.6** Investigating the accuracy of vis-OCT oximetry. (a) The accuracy of vis-OCT oximetry with respect to preset blood sO_2 . Vessel diameter is fixed at $100 \mu m$. Two ROI location is investigated, one is placed in the middle of the vessel (blue box, MD), and the other is near the bottom of the vessel (red box, BT). The solid black line is the expected value. (b) The accuracy of vis-OCT oximetry with respect to varying vessel diameter in the physiological range. Blood sO_2 is fixed at 70% (blue dashed line). The sampling ROI is placed near the bottom of the vessel.59
- Figure 2.7** Inversely calculating sO_2 using all possible packing factor W values ranging form 0 to 1. The blood sO_2 is fixed at 70% for both the numerical simulation and vis-OCT animal experiment (blue dashed line). The black solid curve represents results

obtained using MC-OCT (Sim). The red box represents experiment results obtained by vis-OCT imaging of rat retinal circulation *in vivo* (Exp).61

- Figure 2.8** Schematic diagram for the visible-light and NIR dual-band OCT system. BS: beam splitter; CL: collimating lens; DM 1-3: dichroic mirror; FC: 2×2 fiber coupler; GM: galvanometer scan mirrors; KT: Keplerian telescope; LS: supercontinuum laser source; P: polarizer; PC: polarization controller; Ref 1-2: reference arm; S: beam stopper; SM: spectrometer.64
- Figure 2.9** OCT detection sensitivity and axial imaging resolution. (a) OCT axial impulse response from mirror surface acquired using vis-OCT subsystem. (b) OCT axial impulse response from mirror surface acquired using NIR-OCT subsystem. The first peak is used as benchmarks for both sensitivity and resolution measurements.68
- Figure 2.10** Comparison of structural visible and NIR OCT images. (a) & (b) *En face* view of OCT structure image for vis- and NIR-OCT, respectively. (c) & (d) are B-scan image taken from the location indicated by the yellow dashed line in (a) and (b), respectively. C: Choroid; NFL: neural fiber layer; OPL: outer plexiform layer; RPE: retinal pigment epithelium. (e) & (f) show the A-line profiles taken from yellow dashed line in (e) and (f), respectively. Scale bar: 100 μm70
- Figure 2.11** Wavelength-dependent OCT back-scattered intensity from a identified artery (A) and vein (V). (a) Spectra obtained using vis-OCT subsystem. (b) Spectra obtained using NIR-OCT subsystem.72
- Figure 2.12** OCT oximetry on major retinal circulation vessels. $s\text{O}_2$ values are obtained using vis-OCT data sets.72
- Figure 2.13** Doppler OCT phase image from the dual-ring scan protocol. (a) Vis-OCT data set. (b) NIR-OCT data set. Scale bar: 100 μm73
- Figure 2.14** Comparison of absolute blood flow measurements using both vis- and NIR-OCT. The vessels are indexed from left to right in Fig. 2.12. Errorbar is S.D.74
- Figure 3.1** Cross-sectional B-scan of the tube using OCT structural (top row) and OCT angiographic (bottom row) contrast. The images are acquired at varying flow speed from 0.00 mL/min to 0.05 mL/min. Scale bar: 50 μm90
- Figure 3.2** (a) *En face* OCT angiography image of the polystyren capillary tube. The yellow rectangles indicate the places where OCTA spectra are retrieved. Scale bar: 50 μm ; (b) OCTA spectrum (I_{OCTA}) retrieved from phantom tube with flow rate = 0.00 mL/min. (c) Averaged intensity I_m from capillary tube at increasing flow rate; (d) The spectral derivative of I_{OCTA} spectrum within 560-580 nm from the capillary tube at increasing flow rates. Error bar = S.D.91

- Figure 3.3** Cross-sectional B-scan from (a) OCT structural image, and (b) OCTA contrast, in rat retina *in vivo* using vis-OCT. Anatomical layers labeled include: NFL/GCL-nerve fiber layer/ganglion cell layer, IPL-inner plexiform layer, INL-inner nuclear layer, OPL-outer plexiform layer, ONL-outer nuclear layer, ELM-external limiting membrane, IS/OS-inner segments/outer segments, and RPE-retinal pigment epithelium. Vessels in retinal circulation and choriocapillaries are identified. Artifacts created by the hyper-reflective layers in IS/OS and RPE are indicated with a blue arrow. (c) Overlaid image from (a) and (b). The choriocapillaris lays beneath RPE layer.93
- Figure 3.4** Vis-OCT *en face* fundus projection of a rat retina using *in vivo*. (a) Vis-OCT structural fundus image (b) Vis-OCT angiographic fundus image. (c) Three-dimensional (3D) of rat retinal microvasculature.94
- Figure 3.5** Measured arterial sO_2 calibrated against pulse oximetry readings ($R^2=0.87$) from $n=8$ rats. Black line is the linear regression of the data95
- Figure 3.6** Measured mean sO_2 of branch retinal arteries and veins upon changes of inhalation gas mixtures ($n=8$ for each bar). Error bar = S.E.M. *: $p < 0.05$. **: $p < 0.01$96
- Figure 3.7** Measured relative choriocapillaris sO_2 change comparing to normal air breathing ($n = 6$). ***: $p < 0.001$ 97
- Figure 4.1** (a) Schematic of the combined visible light SLO and OCT prototype system for human subjects. SC: Supercontinuum laser source; SF: Single-mode fiber; SM: Spectrometer; Ref: Reference arm; FM: Motorized flip mirror; MS: Motorized beam stop; GM: Galvometer mirror; MF: Multimode fiber; APD: Avalanche photodiode; MR: Mirror; ND: Neutral density filter. (b) photograph of system. A blue arrow points to the three-dimensional translational chin rest for adjusting eye position; a yellow arrow points to the stationary optics board.....106
- Figure 4.2** OCT axial impulse response from the reflection of a mirror surface. The insert shows a magnified view of the height and full-width-at-half-maximum (FWHM) of the second peak.....112
- Figure 4.3** SLO image centered at the fovea. (a) $20^\circ \times 20^\circ$ FOV. (b) $10^\circ \times 10^\circ$ FOV.....113
- Figure 4.4** Vis-OCT image centered on fovea. (a) $20^\circ \times 20^\circ$ FOV. (b) $10^\circ \times 10^\circ$ FOV, magnification of the red box. (c) Vis-OCT B-scan cross-section image showing layered retinal structures around fovea, acquired from the location highlighted in (a). 12 distinctively identified layers are labeled: ILM: Inner-limiting membrane; NFL: Nerve fiber layer; GCL: Ganglion cell layer; IPL: Inner plexiform layer; INL: Inner nuclear layer; OPL: Outer plexiform layer; ONL: Outer nuclear layer; IS/OS: Inner/outer segment junction; OS: Outer segment of photoreceptor; RPE: Retinal pigmented epithelium; BM: Bruch's membrane.....114

- Figure 4.5** SLO image centered at the ONH. (a) $20^\circ \times 20^\circ$ FOV. (b) $10^\circ \times 10^\circ$ FOV, magnification of the red box.....115
- Figure 4.6** Vis-OCT image centered on ONH. (a) $20^\circ \times 20^\circ$ FOV. (b) $10^\circ \times 10^\circ$ FOV, magnification of the red box. (c) Vis-OCT B-scan crosssection image showing layered retinal strucutes around ONH, acquied from the location highlighted in (a).116
- Figure 4.7** (a) Cross-sectional vis-OCT image around ONH. The inset at the botton-right corner shows the *en face* projection where the B-scan is taken from. (b-c) Magnified in images from the squared areas in (a).....117
- Figure 4.8** Comparison between B-scan image from (a) vis-OCT prototype, and (b) a commerical NIR OCT system (Cirrus-HD-OCT, Carl Zeiss Meditec).....118
- Figure 4.9** Statistical characteristics of noise in OCT. (a) Simulated interferogram with added Gaussian noise from a single reflective surface (red solid line). The black solid line is the noise free interferogram. The shaded area depicts S.D. of the added noise, which corresponds to $\text{SNR} = 30$ dB for the reconstructed image; (b) The distribution of the corresponding non-DC peak values on the 2D complex plane after discrete Fourier transform reconstruction. The insert shows the spatial distribution of the complex values in the 2D plane, which were tested to follow bi-variate normal distribution. (c) The distribution of the modulus r . The solid line is generated using the data from (a) and (b). The dashed line showed a non-symmetrical case where SNR was much worse (10 dB).....126
- Figure 4.10** Flowchart showing the steps of retrieving true OCT intensity using statistical fitting approach. VOI: volume-of-interest. For OCT oximetry, the same VOI is used for all narrow-band images.127
- Figure 4.11** (a) A typical human vis-OCT B-scan image showing three sampling regions: one from within a blood vessel and two from the background at different depths. (b) The intensity probability density function (pdf) of OCT features (gray line) and its statistical fitting (red line). The gray and red arrows indicate the arithmetic mean and fitted OCT intensity, respectively. (c) and (d) The pdfs of pure OCT noise intensities from the background at their respective depths in gray lines. Red lines are the corresponding statistical fittings. The gray arrows indicate arithmetic means. The fitted OCT intensities are both approximately zero.129
- Figure 4.12** Vis-OCT image from a 27-year-old female. (a) Vis-OCT fundus image. (b) OCT intensity spectrum taken from the identified branch retinal artery (A_1 , black curve) and its least-squares fitting (red line). (c) OCT intensity spectrum taken from the identified branch retinal vein (V_1 , black curve) and its least-squares fitting (red line).130
- Figure 4.13** Vis-OCT image from a 27-year-old male. (a) Vis-OCT fundus image. (b) OCT intensity spectrum taken from the identified branch retinal artery (A_1 , black curve) and

its least-squares fitting (red line). (c) OCT intensity spectrum taken from the identified branch retinal vein (V_1 , black curve) and its least-squares fitting (red line).132

Figure 4.14 Vis-OCT image from a 38-year-old female. (a) Vis-OCT fundus image. (b) OCT intensity spectrum taken from the identified branch retinal artery (A_1 , black curve) and its least-squares fitting (red line). (c) OCT intensity spectrum taken from the identified branch retinal vein (V_1 , black curve) and its least-squares fitting (red line).133

Figure 4.15 Vis-OCT image from a 60-year-old female. (a) Vis-OCT fundus image. (b) OCT intensity spectrum taken from the identified branch retinal artery (A_1 , black curve) and its least-squares fitting (red line). (c) OCT intensity spectrum taken from the identified branch retinal vein (V_1 , black curve) and its least-squares fitting (red line).134

Figure 5.1 Schematic diagram of the visible-light optical coherence tomography angiographic system for imaging mouse cortex. BS: beam splitter; DC: dispersion compensator; GS: galvanometer scanning mirror; M: reference mirror; OBJ: scanning lens; SCS: supercontinuum source; SM: spectrometer; VA: variable neutral density attenuator.142

Figure 5.2 A mouse is secured in the animal holder ready for vis-OCT imaging. The headbar is attached to the holder to reduce motion artifacts. The headbar has a center hole of $5 \times 6 \text{ mm}^2$144

Figure 5.3 Extinction coefficient of Rose Bengal, oxygenated hemoglobin (HbO_2), and deoxygenated hemoglobin (HbR). These three chromophores have strong overlapping absorption within the wavelength range from 500 nm – 580 nm.149

Figure 5.4 Depth-coded OCT angiograph in a mouse cortex before and after photothrombosis induced focal ischemic stroke. (a) Pre-photothrombosis (Pre-PT) microvascular structure. A: middle cerebral artery. V: superficial pial veins (b) Post-photothrombosis (Post-PT) microvascular structure. Scale bar: 500 μm150

Figure 5.5 Vessel profiles measured from respective locations indicated in Fig. 5.4. (a) OCTA profile for vessel i. (b) OCTA profile for vessel ii. (c) OCTA profile for vessel iii. Blue line: pre-photothrombosis; red line: post-photothrombosis.151

Figure 5.6 Normalized wavelength-dependent OCT angiographic contrast using different methods. (a) Normalized spectra I_{norm} using source spectrum. (b) dual-depth normalization $\frac{AI(z_2, \lambda)}{AI(z_1, \lambda)}$ spectra. Dashed lines are simulated theoretical values for fully oxygenated whole blood (Oxy-WB) and fully deoxygenated whole blood (Deoxy-WB), which are calculated using Beer-Lambert law and compiled literature data for the optical properties of whole blood.152

Figure 5.7 Retrieving sO_2 from conventionally normalized spectra and dual-depth method. (a) Normalized frequency (f_{norm}) of calculated sO_2 using the conventional method. (b) f_{norm} of calculated sO_2 using the new dual-depth method.153

Figure 5.8 Vascular sO_2 map before and after photothrombosis induced focal ischemic stroke. (a) Before photothrombosis (Pre-PT). (b) After photothrombosis (Post-PT). Scale bar: 500 μm . Arrows indicate the vessels where mean sO_2 is calculated. Elliptical area indicates where arteries and veins overlap each other and only averaged sO_2 is displayed.....154

Figure 5.9 Measuring blood Rose Bengal (RB) concentration using quantitative fluorescence microscopy. (a) Calibration curve for quantitative fluorescence microscopy measurement of RB concentration. Black dots: Mean RB fluorescent intensity (FL) is plotted against known concentration of RB solution. Error bar is standard deviation (S.D) Red dashed line: linear regression of the calibration points, $R^2=0.97$. Blue cross: RB fluorescent intensity as measured in diluted blood drawn from the mouse after injection. The points are registered to the calibration curve to yield RB concentration of the solution. (b) Blood RB concentration as estimated using quantitative FL measurements at time points 8, 16, 24, and 32 minutes after intravenous RB injection.155

CHAPTER 1

Introduction

Tomographic imaging is an indispensable tool in biomedical research and the clinic. Generating slice images of three-dimensional (3D) objects, tomographic techniques can provide non-invasive or minimally-invasive diagnostic information. Some notable modalities, including X-ray computed tomography (CT) and magnetic resonance imaging (MRI), visualize intrinsic density contrast and have enjoyed wide clinical acceptance. Meanwhile, optical-based methods reveal a very different set of tissue properties, namely absorption, scattering, birefringence, etc. [1]. In particular, optical coherence tomography (OCT), an optical analogy to ultrasound imaging, relies on backscattered photons to provide depth-resolved cross-sectional images with micrometer spatial resolution. Since its inception in 1991, OCT has had a transformative impact in the field of ophthalmology and vision research, becoming the *de facto* standard for diagnosing retinal diseases [1-3].

While physicians still rely heavily on structural images highlighting morphological changes to reach diagnostic conclusions, it is well known that alterations in cell activity precedes noticeable structural changes throughout pathological progression of diseases. Thus, an imaging modality that can monitor the functionality of tissues has the potential to revolutionize the current practice

of reactive medicine into preventive medical care, greatly improving outcomes while reducing costs. In such contexts, this dissertation approaches the quest of developing functional OCT, particularly OCT oximetry. Novel physiological parameters, i.e. hemoglobin oxygen saturation (sO_2) and oxygen metabolism rate (MRO_2), are incorporated to monitor metabolic activities of regional tissue. The scope of the works includes verification of OCT oximetry, monitoring oxygenation in the retinal circulation, and applications beyond ophthalmology.

Scientific innovations are built upon foundations laid by generations of passionate and revolutionary pioneers. In this chapter, we will first take a brief review on the OCT principles and its development over the past decades so respects are paid to those who have done the hard work. Then, limitations and challenges of current OCT applications are outlined and discussed. Finally, a summary previews the topics covered in this dissertation and how they address the encountered problems.

1.1 Development and principles of OCT

The core of every OCT system is an optical interferometer. Interferometry makes use of the wavelike behaviors of light. Light is considered an electromagnetic wave in classical electrodynamics. When one wave superposes with another, in-phase superposition leads to constructive interference and out-of-phase superposition leads to destructive interference. Thus, one can compute the relative phase shift, or relative optical path length difference Δl , between two mutually coherent beams by detecting the maxima and minima in the interference fringes. Using this approach, even tiny amounts of displacement, on the order of nanometers, can be measured accurately. Perhaps the most famous application of the interferometry measurements is the 1887

Michelson-Morley experiment. In an attempt to detect earth's motion through the supposed aluminiferous aether, which most physicists at the time believed was the medium in which light wave propagated [4], Michelson and Morley invented an apparatus using a single beam splitter to split light into and combine it from two orthogonal arms. Though the null results of the experiment essentially disproved the existence of aether, the apparatus, later named as the Michelson interferometer, remained as a tool to measure distances which are too small to be measured using other methods.

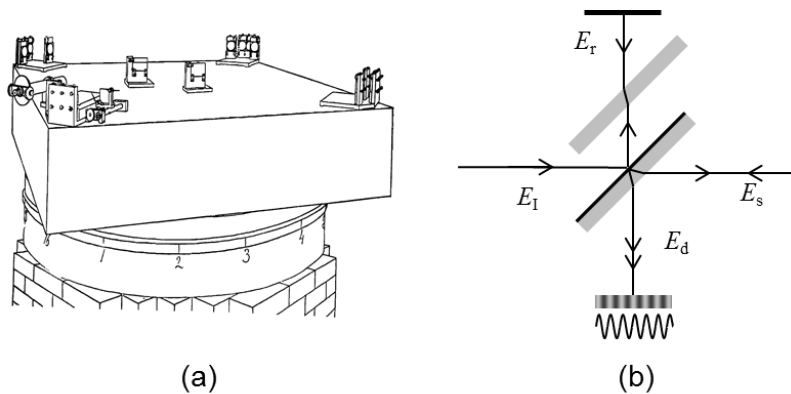


Figure 1.1 The Michaleson interferometer. (a) The actual experimental setup for the 1887 Michelson-Morley experiment. (b) Equivalent optical path for the Michaleson interferometer. E_i : incidence electric field. E_r : reflected electric field from the reference arm. E_s : reflected electric field from the sampling arm. E_d : combined field in the detection arm

In the standard interferometer, light of long coherence length l_c is used. Unfortunately, the practice introduces the infamous 2π ambiguity as the interference fringe is cyclic in nature. As the maxima and minima repeat themselves every integer multiplication of wavelength, the order of the interference cannot easily be determined. Thus, standard interferometric methods are not suitable for measuring distance larger than the wavelength within an object where a definitive reference cannot be directly established.

To resolve this 2π ambiguity, light of limited coherence length can be used in a standard interferometer, leading to low coherence interferometry (LCI) [5]. The adoption of low coherence light source introduces the “coherence gating” effect. As the name suggests, in LCI, interference fringes can only be observed when the optical path length difference between the reference and sample arm is within one coherence length. Thus, the exact location of the sample surface can be uniquely determined with respect to the reference. The measurement resolution of LCI is determined by the coherence length of the light source.

One can mathematically model the LCI using the complex exponential notation for plane wave electric field. Assuming the Michaelson configuration illustrated in Fig. 1.1(b), one can express the light intensity in the detection arm I_d ,

$$I_d = \langle |E_d|^2 \rangle = (I_r + I_s) + 2\text{Re}\{\langle E_r^*(t + \tau)E_s(t) \rangle\}, \quad (1.1)$$

where $\langle \cdot \rangle$ operator represents ensemble average; E_r and E_s are the complex electric field reflected from the reference and sample arm, respectively; I_r and I_s are the corresponding light intensity, $I_r = \langle |E_r|^2 \rangle$ and $I_s = \langle |E_s|^2 \rangle$; τ is the relative time delay between the two arms. Since the speed of light, C , is a constant, the optical path length difference Δl and the relative time delay τ are interchangeable, and either one can uniquely determine the other. By definition, the function $\Gamma(\tau) = \langle E_r^*(t + \tau)E_s(t) \rangle$ represents the temporal cross-correlation function between the reflected reference and sample fields. Decomposing the rightmost term in Eq. 1.1 using Euler’s formula leads to expression,

$$\text{Re}\{\langle E_r^*(t + \tau)E_s(t) \rangle\} = |\Gamma(\tau)| \cos[2\pi\nu_0\tau + \Phi(\tau)], \quad (1.2)$$

where $Re\{\cdot\}$ operator means the real part of the expression; ν_0 is the center optical frequency, $\Phi(\tau)$ is the phase of the correlation function $\Gamma(\tau)$. The cosine term in Eq. 1.2 corresponds to the interference fringe, while the $|\Gamma(\tau)|$ term is the fringe visibility, representing the effect of coherence gating.

Inasmuch that both E_r and E_s are the modulated versions of the illumination electric field E_I , $\Gamma(\tau)$ is indeed an auto correlation function of the source field. One can further apply Wiener-Khinchin (W-K) theorem to establish the relationship between $\Gamma(\tau)$ and the source power spectral density $S(\nu)$. According to W-K theorem, the autocorrelation function of a wide-sense-stationary random process has a spectral decomposition given by the power spectrum of that process. The relationship can be expressed in the form of Fourier transform,

$$\Gamma(\tau) = \int_0^{\infty} S(\nu) \exp(j2\pi\nu\tau) d\nu, \quad (1.3)$$

where ν is the frequency of the light; the source power spectral density can be calculated as $S(\nu) = \left| \int_{-\infty}^{\infty} E_I(t) \exp(-j2\pi\nu t) dt \right|^2$. The semi-infinite integral indicates the non-negativity of light frequency. For a practical band-limited system, it is not difficult to notice that the duality property of Fourier transform requires that the width of function $\Gamma(\tau)$ is inversely proportional to the width of $S(\nu)$. In other words, the broader the source power spectrum is, the narrower the $\Gamma(\tau)$ will be. Analytically, if the source spectral density assumes the form of Gaussian function,

$$S(\nu) = \frac{2\sqrt{\ln 2/\pi}}{\Delta\nu} \exp \left[-4 \ln 2 \left(\frac{\nu - \nu_0}{\Delta\nu} \right)^2 \right], \quad (1.4)$$

the result of the Fourier transform will also take the form of Gaussian function,

$$\Gamma(\tau) = \exp \left[- \left(\frac{\pi \Delta\nu \tau}{2\sqrt{\ln 2}} \right)^2 \right] \exp(-j2\pi\nu_0\tau). \quad (1.5)$$

In both Eq. 1.4 and Eq. 1.5, ν_0 is the center frequency and $\Delta\nu$ is the bandwidth. The scalar term ensures that the integral of $S(\nu)$, or the total energy, is unity.

Without loss of generality, one can define the width of both $S(\nu)$ and $|I(\tau)|$ function using the full-width-at-half-maximum (FWHM) criteria. The FWHM of $|I(\tau)|$ with respect to $\Delta\nu$ is thus,

$$\Delta\tau = \frac{4 \ln 2}{\pi \Delta\nu}. \quad (1.6)$$

Plugging in the speed of light C and using the relationship $\lambda = C/\nu$ or $\Delta\nu = C\Delta\lambda/\bar{\lambda}^2$, the conventional expression for the coherence length can be reached,

$$l_c = \frac{4 \ln 2}{\pi} \frac{\bar{\lambda}^2}{\Delta\lambda}, \quad (1.7)$$

where $\bar{\lambda}$ is the center wavelength and $\Delta\lambda$ is the spectral width. In the Michelson configuration, the scalar term is divided by two for the roundtrip, leading to $l_c = \frac{2 \ln 2}{\pi} \frac{\bar{\lambda}^2}{\Delta\lambda} \approx 0.44 \frac{\bar{\lambda}^2}{\Delta\lambda}$. This expression is traditionally used as the theoretical axial resolution of the LCI. In real-life applications, non-Gaussian spectrum and other than FWHM can be used. However, this only affects the coefficient of the expression, while the fundamental principle that the coherence length is proportional to the square of center wavelength and inversely proportional to the spectral bandwidth remains unchanged.

In the original LCI designs, the length of the reference arm was altered in a controlled manner to directly acquire the auto correlation function covering the entire sample depth. To differentiate this technique from later developments, this approach is retrospectively named time-domain OCT (TD-OCT). To synthesize cross-sectional images, a series of depth scans are performed on laterally-adjacent locations, either by translating the illuminating probing beam or moving the

sample. In a first approach towards tomographic imaging, a cross-sectional topographic image of the retinal pigment epithelium (RPE) of a human eye obtained *in vivo* by the dual beam LCI technique was presented at the ICO-15 SAT conference by Fercher *et al* in 1990 [5] and published by Hitzenberger *et al* in 1991 [6]. Later in 1991, Huang *et al* from Fujimoto's group at MIT published cross-section image of human retina using a fiber-optics based interferometer [2]. They coined the term optical coherence tomography (OCT) to describe the technology. Since then, OCT has become a prominent biomedical tissue-imaging technique, particularly suited to ophthalmic applications and other tissue imaging that require micron-level resolution and millimeter penetration depth.

In 1995, Fercher *et al* developed a new method to obtain the auto-correlation function in LCI [7]. Named Fourier domain OCT (FD-OCT) or spectral domain OCT (SD-OCT), this approach revolutionized entire OCT field as it eliminated the need for mechanical scanning of the reference arm, thus allowing the image speed to increase to the kilohertz region. Later in 1997, the rapidly tunable laser was developed and adopted in OCT [8]. By rapidly sweeping the source spectrum of the illumination source, this setup takes advantage of the higher sensitivity and readout speed of single photon detectors, further increasing imaging speed to the megahertz level [9-11].

Though physically, the FD-OCT imaging principle is exactly the same as the above derivation for TD-OCT, it is non-trivial to rewrite the equations to explicitly include the frequency components. Thus, one can better appreciate how the inverse Fourier transform reconstructs the auto correlation function and why the axial scan can be omitted. With the light frequency explicitly defined, the complex exponential plane wave notation for the incident electric field is,

$$E_1(t, \nu) = \sqrt{S(\nu)}e^{-j2\pi\nu t}. \quad (1.8)$$

The reflected electric field from the reference and sample arm can be expressed with respect to the incident field, $E_r(t, \nu) = rE_1(t - \tau_r, \nu)$ and $E_s(t, \nu) = sE_1(t - \tau_s, \nu)$, respectively. r and s are electric field reflectance of the reference and sample, respectively. τ_r and τ_s are the total delay in the reference and sample arms, respectively. Thus, one can write the frequency-dependent detected intensity $I_d(\nu)$ as,

$$\begin{aligned} I_d(\nu) &= \langle |E_d(\nu)|^2 \rangle \\ &= \langle (E_r + E_s)^*(E_r + E_s) \rangle \\ &= \langle E_r^* E_r \rangle + \langle E_s^* E_s \rangle + \langle E_r^* E_s \rangle + \langle E_s^* E_r \rangle. \end{aligned} \quad (1.9)$$

The first term in Eq. 1.9 represents the intensity of the light reflected from the reference arm,

$$\langle E_r^* E_r \rangle = r^* r S(\nu) = R_r S(\nu), \quad (1.10)$$

while the second term represents the intensity of the light reflected from the sample arm

$$\langle E_s^* E_s \rangle = s^* s S(\nu) = R_s S(\nu). \quad (1.11)$$

In Eq. 1.10 and Eq. 1.11, R_r and R_s are the reflectance of the reference and sample by definition. The cross correlation terms require slightly more work. Using the expression defined in Eq. 1.8, the third term can be written as,

$$\begin{aligned} \langle E_r^* E_s \rangle &= \langle (r\sqrt{S(\nu)}e^{-j2\pi\nu(t-\tau_r)})^* (s\sqrt{S(\nu)}e^{-j2\pi\nu(t-\tau_s)}) \rangle \\ &= \langle r^* s [S(\nu)e^{j2\pi\nu(t-\tau_r)} e^{-j2\pi\nu(t-\tau_s)}] \rangle \\ &= r^* s [S(\nu)e^{-j2\pi\nu(\tau_r-\tau_s)}]. \end{aligned} \quad (1.12)$$

Similarly, the fourth and final term becomes,

$$\langle E_s^* E_r \rangle = s^* r [S(\nu) e^{j2\pi\nu(\tau_r - \tau_s)}]. \quad (1.13)$$

For simplicity, one can define $\tau = \tau_r - \tau_s$ and plug Eq. 1.10 to Eq. 1.13 into Eq. 1.9,

$$\begin{aligned} I_d(\nu) &= R_r S(\nu) + R_s S(\nu) + r^* s [S(\nu) e^{-j2\pi\nu\tau}] + s^* r [S(\nu) e^{j2\pi\nu\tau}] \\ &= S(\nu) [R_r + R_s + r^* s e^{-j2\pi\nu\tau} + s^* r e^{j2\pi\nu\tau}]. \end{aligned} \quad (1.14)$$

Comparing Eq. 1.14 with Eq. 1.1, one can find that both τ in these two equations have exactly the same physical meaning, the relative time delay between the reference and sample arm.

Now the detector intensity is explicitly expressed as a function of frequency, it is straightforward to apply inverse Fourier transform to retrieve the auto correlation function,

$$I_d(t) = \int I_d(\nu) e^{-j2\pi\nu t} d\nu, \quad (1.15)$$

Depending on whether the reference and sample reflectance have frequency dependency, Eq. 1.15 can be expanded into two forms: The simpler form,

$$I_d(t) = \Gamma(t) \otimes [R_r \delta(t) + R_s \delta(t) + r^* s \delta(t - \tau) + s^* r \delta(t + \tau)], \quad (1.16)$$

assumes that both R_r and R_s are frequency-independent. The two peaks at $-\tau$ and $+\tau$ correspond to the relative location of the sample. The two Dirac delta functions are subsequently convolved with the auto correlation function of the source, $\Gamma(t)$. Thus, the width of the peak depends on the width of $\Gamma(t)$. Another interpretation of this relationship is that $S(\nu)$ acts like a window function during the Fourier transform. As multiplication in the frequency domain translates to convolution in the temporal domain, the peaks can be regarded as the shifted version of the Fourier transform of the window function. In conclusion, Eq. 1.16 again demonstrates that the coherence length determines the resolution in LCI.

Meanwhile, if either of the two is a function of the frequency, the expression assumes the following general form,

$$I_d(t) = \Gamma(t) \otimes [\text{IFT}\{R_r\} + \text{IFT}\{R_r\} + \text{IFT}\{r^*s\} \otimes \delta(t - \tau) + \text{IFT}\{s^*r\} \otimes \delta(t + \tau)]. \quad (1.17)$$

In addition to the spectral bandwidth-resolution relationship, Eq. 1.17 further indicates that the reflectance spectrum is also encoded in the recovered correlation function. Thus, Eq. 1.17 can also serve as the foundation for spectroscopic OCT.

1.2 Functional aspects of OCT imaging

Following the theoretical analysis presented in section 1.1, one can appreciate that OCT has some extraordinary properties. First of all, axial and lateral imaging resolution are decoupled from each other. OCT lateral resolution follows diffraction limit as in most optical imaging systems. Like laser scanning microscopy, the minimum achievable illumination spot size dictates the smallest resolvable features, which in turn is determined by the numerical aperture (NA) of the optic system. In contrast, the axial resolution, which is rigorously derived in the previous section, is almost solely determined by the temporal coherence length of the illumination light. Thus, OCT can achieve high axial resolution images even at tissues where it is impossible or extremely hard to accommodate high NA optics, such as in ophthalmic imaging. Second, the amplitude of the interference signal is the multiplication of the reflected electric field from both reference and sample arm. Thus, the light back scattered from the sample is amplified by the reference light. Such optical amplification provides high dynamic range and sensitivity. Thus, imaging of weakly scattering structures even in a scattering environment is possible, enabling ‘*in situ* optical biopsy’.

Ophthalmic applications have developed the earliest, and continue to be the primary area of research and clinical application for OCT. In the past decade, the growth in many other medical specialties has also become significant, particularly in the fields of cardiovascular imaging (i.e., coronary intravascular OCT), dermatology, and gastroenterology [3]. However, the breakthrough of OCT development lies in functional imaging, where contrast other than direct optical absorption and scattering are used to highlight physiological and pathophysiological changes. In this section, three major functional OCT imaging modalities are reviewed.

1.2.1 Polarization sensitive OCT (PS-OCT)

Light, or electromagnetic wave, is a transverse wave because both the oscillating electric and magnetic fields are perpendicular to the wave propagation direction. Inasmuch, the geometrical orientation of the oscillation, also known as polarization, is a key parameter to characterize the light and the medium interacting with it. The electric field vector direction is usually chosen to describe the polarization states, as the direction of electric field, magnetic field and light propagation direction follows right hand rule and the electric field is the major interacting component of the two. For fully polarized light, the orientation can assume a single direction and remain stationary, leading to linear polarization. Or, it may rotate clockwise and counter clockwise at the optical frequency, which is known as circular or elliptical polarization.

The polarization state of light can be altered by the medium interacting with it. In biological tissues, two major contributing factors can alter light polarization state, optical scattering and optical rotation. While scattering is a random process hard to incorporate, optical rotation has tissue-specificity and can be adopted as the contrast mechanism for selected tissues. There are two

main categories for the underlying mechanisms of optical rotation. The first is the optical activity of chiral materials. As the molecules in these materials lack mirror symmetry, they rotate the incoming electric field towards a certain direction, thus affecting light polarization. Examples include hydroxyapatite crystals in dental enamels. The second category is form birefringence, which depends on the macroscopic structure of the tissue rather than the configuration of individual molecules. Thus, form birefringence is more universal in biological tissues, where it can originate from the linear or circular arrangement of anisotropic proteins. Common tissues that display form birefringence include collagen fiber, muscle and nerve bundle. However, these highly regular arrangements are often disrupted during trauma or pathological progression due to the growth of scar or cancerous tissue. The newly substituted tissues do not share the same ordered structure as the original ones and display altered or a complete lack of birefringence properties. Thus, the loss or change of birefringence can be used as a biomarker for tissue lesion [12, 13].

When light propagates in birefringence materials, light of one specific polarization orientation travels faster than lights of other polarization orientations. This linear polarized light with the highest propagation speed is called the fast ray, and its polarization orientation the fast axis. The relative phase delay between the fast ray and the slower ones are determined by the differences in anisotropic refractive index and the total distance travelled. Thus, two parameters, the fast axis and the relative retardation, can be used to characterize tissue polarization properties. The first polarization-sensitive OCT (PS-OCT) application reported by Hee *et al* is capable of characterizing the phase retardation between orthogonal linear polarizations of a birefringent sample [14]. Later, de Boer *et al* used PS-OCT for imaging of thermally damaged tissue [15]. Around the same period, Everett *et al* and Schoenenberger *et al* used PS-OCT to measure birefringence and to generate birefringence maps of porcine myocardium [16, 17]. In 2001,

Hitzenberger *et al* used PS-OCT to generate OCT images depicting phase retardation and fast axis orientation in chicken myocardium [18].

Unfortunately, biological tissue cannot be assumed to be linearly birefringent with a fixed fast axis. Therefore, a complete description of polarization properties of light and sample should use Stokes parameters and Mueller matrices [19]. A PS-OCT system, capable of yielding the full 4×4 Mueller matrix has been presented by Yao and Wang in 1999 [20]. Later in 2002, Yasuno *et al* have presented Mueller matrix images of human skin using spectral interferometry OCT [21]. However, due to the fact that OCT only detects the coherent part of the backscattered light, it is also possible to use the simpler Jones matrix to characterize fully polarized light in OCT [14, 22].

1.2.2 Doppler OCT and OCT flowmetry

All mammalian organs rely on adequate blood flow for nutrient supply and waste disposal. Thus, blood perfusion, the passage of blood through the circulatory system to an organ or tissue, can reflect the health of tissue. In addition, certain circulations, i.e. inner retina circulation and even the entire systemic circulation, are highly regulated to compensate for the metabolic needs of the organ or tissue. Thus, monitoring blood perfusion can also shed light on the functional status of the tissue.

Similar to Doppler ultrasonography, OCT can retrieve flow velocity based on the Doppler Effect. Named after the Austrian physicist Christian Doppler, the Doppler Effect describes that the observed frequency of a wave depends on the relative speed that the source and the observer are moving toward or away from each other. Light scattered back from a sample moving away from the detector shifts to longer wavelength, or appears redder. In the contrary, light scattered back

from a sample moving toward the detector shifts to shorter wavelength, or appears bluer. It is possible for OCT to measure these wavelength shifts, and thus reversely calculating the speed of the moving sample.

In 1997, two groups, Chen *et al* from University of California and Izatt *et al* from Case Western Reserve University, independently reported Doppler OCT measurements of sample velocity using TD-OCT [23, 24]. Though their exact approaches were different, the underlying principles were quite similar. Using inverse Fourier Transform, the back-scattered spectrum was recovered. Its centroid frequency was compared with the carrier frequency, or incident spectrum. They then calculated the Doppler wavelength shift and deduced sample velocity. However, due to the orders of magnitude of difference in the speed of light and blood flow velocity, this technique has sensitivity limitations in biological applications.

Fortunately, a more sensitive technique, phase resolved DOCT, has recently been made possible thanks to the speed advantage of FD-OCT [25, 26]. Phase resolved DOCT acquires sequential depth scans in a rapid consecutive manner. Between each short acquisition interval, the imaged objects, i.e. blood cells, only move a tiny amount comparable to the scale of wavelength. Though this tiny displacement is not directly resolvable in OCT structure images due to resolution limitations, it introduces a phase shift proportional to the displacement on the complex OCT signal. The magnitude of the phase shift $\Delta\varphi$ is related to the sample velocity according to the following formula,

$$\Delta\varphi = 2nk_0v_zT = \frac{4\pi n\delta z}{\lambda_0}, \quad (1.18)$$

where n is the relative refractive index of the medium; $\delta z = v_z T$ is the axial displacement caused by motion; v_z is the axial velocity and T is the acquisition interval; k_0 is the center angular wavenumber; λ_0 is the center wavelength. The scalar term 2 indicates the round trip in the optical path. Thus, rearranging the terms and one can relate the sample velocity to the phase shift using,

$$v = \frac{\lambda_0 \Delta \varphi}{4\pi n T \cos \theta_D}. \quad (1.19)$$

Notably, the word Doppler in the acronym of phase resolved DOCT is somewhat misleading, as the technique does not directly rely on Doppler frequency shift. Specifically, phase resolved DOCT is the direct application of the equation of motion, and can be used even if no Doppler Effect exists. However, the name DOCT is still commonly used to refer this type of OCT flowmetry in accordance with historical conventions.

1.2.3 Spectroscopic OCT and OCT oximetry

Animal tissues contain a variety of chromophores that absorb light in the visible light and – near infrared (NIR) wavelength range. Among them, the concentration of certain chromophores, i.e. melamine and hemoglobin (Hb), are of particular interest as they can reflect the healthiness and functional states of target tissues. For example, high retinal pigment epithelium (RPE) lipofuscin concentration may pose an increased risk factor for age-related macular degeneration (AMD). Thus, measuring RPE lipofuscin concentration can offer an effective screening tool for identifying potential AMD patients and make proactive medical intervention possible [27].

Another intrinsic chromophore, hemoglobin, is the iron-containing oxygen-transport metalloprotein found in the erythrocytes of all vertebrates. Binding with oxygen molecules will

change the optical properties of hemoglobin, leading to two molecular configurations with distinctively different absorption spectra, oxygenated hemoglobin (HbO₂) and deoxygenated hemoglobin (HbR). Thus, it is possible to determine their relative concentration ratio by measuring the effective absorption spectrum of the solution and comparing it with the standard spectra of both HbO₂ and HbR. This relative concentration ratio, also known as hemoglobin oxygen saturation (sO₂), characterizes the percentage utilization of total blood oxygen (O₂) carrying capacity. As the total blood O₂ capacity is unlikely to change significantly during short periods of observation for a given organism, the change in percentage utilization directly reflects the O₂ consumption of regional tissues.

Based on back-scattered photons, OCT is intrinsically sensitive to the optical properties of the sample. In addition, the use of broadband illumination allows retrieving sample absorption spectrum with a single exposure and minimal modification to the system. Following the theoretical analysis in section 1.1, it becomes clear that the power spectrum of the reflected electric field in either arm can be recovered, which were previously explicitly defined as reference and sample electric field reflection coefficients, r and s , respectively. For simplicity, here we assume only the sample reflection coefficient s is the function of wavelength, while the reference reflection coefficient r is a constant and its value assumed to be unity. Equation 1.1 thus can be re written as

$$I_d = \langle |E_d|^2 \rangle = (I_r + I_s) + 2\text{Re}\{sE_1^*(t + \tau)E_1(t)\}. \quad (1.20)$$

Meanwhile, the corresponding auto correlation function is slightly modified to reflect the modulation in the spectrum density,

$$\Gamma'(\tau) = \int_0^\infty sS(\nu)\exp(j2\pi\tau\nu)d\nu, \quad (1.21)$$

Note that Eq. 1.21 takes the form of inverse Fourier transform on $sS(\nu)$. Thus, it is straightforward to perform Fourier transform on $I'(\tau)$ to inversely calculate s . In TD-OCT systems, $I'(\tau)$ can be recovered from the real-valued detector fringes through Hilbert transform, as $I'(\tau)$ is analytic. The first reported application is to retrieve the absorption of colored glass from Morgner *et al* in 2000 [28]. Similarly, FD-OCT can yield the same spectroscopic information by performing windowed Fourier transform on the reconstructed complex OCT signal. Furthermore, due to the fact that optical frequencies are intrinsically unmixed in FD-OCT systems, a more convenient approach, short-time Fourier transform (STFT), can be used directly on the interference spectrum to recover wavelength-dependent OCT signal. This approach is first demonstrated by Leitgeb *et al* later in 2000 [29].

In 2003, Faber *et al* reported the first quantitative measurements of absorption coefficients from diluted and lysed porcine blood sample using NIR-OCT operating around 800 nm [30]. Two years later, semi-quantitative assessment of sO_2 from whole blood *in vitro* was reported by the same group in 2005 [31]. *In vivo* retinal oximetry was later attempted by Kagemann *et al* in 2007 [32], and Lu *et al* in 2008 [33], where both groups used NIR-OCT. However, only qualitative results were obtained. It was not until the adoption of visible-light OCT (vis-OCT) when quantitative blood sO_2 was obtained from mouse dorsal skin fold window by Robles *et al* in 2011 [34] and in rat retinal circulation by Yi *et al* in 2013 [35].

1.3 Challenges of OCT

The rapid development of the OCT imaging modality over the past decade is not unchallenged by difficulties. Following lists some major issues that prevent with current OCT applications from acquiring even higher quality anatomical image or functional information.

1.3.1 Multiple scattering

Biological tissues, including whole blood, are highly optical scattering media and will lead to multiple scattering of the OCT probing light. A photon that goes through multiple scattering events may have different accumulative optical path length from its actual physical depth, which leads to inaccurate localization of photons, image blurring, and signal strength reduction [36-38].

Though Thrane *et al* have analytically investigated the effects of multiple scattering in OCT anatomical imaging in as early as 2000 [39], it remains a major challenge in today's high resolution application. More importantly, it is unclear how multiple scattering affects functional OCT imaging, especially in spectroscopic OCT where absorptive optical attenuation also depends on the specific path experienced by a photon.

1.3.2 Imaging resolution

Despite the fact that axial and lateral imaging resolutions are decoupled in most OCT systems, they still have their corresponding physical limitations. Until recently, the record of OCT axial resolution was around 1 μm [40]. Using an objective with higher NA can potentially bring lateral

resolution close to the diffraction limit; however, the resulting short Rayleigh range also reduces imaging depth.

In addition, current methods for spectroscopic OCT analysis has intrinsic tradeoffs between axial and spectral resolution due to the uncertainty principle, also known as the Gabor limit. Although there exists certain walk-arounds to approximate the limit or enhance the apparent resolution, i.e. using of wavelet transform and dual-window approach [41], the underlying fundamental remains unchanged. Thus, caution must be asserted when performing spatial-spectral analysis in OCT. In short, if one wants to increase the spectral resolution, one effectively loses axial resolution, and vice versa.

1.3.3 Imaging contrast

Optical properties between different types of biological tissues are often very similar. In addition, they almost always exhibit high optical scattering potential. When performing anatomical and functional analysis on OCT images, it is often difficult or impossible to differentiate signal from the target region-of-interest (ROI) and surrounding background tissue. Thus, the need for complicated imaging segmentation algorithms often makes quantitative imaging analysis tedious and susceptible to image quality problems.

In addition, label-free visualization of micro structure using intrinsic contrast is often desirable in the context of clinical diagnosis imaging to minimize invasiveness. Thus it is worthwhile to investigate methods to enhance OCT contrast from otherwise non-resolvable features either due to smaller size or insufficient absorption/scattering contrast.

1.3.4 Noise and speckle in OCT imaging

OCT, like any other imaging systems, is susceptible to noise. Common noise sources in OCT imaging system include the discrete arrival of photons (shot noise), excess noise (laser instability), and receiver noise (thermal noise, dark current, and readout noise) [42]. In an ideal or well-designed system, the lower limit of noise is approximately shot noise [42, 43]. The existence of noise will inevitably bias quantitative measurement, especially in lower SNR images.

In addition, the use of coherent illumination introduces speckle into OCT images. Though speckle can be related to micro structures of the sample, in many cases it is treated as noise [44]. Thus, the challenge is how to interpret speckle in OCT images. If it is treated as imaging contrast, what structural and functional information does it provide? If treated as noise, how to minimize its interference both aesthetically and in quantitative analysis?

1.3.5 Selection of wavelength bands in OCT imaging

Multiple wavelength bands have been demonstrated in OCT systems. Traditionally, NIR bands with center wavelength ranging from 800 nm to 1300 nm are used. Within this spectral range, biological tissues often exhibit minimal optical absorption and scattering, allowing deeper imaging depth and higher resolution. This choice of illumination source also largely coincide with commercial availability of broadband light sources suitable for low-coherence interferometry. Recently, OCT systems using illumination source within the visible-light spectrum, so called visible-light or white-light OCT, is reported. The claimed advantage of vis-OCT is that it has higher imaging resolution and, more importantly, higher spectroscopic sensitivity to enable OCT oximetry *in vivo*.

However, due to the drastically different optical properties between the visible and NIR wavelength range, it is unclear how the choice of wavelength bands will affect the quality of OCT imaging, both anatomically and functionally. Thus one question is raised: what is the optimal wavelength bands of choice in OCT imaging?

1.4 Scope of the dissertation

The studies included in this dissertation work have one major focus: using spectroscopic OCT analysis to recover functional blood hemoglobin oxygen saturation *in vivo*. In the aim of providing accurate and robust sO₂ measurements, it also attempts to solve or provide some insight into the aforementioned challenges. Especially, the optical wavelength range for OCT oximetry is investigated in chapter 2. In the same chapter, the effects of multiple scattering on the quality of OCT image and accuracy of OCT oximetry is also investigated. Then, chapter 3 seeks to address the imaging contrast concern using OCT angiography. Subsequent applications in rodent and human studies are presented in Chapter 3 and 4, respectively. Finally, chapter 5 presents an OCT imaging application beyond ophthalmic imaging by monitoring hemodynamic change on mouse cortex *in vivo*.

1.4.1 Organization of the dissertation

Each chapter begins with an introduction outlining the significance of the reported study and a concise literature review is performed.

Chapter 2 uses numerical simulation and a dual-band OCT system trying to answer the question of optimal wavelength bands for OCT oximetry. In addition, imaging quality such as visualized anatomical features, resolution, other functional imaging aspects including Doppler OCT flowmeter is investigated.

Chapter 3 investigates the possibility of combining OCT angiography and oximetry to retrieve sO_2 information from otherwise non-resolvable vessels. Especially, relative sO_2 fluctuation within choroidal capillaries following inhalation oxygen challenge is reported for the first time. It also investigates the possibility of using narrower wavelength bands to reduce light exposure and provide robust results.

Chapter 4 presents a translational study where the established vis-OCT system is applied to human studies. The feasibility of OCT oximetry on human retinal imaging is established using a prototype system.

Chapter 5 extends the application of vis-OCT oximetry beyond ophthalmological applications. Especially, vis-OCT is used to monitor hemodynamic changes in mouse cortex after surgically induced ischemic stroke. This provides a proof of concept that vis-OCT oximetry can also work in highly turbid tissue medium, i.e. cortex. In addition, it reveals hemodynamic parameters within mouse cerebral circulation during both normal condition and after surgically induced focal ischemia.

Finally, a conclusion and outlook of this dissertation is given in Chapter 6.

CHAPTER 2

Illumination wavelength and its effects on anatomical and functional OCT imaging

Optical coherence tomography (OCT) has demonstrated tremendous success in imaging three dimensional (3D) tissue anatomy with micrometer-level spatial resolution on a macroscopic length scale [45]. In the past two decades, the technique has been translated into various clinical practices [46]. In particular, OCT has joined the standard of care in ophthalmology, providing rich 3D anatomical images from various retinal layers, choroid, and optic nerve head. Besides the technical advances on high-speed and high-resolution retinal imaging, functional imaging of various hemodynamic parameters has emerged as an invaluable supplement to anatomical OCT imaging.

This chapter seeks to answer the question that how the wavelength band used in OCT illumination affects image quality, and more importantly, the performance of functional OCT. A major emphasis is placed on OCT retinal oximetry, which is the key aspect of the work presented throughout this dissertation. The first part this chapter introduces a numerical simulation approach based on the Monte Carlo method. In the second part, a visible-light and near infrared (NIR) dual-band OCT system is designed and implemented. Visible and NIR OCT images are simultaneously acquired *in vivo* to appreciate their similarities and differences.

2.1 Introduction

Most commercially available OCT systems operate within the near infrared (NIR) range of the electromagnetic spectrum, i.e. having a center wavelength around 800 nm or 1300 nm. Several factors have backed its adoption. First, biological tissues (blood, cell matrix, melanin, etc.) exhibit minimal optical absorption and scattering within the NIR range among usable optical bands [47]. Second, broadband NIR light sources, especially superluminescent diodes (SLD), are commercially accessible and more economically viable than their visible counterparts during the time period of OCT developments [1]. Third, NIR spectrum range falls out of the human visual perception, making it less intrusive when performing ophthalmological scanning and other examinations.

Unfortunately, the use of NIR illumination acts as a double-edged sword for spectroscopic OCT analysis. The lower optical absorption experienced by the probing beam often translates to reduced spectral contrast in the acquired spectroscopic image, making inverse calculations challenging and susceptible to noises. For OCT oximetry specifically, the optical absorption coefficients (μ_a) of oxygenated (HbO₂) and deoxygenated (HbR) hemoglobin are much lower and have arguably less usable contrast in the NIR wavelength range. In addition, tissue optical scattering coefficients (μ_s) become orders of magnitude larger than blood μ_a , overshadowing contrast contributions from blood absorption. Thus, NIR illumination may not be ideal if accurate quantification of sO₂ is desired, which was first reported by Faber *et al* [48].

Visible-light OCT (vis-OCT) is then proposed to address the issue. Within the spectral range from 500 to 600 nm, blood μ_a is over ten times higher than that in the NIR region. More importantly, HbO₂ and HbR absorption spectra have opposing trends and share multiple isosbestic points [49],

which facilitate the inverse calculation. In addition, vis-OCT intrinsically has higher axial resolution than NIR-OCT with comparable bandwidth because a shorter wavelength range is used [50]. Collectively, these advantages offer an opportunity to optically determine sO_2 with high accuracy, as demonstrated in *ex vivo*, *in situ* and *in vivo* experiments [34, 35].

Although vis-OCT oximetry has shown great potential, several uncertainties need to be thoroughly investigated for accurate sO_2 measurement before it can be successfully translated into clinics. First, it is not clear how physiological variations and sampling strategy affect the accuracy of sO_2 measurements. Maintaining high accuracy and precision is very important regardless of physiological and pathological variation of physiological parameters such as vessel diameter and actual oxygenation value.

Second, it is not clear how visible-light compares with NIR illumination in terms of anatomical imaging quality and functional aspects other than oximetry. Despite its higher spectral contrast, vis-OCT also suffers from lower penetration depth and often has sub-optimal signal-to-noise ratio (SNR) in deeper regions. Thus, it is desirable to compare OCT images from two wavelength range to appreciate their respective performance.

Third, Vis- and NIR-OCT may possess different imaging contrasts due to diverging tissue optical properties. An uninformed physician may find the discrepancy confusing. These discrepancies are best appreciated if both visible and NIR OCT images of the same sample is compared side-by-side.

The first part of this chapter employs numerical Monte Carlo simulation of OCT oximetry by focusing on a specific application, the retinal OCT oximetry. The numerical simulation seeks to

answer two questions: (1) what is the optimal wavelength range for OCT oximetry; and (2) how physiological variations affect its accuracy.

In the second part, a visible/NIR dual-band OCT system is constructed to compare anatomical and functional OCT imaging capability within the two wavelength bands side-by-side. The simultaneous acquisition of both vis- and NIR-OCT images eliminate most confounding factors that exist when obtained using different systems. Thus, it serve as a fair comparison between the OCT images using the two illumination spectral bands.

2.2 Investigating the optimal wavelength band and accuracy of OCT oximetry: a Monte Carlo study

Monte Carlo (MC) simulation is a statistical numeric method to identify approximate solutions of stochastic processes. This method is often used to study light-tissue interactions, where finding analytic solutions is technically challenging. Although Monte Carlo simulation does not usually track phase information of photons, the feasibility of Monte Carlo simulation of OCT (MC-OCT) was demonstrated by several groups [38, 51-53]. By simulating the behavior of photon packets traveling across different layers and blood vessels in the retina, one can achieve a numerical approximation of real experimental OCT signals.

In this section, a Monte Carlo simulation algorithm is conducted on a simplified four-layer eye model to investigate the suitable wavelength band to be used in OCT oximetry. Its accuracy is also established following variations of simulated parameters within physiological range.

2.2.1 Monte Carlo simulation model and algorithms

2.2.1.1 Simplified four-layer eye model

Figure 2.1(a) illustrates the major anatomical structures of the human eyeball. A three dimensional four-layer model is subsequently adopted to describe the structures found in the posterior segment. The four layers are neural retina, retinal pigment epithelium (RPE), choroid, and sclera, as shown in Fig. 2.1(b) [54]. The respective thicknesses of these layers are set to 200 μm , 10 μm , 250 μm , and 700 μm based on literature reports [54, 55]. The lateral boundary of each layer extends to infinity. The blood vessel is modeled as an infinitely long cylinder imbedded in the retinal layer and parallel to the retina surface. Its diameter varies from 40 μm to 160 μm based on the specific aims of each simulation run [56]. The vessel wall thickness is set to be 10% of the lumen diameter [57]. Blood is treated as a homogenous medium inside the vessel. It has been shown that this simplified model is sufficient for retinal photon-tissue interaction simulation since other posterior ocular tissues (such as vitreous humor) are either relatively thin or optically transparent [55, 58].

The optical properties used in the simulation for all solid tissues, including absorption coefficient μ_a [cm^{-1}], scattering coefficient μ_s [cm^{-1}], and anisotropy g [dimensionless], can be found in the literatures [59, 60], and are summarized in table 2.1. They exhibit little variation within either the visible or NIR spectral band, and are subsequently treated as constant values within the two bands respectively.

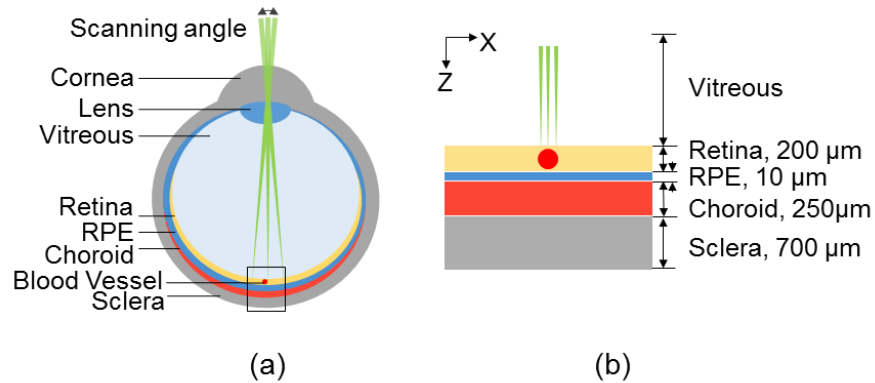


Figure 2.1 Simplified eye model used in the numerical Monte Carlo study. (a) Schematic diagram of a human eyeball during OCT imaging. (b) Dimensions and relative positions of the four simulated layer structures from the posterior segment (not to scale). A cylindrical blood vessel is imbedded in the retina layer parallel to surface.

Table 2.1 Optical properties (μ_a [cm^{-1}], μ_s [cm^{-1}], and g [-]) of solid ocular tissue used in the Monte Carlo Simulation

		Visible (520 nm – 610 nm)	NIR (750 nm – 840 nm)
Retina	μ_a	5	1
	μ_s	319	224
	g	0.97	0.97
RPE	μ_a	938	385
	μ_s	1068	1469
	g	0.84	0.84
Choroid	μ_a	224	27
	μ_s	711	484
	g	0.94	0.94
Sclera	μ_a	4	0.4
	μ_s	96	61
	g	0.90	0.90
Blood vessel wall	μ_a	9	2
	μ_s	284	140
	g	0.84	0.84

2.2.1.2 Absorption and scattering properties of whole blood

Erythrocytes, or the hemoglobin content within erythrocytes, are the major absorbing chromophore of whole blood. Given the molar extinction coefficient of HbO₂ (ϵ_{HbO_2}) and HbR (ϵ_{HbR}) (in cm⁻¹Mole/L), one can calculate the absorption coefficients of whole blood using [61]

$$\mu_a = 2.3 \times [HbT] \times \frac{\epsilon_{HbO_2} \times sO_2 + \epsilon_{HbR} \times (1-sO_2)}{W_{HbR}}, \quad (2.1)$$

where [HbT] (in g/L) is the concentration of total hemoglobin; sO₂ [dimensionless] is the hemoglobin oxygen saturation; W_{HbR} is the molecular weight (MW) of the hemoglobin, which is roughly 64500 [g/Mole]. The difference between the MW of HbO₂ and HbR is neglected as the MW of oxygen is much smaller than that of the hemoglobin molecule. The absorption coefficients of fully oxygenated (μ_{a_OxyB}) and deoxygenated (μ_{a_DeOxyB}) whole blood can be obtained by plugging sO₂ = 1 or 0 in Eq. 2.1, respectively. Prior to each simulation, the blood μ_a is predetermined using an sO₂ within the physiological range from 0.4 to 0.98 [62].

Similarly, the scattering coefficient of whole blood, μ_s , is also sO₂-dependent. Using the Kramers–Kronig relationship and the Mie solution for the Maxwell equation, one can calculate the wavelength-dependent scattering coefficients of oxygenated (μ_{s_OxyB}) and deoxygenated (μ_{s_DeOxyB}) whole blood following the literature [63]. However, this treatment assumes that particles (erythrocytes) scatter light independently, which actually is not entirely true. Consequently, the obtained μ_{s_OxyB} and μ_{s_DeOxyB} spectra have similar spectral shape to what was previously reported, but with considerably larger values [64-66]. As dependent scattering, or coherent scattering, happens due to densely packed erythrocytes in whole blood, a scaling coefficient is needed to bridge the difference between dependent and independent scattering

coefficient. This hematocrit-dependent scaling coefficient is known as the packing factor W [dimensionless]. In physiological context, W and hematocrit H [dimensionless] roughly follows the following relationship over both the visible and NIR spectral range [66],

$$W = (1 - H)^2. \quad (2.2)$$

Using the mean physiological value of $H = 0.45$, a packing factor $W = 0.3$ is empirically chosen to scale the raw spectra obtained from the Mie theory. Thus, the expression for the sO_2 -dependent whole blood scattering coefficient is,

$$\mu_s = W \cdot \mu_{s_{OxyB}} \times sO_2 + W \cdot \mu_{s_{DeOxyB}} \times (1 - sO_2). \quad (2.3)$$

The anisotropic factor, g , does not show significant wavelength dependency in either spectral range. Blood oxygen level also has little effect on its value. Thus, g is fixed at 0.987 for the visible band and 0.983 for the NIR band, respectively. Table 2.2 summarizes the absorption coefficients and unscaled scattering coefficients from Mie theory within the simulated wavelength range.

Table 2.2 Optical properties of whole blood within the simulated wavelength bands. All coefficients are of unit [cm^{-1}].

	λ [nm]	μ_{a_OxyB}	μ_{a_DeOxyB}	μ_{s_OxyB}	μ_{s_DeOxyB}
Visible	520	121.0	152.6	3626.3	3396.6
	525	150.7	168.1	3547.2	3339.5
	530	189.4	185.0	3459.0	3283.0
	535	224.0	201.3	3387.4	3230.1
	540	241.9	217.4	3353.1	3180.6
	545	234.0	233.0	3365.5	3136.1
	550	204.1	244.7	3407.4	3103.3
	555	174.0	249.1	3436.1	3085.9
	560	160.8	244.6	3427.1	3085.1
	565	172.9	230.3	3373.5	3097.8
	570	210.3	211.6	3289.4	3112.0
	575	244.0	193.4	3238.0	3121.5
	580	224.8	176.9	3291.1	3126.7
	585	150.7	160.6	3415.2	3132.4
	590	77.9	136.6	3504.6	3150.2
	595	36.9	104.7	3527.5	3172.7
	600	18.5	77.2	3513.4	3178.0
	605	10.8	60.6	3485.3	3163.6
610	7.8	48.3	3452.7	3144.2	
Near infrared	750	2.7	7.3	2653.2	2366.0
	755	2.9	7.9	2628.3	2341.9
	760	3.0	7.9	2603.7	2319.1
	765	3.2	7.4	2579.4	2296.9
	770	3.4	6.7	2555.3	2274.8
	775	3.5	6.1	2531.5	2252.8
	780	3.7	5.5	2508.0	2230.9
	785	3.8	5.0	2484.8	2209.1
	790	3.9	4.6	2461.8	2187.5
	795	4.1	4.2	2439.1	2166.1
	800	4.2	3.9	2416.5	2144.6
	805	4.4	3.8	2394.0	2123.2
	810	4.5	3.7	2372.1	2102.3
	815	4.6	3.6	2350.4	2081.7
	820	4.7	3.6	2328.9	2061.3
	825	4.9	3.6	2307.6	2041.1
	830	5.0	3.6	2286.6	2021.2
	835	5.2	3.6	2265.8	2001.6
840	5.3	3.6	2245.3	1982.2	

2.2.1.3 Monte Carlo Simulation

The MC-OCT simulation is implemented in MATLAB (2012 a, Mathworks, Inc.) based on the MCML code by Wang *et al* [51]. Figure 2.2 shows the flowchart for simulating OCT amplitude image at the given optical wavelength. First, the model geometry and tissue optical parameters, including μ_a and μ_s , are initiated to the values established in section 2.2.1.1 and 2.2.1.2. Then, a photon packet with unit initial weight is launched and traced. The path length and energy deposition of the photon packet at every scattering event site are recorded. The tracing is terminated if (1) the photon packet exists the tissue boundary, or (2) its weight is sufficiently small (<0.0001) and does not survive the roulette test [51]. In addition, the tracing is also terminated if the cumulative path length exceeds a pre-defined threshold value (100 μm below the retina layer). This treatment has little or no effect on the simulated OCT signal from within blood vessels, as both real OCT imaging and MC-OCT simulations are depth resolved [52, 67]. However, it can greatly reduce the execution time.

When the photon packet exits the model from the upper surface, its propagation direction is compared with the pre-defined collection angle of the MC-OCT detection scheme. The photon packet is considered “detectable” if it falls into the collection cone of 4.2° , which corresponds to a numerical aperture (NA) of 0.1 for tissue with refractive index $n = 1.38$. Otherwise, it is discarded (undetected). For each detected photon packed, its weight and cumulative path length are recorded for OCT image construction and sO_2 estimation. Finally, a new photon packet is launched and the entire process is iterated until a stable solution is reached. In order to accelerate the simulation on multi-core computer systems, parallel computing is implemented on the level of launch angles, or A-lines, as they are independent from each other.

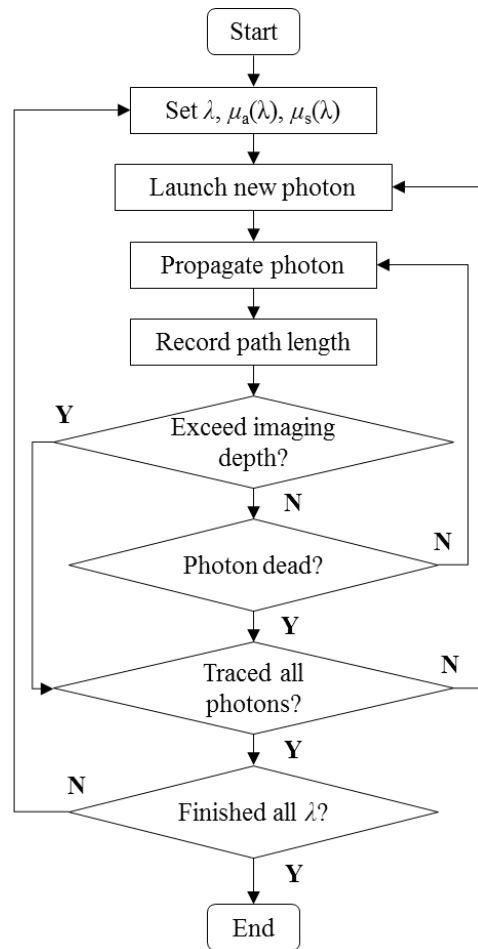


Figure 2.2 Flowchart of the implemented Monte Carlo simulation algorithm for generating spectroscopic MC-OCT signal.

The simulated MC-OCT B-scan is reconstructed by projecting the detected photon packets onto the Cartesian coordinate using its launch angle, cumulative path length, and weight. The launching angle is so chosen that each reconstructed A-line represents $1 \mu\text{m}$ in the grid laterally. It is worth noting that the process neglects the finite resolution and sensitivity roll-off found in real OCT imaging process due to limited illumination bandwidth and spectral resolution. However, these effects demonstrate little interfere with the subsequent spectroscopic analysis and are not considered in the simulation.

To generate spectroscopic OCT signal in MC-OCT, the entire simulation is repeated for various optical wavelengths. For the visible spectral range, the simulated wavelength band covers 520 nm to 610 nm; and for the NIR spectral range, the bands covers from 750 nm to 840 nm. Each band is discretized at a 5 nm interval. For each simulated wavelength point, the blood optical properties are averaged from the neighboring ± 5 nm wavelength range.

2.2.1.4 Estimating sO₂ Value

The back-scattered spectrum, I , is taken from the mean MC-OCT intensity from a rectangular region-of-interest (ROI) within the blood vessel. The size of the ROI are 3 μm and 20 μm along the lateral and axial directions, respectively. To inversely calculate the blood sO₂ associated with each simulated vessel, the following model is constructed based on the Beer-Lambert law [29],

$$I = I_0 \cdot r \cdot \exp\left(-2d \cdot \mu_{t_OxyB} \cdot sO_2 - 2d \cdot \mu_{t_DeOxyB} \cdot (1 - sO_2)\right), \quad (2.4)$$

where I_0 [arb. u.] is the intensity of incident light; d [cm] is the vessel diameter; r [dimensionless] is the reflectance from the tissue. The spectrum of r can be expressed by a power law $r(\lambda) = A\lambda^\alpha$ under the first Born approximation, where A is a constant [68, 69]. μ_{t_OxyB} [cm^{-1}] and μ_{t_DeOxyB} [cm^{-1}] are the compound attenuation coefficients of fully oxygenated and fully deoxygenated whole blood, respectively. Both μ_{t_OxyB} and μ_{t_DeOxyB} are the linear combination of the absorption coefficients, scattering coefficients, and the packing factor of whole blood [70],

$$\begin{aligned} \mu_{t_OxyB} &= \mu_{a_OxyB} + W \cdot \mu_{s_OxyB}, \\ \mu_{t_DeOxyB} &= \mu_{a_DeOxyB} + W \cdot \mu_{s_DeOxyB}. \end{aligned} \quad (2.5)$$

Plugging in the expression for $r(\lambda)$ and performing a logarithm operation on both sides of the Eq. 2.4, one can reach,

$$\ln\left(\frac{I}{I_0}\right) = 2d[sO_2 \cdot (-\mu_{t_OxyB} + \mu_{t_DeOxyB}) - \mu_{t_DeOxyB}] + \ln(A) + \alpha \cdot \ln(\lambda), \quad (2.6)$$

which is a function of λ . Based on the notion that sO_2 cannot be less than zero or greater than one, a constrained least squares fitting can be performed to estimate sO_2 , d , $\ln(A)$, and α .

2.2.1.5 Cross-verification of MC-OCT results against animal experiments *in vivo*

The optical properties of rat blood are similar to that of human blood. It is reasonable to use experimental data obtained from rat fundus OCT images to cross-verify the selection of W in terms of accuracy of OCT oximetry [35]. A pigmented rat (Long Evans, Harlan Laboratories) was anesthetized using 1.5% isoflurane and oxygen/nitrogen gas mixture similar to air. Prior to image, 0.5% Tetracaine Hydrochloride ophthalmic solution was applied to the rat eyes for local anesthesia, and 1% Tropicamide ophthalmic solution to dilate the pupil. It was then transferred to a customized imaging stage for vis-OCT imaging. During the experiment, the inhalation gas compound was deliberately controlled and the systemic arterial spO_2 was monitored to be exactly 0.7 by a pulse oximeter attached to the rat's rear feet. During imaging, artificial tears was applied every other minute to keep the rat cornea moisturized. The rats were removed from the imaging setup immediately after the experiment and allowed full recover.

2.2.2 Simulation results

2.2.2.1 Validity and stability of the MC-OCT simulation

The validity of the MC-OCT algorithm was cross-verified against the established MCML code from Wang *et al* [51] using the four layer eye model without the imbedded vessel. The two algorithms gave almost-identical results. Figure 2.3(a) is a simulated B-scan image using the MC-OCT MATLAB code. The layered anatomic structures of retina, RPE, and the blood vessels can be clearly identified, and agree with the eye model described earlier.

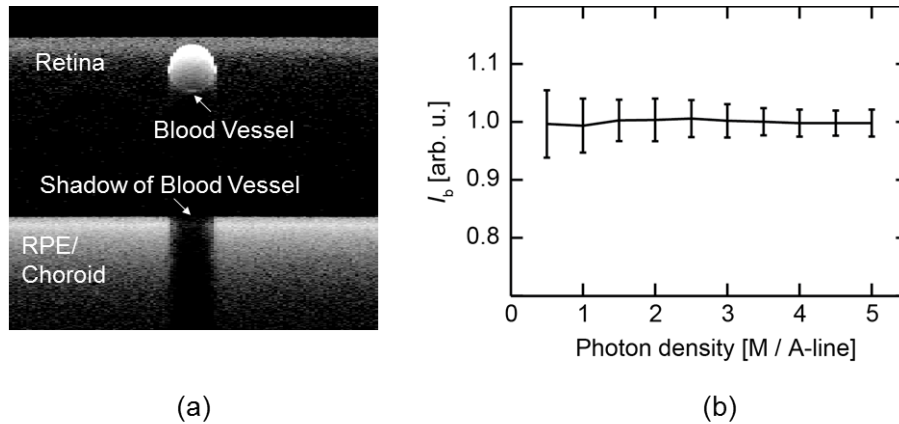


Figure 2.3 (a) A sample simulated MC-OCT B-scan imaging. The labeled structures corresponds well to the constructed four-layer eye model. (b) Mean and standard deviation of back-scattered intensity (I_b) from 10 simulation runs at each photon density level.

A stability test is performed to establish the optimal cycles of iteration. The mean optical properties within the simulated visible wavelength range are assigned to the eye model. The vessel diameter is fixed at $100 \mu\text{m}$ and blood sO_2 is set to 70%, respectively. Figure 2.3(b) plots the mean value and standard deviation of MC-OCT intensity from a rectangular ROI ($3 \mu\text{m}$ lateral \times $20 \mu\text{m}$ axial) near the bottom of the blood vessel, each calculated from 10 simulation runs at the given photon packet density. The photon packet density is defined as number of photon packets per

simulated A-line, or launching angle, and ranges from 0.5 million (M) to 5 M with a step size of 0.5 M. The mean back-scattered MC-OCT intensity shows no significant fluctuation against increasing number of photon packets simulated. In contrast, the standard deviation gradually decreases as photon packet density increases, indicating that larger iteration cycles provides more stable solutions. When the number of photon packets exceeded 3.5 M per A-line, the marginal improvement becomes insignificant. Thus, 4 million photons per A-line is chosen as the optimal iteration cycle in all subsequent analysis. When executed on a workstation equipped with dual Intel Xeon E5645 CPU at 2.40 GHz and 24 GB of memory, the MATLAB algorithm throughput was about 30 minutes per A-line.

2.2.2.2 Accuracy of OCT oximetry and the choice of wavelength bands

To establish the optimal wavelength range for OCT oximetry, the MC-OCT simulation is carried out in both visible and NIR range for inverse sO_2 calculation. The simulated visible spectral range is from 520 nm to 610 nm; while the simulated NIR spectral range is from 750 nm to 840 nm. Both wavelength bands are chosen to include isosbestic points within each range for maximum spectral contrast and inverse calculation stability [66, 71]. The geometry and blood oxygenation are kept constant (vessel diameter = 100 μm , and $sO_2 = 70\%$) throughout the entire simulation. The packing factor W is empirically chosen to be 0.3 as explained earlier.

The back-scattered MC-OCT intensity spectra are sampled from a rectangular ROI (3 μm lateral \times 20 μm axial) near the bottom of the blood vessel. Figure 2.4 compares the normalized back-scattered spectrum from the simulated visible and NIR wavelength bands, respectively. A non-negative least squares fitting is subsequently performed to retrieve blood sO_2 . The fitting algorithm converged nicely on the MC-OCT spectra simulated using visible spectral range, which

yields $sO_2 = 0.71 \pm 0.025$. In contrast, the same fitting algorithm failed to converge for the MC-OCT spectra obtained using NIR spectral range. The solid line in Fig. 2.4(b) represents one case of many divergent solutions, and no usable sO_2 value is obtained.

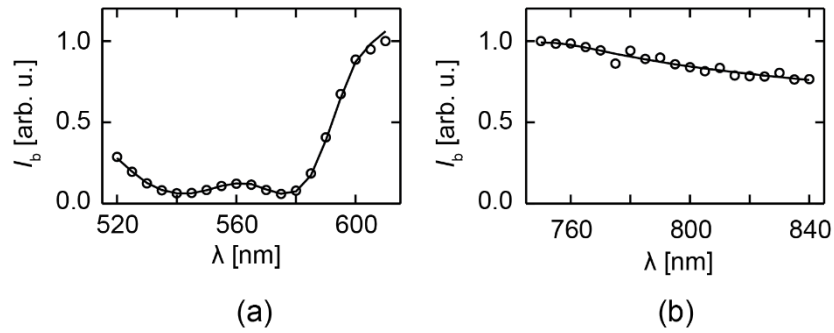


Figure 2.4 Normalized back-scattered intensity (I_b) from (a) visible wavelength range; and (b) NIR wavelength range. The solid line is obtained by least squares fitting all spectral points against known whole blood compound attenuation coefficients. The algorithm does not converge for NIR data, and one representative case is plotted in (b).

This result is not unexpected if one compares the compound attenuation coefficient spectra ($W = 0.3$) of fully oxygenated blood μ_{t_OxyB} and deoxygenated blood μ_{t_DeOxyB} between the visible and NIR wavelength bands in Fig. 2.5, where. While μ_{t_OxyB} and μ_{t_DeOxyB} clearly have different spectral shape within the visible range, they share the same trend and are almost parallel to each other in the NIR range. In addition, one can plot the spectra for $sO_2 = 70\%$ whole blood on top of both plots. While the visible spectra is clearly the mixing of two different spectral shape, the NIR spectra can be obtained by scaling either of the the NIR μ_{t_OxyB} or μ_{t_DeOxyB} spectrum. Thus, the NIR situation corresponds to solving the inverse equation using two linearly-dependent inputs. Until a more advanced fitting algorithm is developed, this poses a major hurdle for sO_2 measurements using NIR wavelength range. Therefore, visible light is currently the preferred

choice for OCT oximetry applications, and all subsequent analysis primarily focus on the accuracy of vis-OCT oximetry.

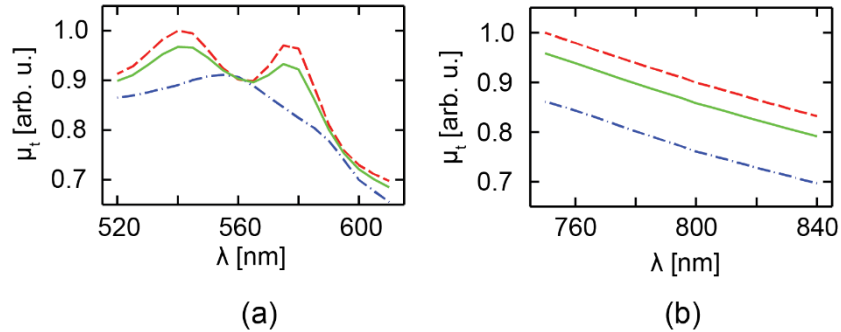


Figure 2.5 Normalized compound attenuation coefficient μ_t for (a) visible wavelength range; and (b) NIR wavelength range. The red dashed curve represents fully oxygenated blood μ_{t_OxyB} ; the blue dot-dash curve represents fully deoxygenated blood μ_{t_DeOxyB} ; the green solid line represents whole blood compound attenuation coefficient when $sO_2 = 70\%$.

2.2.2.3 Accuracy of vis-OCT oximetry under physiological variations

Physiological parameters, including vessel diameter and blood sO_2 , can demonstrate large variations in both normal and pathological condition. So it is important that OCT oximetry can retrieve accurate true sO_2 values regardless of interferences. In this section, the accuracy of vis-OCT oximetry is verified against various pre-set blood oxygenation level and vessel diameters.

The first factor being examined is whether vis-OCT oximetry can accurately reflect blood sO_2 variations. The vessel diameter is fixed at $100 \mu m$, while the blood sO_2 varies from physiological values from 40% to 98%. Two sampling ROI's are used to retrieve back-scattered MC-OCT intensity. As illustrated in the insert of Fig. 2.6(a), one ROI is located in the middle of the blood vessel (MD); the other is placed near the bottom of the vessel (BT). The sO_2 values are subsequently retrieved from least squares fitting for each individual preset sO_2 and sampling

location, respectively. Plotted against pre-set values in Fig 2.6(a), the inversely calculated sO_2 from MC-OCT simulation always deviate less than 5% from the expected value. A linear regression also showed strong positive correlations ($R^2 = 0.99$) between the calculated value and pre-set value for both sampling locations, indicating that OCT oximetry can accurately measure sO_2 . In addition, there is no significant difference between the MD and BT sampling location. Thus, the BT ROI is used for all subsequent analysis.

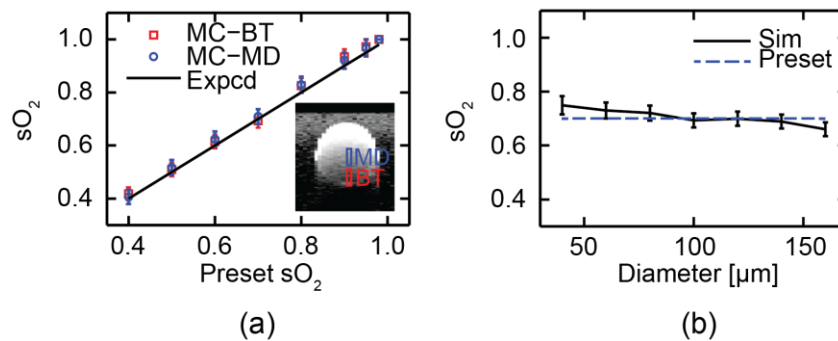


Figure 2.6 Investigating the accuracy of vis-OCT oximetry. (a) The accuracy of vis-OCT oximetry with respect to preset blood sO_2 . Vessel diameter is fixed at 100 μm . Two ROI location is investigated, one is placed in the middle of the vessel (blue box, MD), and the other is near the bottom of the vessel (red box, BT). The solid black line is the expected value. (b) The accuracy of vis-OCT oximetry with respect to varying vessel diameter in the physiological range. Blood sO_2 is fixed at 70% (blue dashed line). The sampling ROI is placed near the bottom of the vessel.

Secondly, the influence of blood vessel diameter on the accuracy of sO_2 estimation is investigated [55, 71]. For this purpose, the blood sO_2 level is set to a constant value of 70%, while vessel diameter is varied from 40 μm to 160 μm according to anatomical findings [56, 72]. Figure 2.6(b) plots the inversely calculated sO_2 values against increasing vessel diameter. No statistically significant difference is found within the simulated diameter range. However, a gradually descending trend can be observed. A closer look at the simulated MC-OCT signal reveals that back-scattered intensity is extremely low for larger vessels due to longer attenuation path length.

This leads to lower SNR, and thus, underestimation from the least squares fitting algorithm. Despite being statistically insignificant, this phenomenon suggests a tradeoff when selecting optimal sampling ROI. While a deeper ROI is usually accompanied by larger optical attenuation from blood, it also suffers from lower signal strength, and thus, lower SNR and sub-optimal OCT oximetry performance. Thus, to ensure the accuracy of sO_2 measurements, caution must be asserted when selecting the ROI for OCT oximetry. The sampling location should (1) have sufficient attenuation path length to create sufficient spectral contrast, and (2) have reasonably high SNR to ensure optimal fitting performance.

2.2.2.4 Experimental verification of the chosen Packing factor W

The choice of appropriate W is crucial for accurate sO_2 estimation. Unfortunately, W depends on blood hematocrit H , and may vary among different individuals. When the actual W value is not readily available in clinical settings, it is critical that an empirically-chosen one can provide sufficiently accurate results. The MC-OCT simulation in this section seeks to answer this question by investigating how inversely calculated sO_2 changes when fitted using W ranging from all possible values from 0 to 1. Meanwhile, vessel diameter and blood sO_2 are kept constant to 100 μm and 70%, respectively.

The inversely calculated sO_2 values from MC-OCT simulation are plotted in solid line against W in Fig. 2.7. It appears that in the interval from $W = 0.2$ to $W = 0.4$, fitted sO_2 is reasonably accurate with respect to the pre-set value, having estimation error less than 5 percentage points. Significant under-estimation over 20% can be found when W is less than 0.1 or greater than 0.4.

In addition, the effect of W is further investigated using experimental data from the vis-OCT system previously reported [35]. The back-scattered intensity within an artery with known oxygen

saturation of 70% is sampled in the same manner as in MC-OCT simulations. The corresponding sO_2 is inversely calculated using least squares fitting with W ranging from 0 to 1 and plotted on top of Fig. 2.7. The experiment result agrees with the simulation.

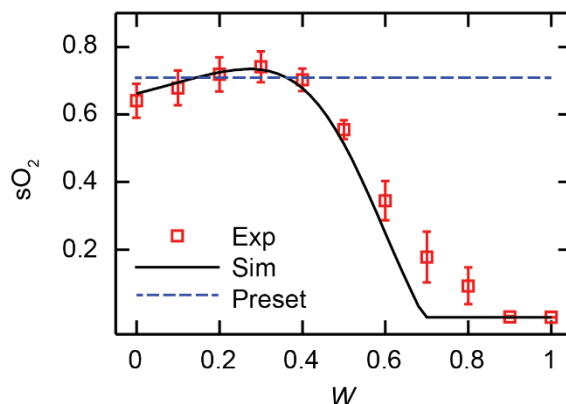


Figure 2.7 Inversely calculating sO_2 using all possible packing factor W values ranging from 0 to 1. The blood sO_2 is fixed at 70% for both the numerical simulation and vis-OCT animal experiment (blue dashed line). The black solid curve represents results obtained using MC-OCT (Sim). The red box represents experiment results obtained by vis-OCT imaging of rat retinal circulation *in vivo* (Exp).

Both the numerical simulation and experimental data imply that a W value between 0.2 and 0.4 may be empirically used for OCT oximetry application. However, it is recommended that W should be selected after being calibrated against known hematocrit value.

2.2.3 Discussion

The Monte Carlo simulation suggests that visible-light is the preferred wavelength band when performing OCT oximetry. It can provide accurate and stable sO_2 measurements regardless of physiological variations in blood oxygenation, vessel diameter, or sampling location. However, the presented numerical approach does not take detection noise into consideration. Thus, caution

must be asserted in real experimental setups, especially regarding the proper selection of sampling ROI. Specifically, one may want to employ different strategies based on vessel diameter to maximize spectral contrast, and eventually the accuracy of sO_2 . In smaller vessels, the bottom surface provides good reflectance signal due to the refractive index mismatch between blood and the vessel wall. The photons sampled at the bottom finished one entire round-trip inside the blood vessel, and such double passing improves spectral contrast due to longer absorption length. In larger blood vessels, however, strong attenuation reduced photon packets survive such longer path lengths, which leads to drastic drops in signal strength and makes it more vulnerable to detection noises. To compensate for this, choosing a ROI position closer to the vessel surface within larger vessels (rather than at the boom of the vessel) is a good strategy for more robust inverse calculation at the cost of less absorption contrast.

The presented numerical investigation does not include other possible confounding factors presented in human eye, such as RPE melanin concentration. Fortunately, as OCT images are depth-resolved, the signal from these deeper layers is unlikely to interfere with the signal from the more superficial retinal circulation. However, if one want to retrieve blood oxygenation from within the chordal circulation, then such influence cannot be neglected. A more thorough study is required to address the question.

The NIR wavelength band simulated is slightly shorter than the ones currently being used in commercial NIR OCT systems. It is intended so as to include the isosbestic point at around 822 nm for the highest possible absorption contrast within the range. Thus, longer wavelength ranges are even less likely to provide good spectral contrast for inverse sO_2 calculation, and have even lower absorption coefficients.

2.3 Comparing anatomical and functional imaging capability between visible-light and NIR OCT using a dual-band system

The numerical simulation presented in section 2.2 suggests that visible range is advantageous over NIR range in OCT oximetry applications. However, it is still desirable to compare the performance of OCT images in these two bands in real experimental setting. In addition, there are several concerns left unaddressed in the simulation. First, it is not clear how the quality of vis-OCT image compares with NIR ones, both anatomical-wise and functional-wise. Second, due to the drastic difference in tissue optical absorption and scattering, vis- and NIR- OCT images may possess difference contrast. Thus it is worthwhile to investigate the diagnostic value afforded by the novel vis-OCT image.

In this section, a visible-light and NIR dual-band OCT system is designed and constructed. It can acquire both vis- and NIR-OCT images over the same field of view (FOV) simultaneously. Discrepancies, including imaging resolution and key anatomical features, between Vis- and NIR-OCT images are identified. Functional parameters such as retinal circulation sO_2 and blood flow are extracted from both wavelength range and compared with each other.

2.3.1 Material and Methods

2.3.1.1 System setup

Figure 2.8 shows the schematic diagram of the visible-light and NIR dual-band OCT system. A single supercontinuum source (SuperK EXTREME, NKT photonics) provides ultra-wide-band illumination. A pair of beam splitters (DM1 and DM2, SuperK SPLIT, NKT photonics) selectively

separated the output light into visible (500 – 650 nm) and NIR (780 – 950 nm) bands. The separated beams are then individually delivered to the input arms of two Michelson interferometers. The Vis-OCT interferometer adopts a free-space configuration using a 50:50 polarization-insensitive beam splitter (BS013, Thorlabs). The NIR-OCT interferometer consists of a conventional 2×2 optical fiber coupler (TW850R5A2, Thorlabs) with even split ratio.

The sampling beams of the Vis- and NIR-OCT subsystems are recombined by a third dichroic mirror (DM3, FF750-SDi02, Semrock) and share an identical optical delivery path thereafter for retinal imaging. A pair of galvanometer mirrors (QS-7, Nutfiled Technology) steer the illumination beam and project the raster scanning pattern onto the mouse retina through a 5:1 Keplerian telescope (Focal length 75 mm : 15 mm). The collimating lens (CL, Effective focal length 11 mm, Thorlabs) in the NIR path can be adjusted axially to compensate for chromatic aberration between the two wavelength bands to ensure optimal focus is achieved for both visible- and NIR subsystem. Each sub-system has its own reference arm, within which the dispersion mismatch and intensity are carefully balanced for optimal imaging quality.

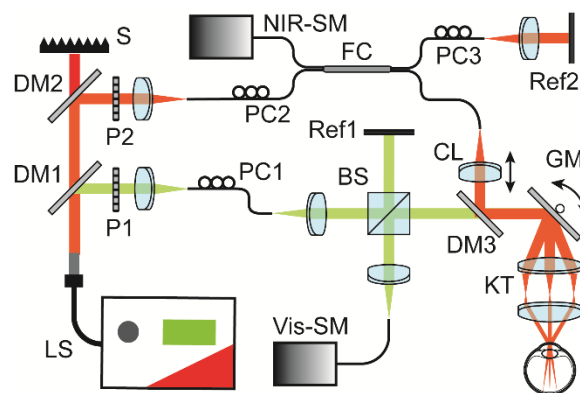


Figure 2.8 Schematic diagram for the visible-light and NIR dual-band OCT system. BS: beam splitter; CL: collimating lens; DM 1-3: dichroic mirror; FC: 2×2 fiber coupler; GM: galvanometer scan mirrors; KT: Keplerian telescope; LS: supercontinuum laser source; P: polarizer; PC: polarization controller; Ref 1-2: reference arm; S: beam stopper; SM: spectrometer.

Two home-made spectrometers digitized the interference spectra. After calibration, the Vis-OCT spectrometer covers the spectral range from 513 nm to 620 nm. The full width at half maximum (FWHM) bandwidth is 91 nm. The NIR-OCT spectrometer covers the spectral range from 773 nm to 909 nm with FWHM bandwidth of 93 nm.

2.3.1.2 Performance characterization

To characterize the system sensitivity and actual imaging resolution, a silver mirror is placed in the sample arm where the mouse eye would otherwise be located. The reflection from the silver mirror corresponds to axial delta function and can be used to measure the system axial impulse response. In addition to the silver mirror, a neutral density (ND) filter (Optical density = 3.0, Thorlabs) is also inserted to attenuate the light so that the detected signal falls within the dynamic range of the spectrometer.

The location of the reference mirror is adjusted axially to create a series of OCT interference fringes pattern with different time delay. This operation is analogous to imaging the sample at various depths. Inasmuch, the depth-dependent sensitivity roll-off can be characterized.

2.3.1.3 Animal preparation

Wild-type C57BL/6 mice are imaged to compare the performance of vis- and NIR OCT image *in vivo*. Key benchmarked metrics include actual image resolution, anatomic features, and functional blood flow and sO₂ measurements. The mouse is anesthetized via intraperitoneal injection (IP) of Ketamine/Xylazine cocktail solution. The dosage is 87 mg Ketamine and 13 mg Xylazine per kilogram of body weight.

Once the mouse enters the desired anesthesia plane, 1% Tropicamide ophthalmic solution is applied for pupil dilation. The mouse is then transferred to a home-made stage and carefully immobilized for imaging. In the interval of acquisition, artificial tear drops are applied every other minute to prevent eye dehydration. The mouse is allowed to fully recover and sent back to animal housing facility after the experiment.

2.3.1.4 Imaging protocols

Vis- and NIR-OCT images are simultaneously acquired in the same volumetric scan. Depending on the specific aim of each acquisition, one of the following two scanning protocols is used. OCT anatomical imaging and oximetry both use the raster scanning protocol. It covers a square FOV of 0.8 mm by 0.8 mm on the mouse retina.

Doppler OCT flowmetry uses “dual-ring” scanning trajectory centered at optic nerve head (ONH). The adoption of the dual-ring protocol allows rapid extraction of both Doppler phase shift ($\Delta\phi$) and Doppler angle (θ_d) from a single exposure [73]. The diameters of the inner and outer rings are 0.52 mm 0.63 mm, respectively.

2.3.1.5 Image reconstruction, OCT oximetry and OCT flowmetry

Structural OCT images are reconstructed following previously established protocols for both visible-light and NIR OCT images. OCT fundus images are generated by projecting mean pixel intensity across the entire retina thickness towards the *en face* plane. The regions containing blood vessels are manually identified and segmented. Then, spectroscopic OCT analysis is performed to retrieve the back-scattered spectrum for OCT oximetry. The steps for retrieving sO_2 are documented in published literatures in great detail [35]. Briefly, a window-based approach is

adopted. A series of short-time Fourier transforms (STFT), which split the entire spectrum into equally spaced narrow bands in k -space, are performed to reconstruct wavelength-dependent OCT amplitude image. The mean OCT intensity within center of the vessel is calculated and assigned as the back-scattered spectra for each identified vessel. The back-scattered spectrum is fitted against the same modified Beer-Lambert's law to model as in reference [35], where a linear relationship between the measured OCT amplitude and relative HbO_2/HbR concentration was established.

OCT flow analysis is performed on the “dual-ring” scanning data set. First, the complex OCT signal is reconstructed from the raw spectrometer interferogram. Then, θ_d and $\Delta\phi$ for each identified vessel are retrieved using methods reported in reference [73]. Briefly, θ_d is obtained by solving geometric relationship from the same vessel in two ring trajectories, assuming the axial length of mouse eye is 3 mm. Meanwhile, calculating the inter-A-line phase difference yield OCT phase image for $\Delta\phi$. When phase-wrapping exists, appropriate un-wrapping algorithm is applied to resolve minor $2\text{-}\pi$ ambiguity before calculating flows [74]. The integral of $\Delta\phi$ within the vessel is translated back to velocity unit, and then inverse projected towards the vessel direction to calculate blood flow rate.

2.3.2 Results

2.3.2.1 System sensitivity and imaging resolution

The respective illumination intensity of the visible and NIR beams are 0.9 mW and 0.8 mW at the pupil plane, measured by a calibrated integrating sphere attached to a miniature spectrometer (USB2000, Ocean Optics). The reconstructed OCT amplitude signal from the mirror surface is

plotted in Fig. 2.9 against increasing imaging depth for both the visible (a) and NIR (b) subsystem. In either plot, the first peak is the highest and sharpest. The height of peaks decreases as depth increases, which is caused by sensitivity roll-off from limited spectral resolution. Meanwhile, the width of the peaks also increases slightly at deeper locations due to residue dispersion mismatch.

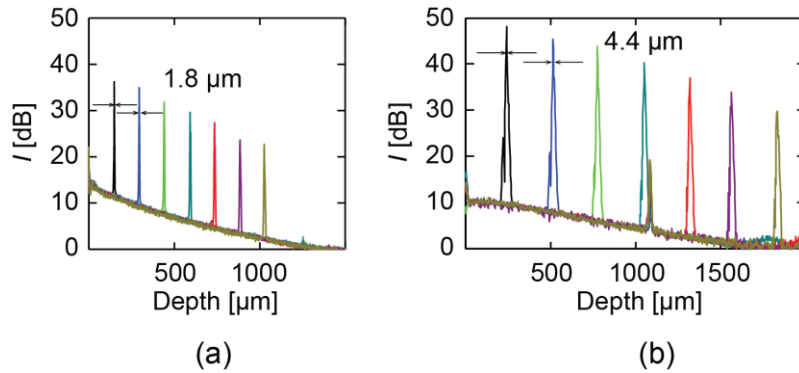


Figure 2.9 OCT detection sensitivity and axial imaging resolution. (a) OCT axial impulse response from mirror surface acquired using vis-OCT subsystem. (b) OCT axial impulse response from mirror surface acquired using NIR-OCT subsystem. The first peak is used as benchmarks for both sensitivity and resolution measurements.

For both the visible and NIR subsystem, the first peaks are used as the benchmark to characterize sensitivity and axial resolution. This approach agrees with the common practice where the imaged sample is often placed close to the zero-delay line. In Fig. 2.9(a), the height of the first peak with respect to the noise floor is 26.6 dB. Thus, the imaging sensitivity of the vis-OCT subsystem is 86.6 dB after taking into consideration of the 60-dB round-trip attenuation from the inserted ND filter. The FWHM (-6 dB) width of the peak is 1.8 μm , characterizing the axial imaging resolution of the vis-OCT subsystem in air. Similarly, the sensitivity of the NIR-OCT subsystem is 98.2 dB, and it has 4.4 μm axial resolution in air. Sensitivity roll-off is characterized by linear regression of all the peaks within the imaging depth range. The vis- and NIR-OCT subsystems achieve sensitivity roll-off of 16.4 dB/mm and 12.2 dB/mm, respectively.

2.3.2.2 Comparison of imaged anatomic features between Vis- and NIR-OCT

Figure 2.10 compares anatomical features from the simultaneously acquired visible and NIR OCT fundus images. Both images demonstrate similar features, where retinal blood vessels, neural fiber layer (NFL), and retinal pigment epithelium (RPE) contribute to the majority of the contrast. One slice of B-scan is taken from the same y -location (indicated by the dashed yellow lines) from both the visible and NIR volumetric scan data and shown in Fig. 2.10(c) and (d), respectively. Multiple retinal layers are distinguishable in both images, with NFL and RPE the brightest. The distinguishable and identified layers are annotated in both B-scans.

Besides similarities, visible and NIR OCT images also demonstrate considerable difference in image contrast. A strip pattern, which originates from the axons of retinal ganglion cells in NFL, is more recognizable in the Vis-OCT fundus image. Two key factors can contribute to this phenomenon. First, NIR-OCT has larger imaging depth compared to vis-OCT. As NIR light penetrates deeper into the tissue, the more intense, homogenous signals from the RPE and choroid overshadows features from NFL in the projected fundus image, giving it a more uniform look. Second, visible light experiences stronger back-scattering from NFL with respect to surrounding tissues, possibly due to its shorter wavelength. Specifically, one can measure the relative intensity ratio between the NFL layer and its surrounding tissues, which is 3.2:1 and 2.0:1 in the visible and NIR B-scans, respectively.

The visible wavelength range also demonstrated superior axial resolution over NIR. In the vis-OCT B-scan, RPE and choroidal layers can be clearly distinguished. In contrast, these layers merge together in NIR-OCT B-scan as one single highly reflective interface. The extracted A-line profiles

from the indicated location showed narrower peak profile, which corresponds to retinal layer interfaces.

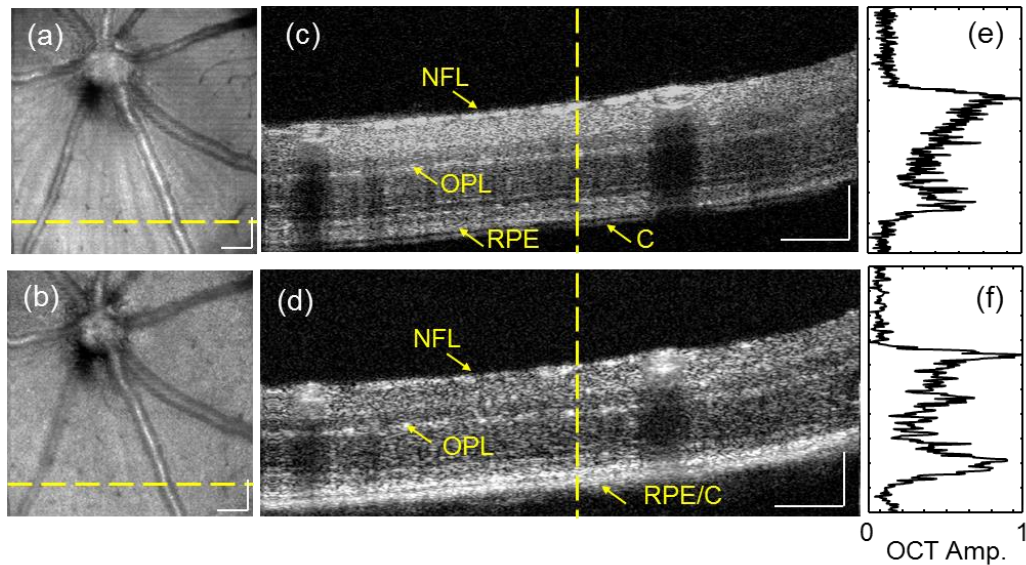


Figure 2.10 Comparison of structural visible and NIR OCT images. (a) & (b) *En face* view of OCT structure image for vis- and NIR-OCT, respectively. (c) & (d) are B-scan image taken from the location indicated by the yellow dashed line in (a) and (b), respectively. C: Choroid; NFL: neural fiber layer; OPL: outer plexiform layer; RPE: retinal pigment epithelium. (e) & (f) show the A-line profiles taken from yellow dashed line in (e) and (f), respectively. Scale bar: 100 μm .

In addition, visible and NIR OCT images demonstrate drastically different quality of speckle patterns. Specifically, speckle in the Vis-OCT B-scan is densely packed and scattered. In contrast, NIR-OCT speckle appears to be larger and clumped. The difference can be explained by the longer coherence length of the NIR illumination light and the fact that the NIR subsystem has lower imaging resolution than the visible subsystem [44].

2.3.2.3 Comparison of oximetry capability between Vis- and NIR-OCT

Spectroscopic OCT analysis is attempted on both visible and NIR OCT data sets to retrieve sO_2 within the retinal circulation. Figure 2.11 compares the back-scattered spectra obtained using visible-light and NIR OCT, respectively. Each plot consists of one artery and one vein. The arterial and venous OCT back-scattering spectra show two clear crossings in the visible range. This guaranteed the convergence and stability of the least-squares fitting algorithm. In contrast, the two corresponding spectra from NIR-OCT dataset show little difference in their spectral distributions (Fig. 4(b)). Even though theoretically there exists one isosbestic point at around 822 nm in the oxygenated/deoxygenated whole blood absorption spectrum [66], such a feature was not identifiable in NIR-OCT measurements. One important confounding factor is that blood scattering is more than 100 times stronger than absorption in the NIR range, but has less usable differentiating contrast [66]. As a single scaling factor can almost convert one spectrum to another, a mathematical interpretation that correlates such spectral changes with sO_2 is much more difficult. In this case, our least-squares regression failed to converge and we did not obtain reliable sO_2 estimations, which agreed with our numerical simulation studies [75].

In summary, only OCT with a visible range light source is able to yield stable sO_2 measurements, which agrees with the findings presented in section 2.2.2.2. The corresponding sO_2 values for each identified branch retinal arteries and veins are plotted in Fig. 2.12 to demonstrate the capability of vis-OCT oximetry.

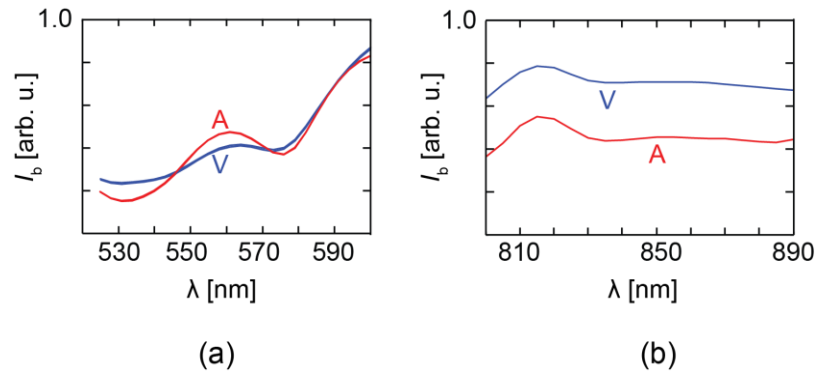


Figure 2.11 Wavelength-dependent OCT back-scattered intensity from a identified artery (A) and vein (V). (a) Spectra obtained using vis-OCT subsystem. (b) Spectra obtained using NIR-OCT subsystem.

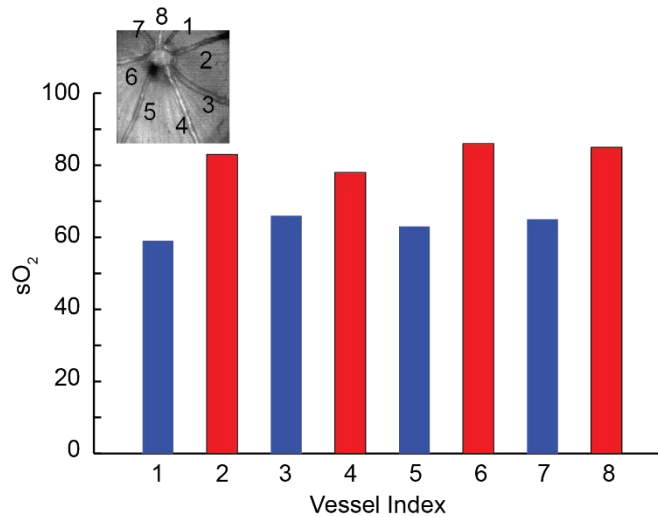


Figure 2.12 OCT oximetry on major retinal circulation vessels. sO_2 values are obtained using vis-OCT data sets.

2.3.2.4 Comparison of flowmetry capability between Vis- and NIR-OCT

Figure 2.13 shows the B-scan anatomical images overlaid with $\Delta\phi$ within blood vessels along the trajectory of the smaller ring scan for vis-OCT (a) and NIR-OCT (b), respectively. In both Doppler OCT B-scans, the direction of blood flow shows alternating pattern between adjacent vessels, reflecting the anatomical arrangement of arteries and veins within the retinal circulation. In vessels number 6, 8, 9 and 10 (numbered from left to right), phase-wrapping can be observed due to higher blood flow rate or smaller Doppler angle. Phase-wrapping is more pronounced in vis-OCT Doppler image Fig. 2.13(a), possibility because a shorter wavelength range of the light spectrum used, which is more susceptible to the $2\text{-}\pi$ ambiguity.

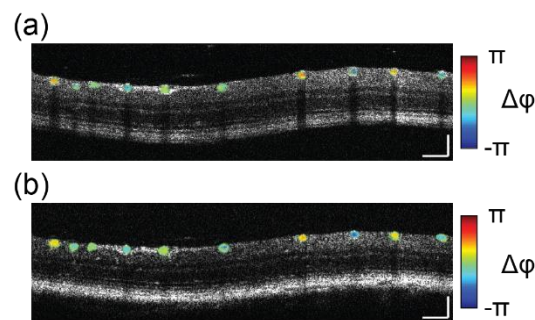


Figure 2.13 Doppler OCT phase image from the dual-ring scan protocol. (a) Vis-OCT data set. (b) NIR-OCT data set. Scale bar: 100 μm .

The flow rate for each identified major retinal blood vessel is retrieved as the mean value from the eight consecutive pairs of ring scans. Figure 2.14 compares the results obtained using visible and NIR data set, respectively. None of the ten vessels showed significant flow rate difference between the two illumination bands.

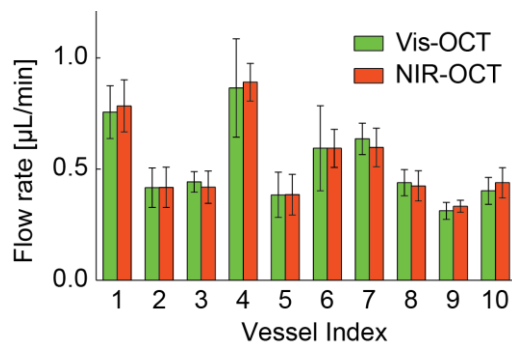


Figure 2.14 Comparison of absolute blood flow measurements using both vis- and NIR-OCT. The vessels are indexed from left to right in Fig. 2.12. Errorbar is S.D.

In addition, the total perfusion rate is calculated as the sum of flow in either arteries or veins. For vis-OCT, the total perfusion rate is 2.71 ± 0.27 $\mu\text{L}/\text{min}$ for arteries and 2.53 ± 0.27 $\mu\text{L}/\text{min}$ for veins. Similar values of 2.76 ± 0.17 $\mu\text{L}/\text{min}$ (artery) and 2.52 ± 0.17 $\mu\text{L}/\text{min}$ (vein) are obtained by NIR-OCT. No statistically significant difference is found between total blood flow of arteries and veins, or between vis- and NIR-OCT measurements. The consistency of these values indicates that the measurement is reliable and that both visible and NIR illumination have comparable performance in OCT oximetry.

2.2.3 Discussion

Both visible-light and NIR wavelength range can be used to acquire fundus OCT images *in vivo*. The presented experimental data prove that both vis- and NIR-OCT images reveal reasonably identical anatomical structures found in mouse retina. In vis-OCT images, higher axial resolution, afforded by its shorter wavelength range, allows differentiation of the RPE-Choroid complex. Such a feature has the potential to facilitate RPE pathognomonic evaluation [76]. Vis-OCT images also tends to emphasis contrasts generated within NFL, which might give vis-OCT a unique advantage

when changes in NFL thickness and reflectivity are of clinical significance, such as in the diagnosis of glaucoma [77].

Aside from its superior axial resolution, the lateral resolution of vis-OCT should also be an improvement over NIR-OCT. Specifically, if one assumes that the mouse eye has an effective numerical aperture (NA) of ~ 0.05 , the theoretical value for lateral resolution would be $7.1 \mu\text{m}$ and $10.5 \mu\text{m}$ for vis- and NIR-OCT, respectively. Unfortunately, such an improvement is not obvious in the mouse fundus image, possibly due to the poor optical quality of rodent eye [78].

The experimental results agree with the previous conclusion obtained by the numerical Monte Carlo investigation that visible-light is more suitable for OCT oximetry applications. Only vis-OCT is able to inversely calculate retinal circulation $s\text{O}_2$ following spectroscopic OCT analysis on fundus volumetric scan acquired *in vivo*. In contrast, blood absorption contrast is interfered by tissue scattering and provides little usable information. It is extremely difficult to extract stable $s\text{O}_2$ estimation in the NIR wavelength band unless more advanced data-fitting algorithms are developed.

One weakness of vis-OCT is its limited penetration depth. Due to stronger tissue absorption and scattering in the visible spectral range, visible light energy dissipates faster than NIR. Though both subsystems have adequate penetration depth to image the entire neural retina in the current application, NIR-OCT performs much better if the target-of-interest lies beneath RPE.

Though both subsystems are able to offer reliable blood flow measurements, vis-OCT is more vulnerable to 2π ambiguity and phase-wrapping due to its shorter wavelength range. Thus NIR-OCT is the preferred choice for flow measurement applications when higher flow rate is expected.

2.4 Summary

In this chapter, the effect of illumination wavelength band is investigated for two common choices, visible-light centered around 560 nm and NIR centered around 850 nm. For ophthalmological applications, they both reveal detailed fundus anatomical features, demonstrating invaluable diagnostic value. In addition, it is shown that both wavelength bands are capable of being used in functional OCT imaging, i.e. Doppler OCT flowmetry.

However, only vis-OCT is able to provide accurate and stable blood sO_2 measurements following both numerical and experimental investigations. The accuracy of vis-OCT oximetry is subsequently tested and verified. With functional OCT oximetry being the key aspect of this dissertation, the work presented in this chapter serve as the foundation of later studies.

Vis-OCT also provides higher axial resolution compared to its NIR counterpart. This may be advantageous when subtle changes in retina layers is of diagnostic value. Meanwhile, NIR-OCT has deeper penetration depth and is more tolerating to phase-wrapping in OCT flowmetry application.

In summary, both vis- and NIR-OCT are versatile imaging modalities. They complement, rather than compete, each other to provide a wide array of assessment on the anatomy and functionality of the retina. The wavelength bands of choice should be based on the specific requirements of the application. A dual-band OCT system similar to the one developed can provide a compact solution and offer a broader range of information than either band alone.

CHAPTER 3

Label-free retinal angiography and angiograph-based oximetry

This chapter addresses the challenge of resolving retinal microvasculature using intrinsic optical coherence tomography (OCT) angiographic contrast. A new theoretical formulation for visible light OCT (vis-OCT) angiography-based oximetry is also presented. The established theory is verified by *in vitro* experiments using polystyrene capillary tube. After appropriate normalization and calibration, robust *in vivo* measurements of absolute blood oxygen saturation (sO_2) variation in the retinal circulation and relative sO_2 variation in the choriocapillaris following inhalation oxygen challenge are demonstrated for the first time. The new method requires much reduced illumination power, which can greatly benefit clinical applications of vis-OCT.

3.1 Introduction

Functional assessment of hemodynamic response has emerged as an invaluable supplement to anatomical optical coherence tomographic (OCT) imaging. One major application of functional OCT relies on blood flow, or moving blood cells, to generate intrinsic velocity-based contrast. Reported laboratory and clinical research projects include retinal blood flow measurements [79-

85], and label-free retinal OCT microangiography (OMAG) [86-88]. Because the neuroretina has high metabolic demand, variations in the retinal circulation can be an excellent indicator of the viability of the retina and has been associated to various retinal diseases [89-91].

Another important hemodynamic parameter within the retinal circulation is the hemoglobin oxygenation saturation (sO_2). sO_2 characterizes the utilization of oxygen-carrying capability of blood. The sO_2 difference between the branch retinal arteries and veins quantifies oxygen extraction from the retinal circulation. When combined with blood flow measurements, retina oxygen metabolic rate ($rMRO_2$) can be obtained [92, 93]. Label-free determination of sO_2 using optical approach is possible because oxyhemoglobin (HbO_2) and deoxyhemoglobin (HbR) have distinctively different absorption properties in the visible to near-infrared (NIR) spectral range. Early attempts on OCT oximetry date back more than a decade ago, where near infrared (NIR) illumination was employed focusing on the HbO_2 and HbR isosbestic point around 800 nm [30-33]. Unfortunately, the relatively low optical absorption is often shadowed by tissue scattering in the NIR region, and no results was obtained *in vivo*. Details on this matter are thoroughly discussed in chapter 2.

Later, knowing that HbO_2 and HbR have much higher absorbing contrast within the visible-light spectral range, two groups, Yi *et. al.* and Robles *et. al.*, independently explored the feasibility of using visible light OCT (vis-OCT) to quantify sO_2 from *ex vivo* and *in vitro* samples, respectively [94, 95]. They further showed measurement of blood oxygenation using spatially-resolved spectroscopic analysis from systemic circulation *in vivo* [34], and the first demonstration of vis-OCT retinal oximetry in rodents *in vivo* [35].

The reported vis-OCT oximetry approach requires that the target blood vessel must first be visualized. Image segmentation is then applied to isolate the blood vessel and retrieve spectroscopic OCT intensity from within the vessel. However, this requirement poses certain challenges in studying blood circulation systems in the eye. First, smaller blood vessels, including arteriole, venules, and choroidal capillaries, are generally not visible in conventional OCT structure images. Thus, it is impossible to retrieve sO_2 from these unresolved vessel. Second, the segmentation algorithm to identify and isolate blood vessels can be cumbersome and time-consuming. It may become extremely difficult or even impossible when image signal-to-noise ratio (SNR) is low.

In response to these challenges, Yi *et al* later proposed to combine blood dynamic motion contrast and spectroscopic absorption contrast simultaneously for microvasculature sO_2 calculation [96]. This approach separates OCT back-scattered signal from blood and other static tissues, enhancing the contrast from otherwise non-resolvable vessels while eliminating the need for cumbersome image segmentation previously needed to locate blood vessels. A similar strategy was recently adapted for both exposed cortical imaging and retinal imaging in rodents [97].

However, the theoretical foundation for OCT angiography-based oximetry is yet to be established. Specifically, the complication of blood flow to the angiographic signal is not explicitly considered in all aforementioned studies, which could confound sO_2 calculations *in vivo*.

The work presented in this chapter seeks to address this concern. First, the theoretical formulation is expanded to cover OCT angiography-based oximetry by taking account of dynamic blood flow contrast. A new data processing algorithm, i.e., using spectral derivative to normalize flow rate, is investigated for robust sO_2 calculation. The theoretical model is subsequently verified

using a phantom capillary tube filled with anticoagulated bovine whole blood. Finally, the developed vis-OCT angiography-based oximetry is used to detect sO₂ variations upon inhaling different gas mixtures in rat retina *in vivo*. Moreover, non-invasive measurements of the relative sO₂ changes are demonstrated for the first time using vis-OCT.

3.2 Theoretical formulation of OCT angiography-based oximetry

In this section, the extended theoretical formulation for the spectroscopic analysis on vis-OCT angiography-based oximetry is presented. The motion-enhanced dynamic scattering model is to demonstrate that a linear relationship can be established between sO₂ and OCT angiographic spectrum. Without loss of generality, one can start the formulation from a wavelength-dependent A-line signal from OCT angiogram $AA(z, \lambda)$, where z defines the axial coordinate and λ denotes the wavelength. Note that the formulation omits the finite axial resolution and sensitivity roll-off for simplicity purpose. At a given point along the angiographic A-line,

$$AA(z, \lambda) = I_0(\lambda)r(z, \lambda)\eta(z, \lambda)G(\Delta\varphi), \quad (3.1)$$

where $I_0(\lambda)$ is incidence intensity. $r(\lambda)$ is the wavelength-dependent back scattering coefficient of local tissue, which can be further expressed by a power law $r(\lambda) = B\lambda^{-\alpha}$ under the first Born approximation. B is a scaling constant while the value of α depends on the tissue type and has been previously characterized to be ~ 1 with variations around ± 0.2 [69, 98]. The term $G(\Delta\varphi)$ is a non-negative scalar representing the dynamic contrast enhancement caused by random phase variation due to motion. The value of G is assumed to be 0 only if the tissue is static. $\eta(z, \lambda)$ is the cumulative attenuation when light double passes the tissue,

$$\eta(z, \lambda) = e^{-\int_0^z 2\mu_t(z', \lambda) dz'}, \quad (3.2)$$

where μ_t is the total attenuation coefficient of local tissue attributed to both optical absorption and scattering.

After normalizing $AA(z, \lambda)$ by the source spectrum $I_0(\lambda)$, the resulting image is analogous to the wavelength-dependent optical density (OD) mapping used in traditional fundus retinal oximetry, except for the additional motion enhancement term $G(\Delta\varphi)$. Hence the notation $OD(z, \lambda)$ is used to denote the normalized $AA(z, \lambda)$,

$$OD(z, \lambda) = \ln \frac{AA(z, \lambda)}{I_0(\lambda)} = \ln r(\lambda) + \ln \eta(\mu_a, \mu_s, \lambda) + \ln G(\Delta\varphi). \quad (3.3)$$

Plugging Eq. 3.2 into Eq. 3.3 and rearranging lead to,

$$OD(z, \lambda) = \alpha\lambda + \ln B - 2\int_0^z \mu_t(z', \lambda) dz' + \ln G(\Delta\varphi). \quad (3.4)$$

One can further take the partial derivative of OD against wavelength (spectral derivative) on both side of the equation, which leads to the expression,

$$\frac{\partial OD(z, \lambda)}{\partial \lambda} = -\frac{2\partial \int_0^z \mu_t(z', \lambda) dz'}{\partial \lambda} + \alpha + \frac{\partial \ln G(\Delta\varphi)}{\partial \lambda}. \quad (3.5)$$

In the OCT angiography imaging protocol, wavelength is much smaller than the motion displacement of the blood cells. For example, red blood cells travel an average of 0.13 mm during the 0.01 s dwell time between acquisitions. Thus the phase variation becomes random and the enhancement factor $G(\Delta\varphi)$ loses wavelength dependence. The spectral derivative of $G(\Delta\varphi)$ could be considered approximately zero and the equation becomes

$$\frac{\partial OD(z, \lambda)}{\lambda} = -\frac{2\partial \int_0^z \mu_t(z', \lambda) dz'}{\partial \lambda} + \alpha. \quad (3.6)$$

Now let us consider the attenuation contribution from the whole blood and the static tissues.

As light propagates in tissue, the cumulative attenuation is

$$\int_0^z \mu_t(z', \lambda) dz' = \int_0^{l_b} \mu_t(z', \lambda) dz'_{blood} + \int_0^{l_{else}} \mu_t(z', \lambda) dz'_{static\ tissue}, \quad (3.7)$$

or, after simplification,

$$\int_0^z \mu_t(z', \lambda) dz' = \mu_{t_b} l_b + \overline{\mu_{t_{else}}} l_{else}, \quad (3.8)$$

where μ_{t_b} and $\overline{\mu_{t_{else}}}$ denote the total attenuation coefficients of whole blood and averaged attenuation coefficient of static retinal tissue, respectively; l_b and l_{else} denote the cumulative optical path length within the blood vessel and in other retinal tissues, respectively.

It is previously characterized that the total attenuation coefficients of non-blood retinal tissues have little wavelength-dependency compared with that of blood [60, 66]. Thus, the spectral derivative in Eq. 3.6 can be approximated by,

$$\frac{\partial \int_0^z \mu_t(z', \lambda) dz'}{\partial \lambda} = \frac{\partial \mu_{t_b}}{\partial \lambda} l_b + \frac{\partial \overline{\mu_{t_{else}}}}{\partial \lambda} l_{else} \cong \frac{\partial \mu_{t_b}}{\partial \lambda} l_b. \quad (3.9)$$

One can further express μ_{t_b} with respect to sO_2 as

$$\mu_{t_b} = sO_2 \cdot \mu_{t_{Oxy}} + (1 - sO_2) \cdot \mu_{t_{Deoxy}}, \quad (3.10)$$

where $\mu_{t_{Oxy}}$ and $\mu_{t_{Deoxy}}$ are the total attenuation coefficients for fully oxygenated and deoxygenated whole blood, respectively. For simplicity, one can define the following two constants, $k_{Oxy} = \frac{\partial \mu_{t_{Oxy}}}{\partial \lambda}$ and $k_{Deoxy} = \frac{\partial \mu_{t_{Deoxy}}}{\partial \lambda}$ and plug Eq. 3.8 – Eq. 3.10 into Eq. 3.6 so that

$$\frac{\partial OD(z, \lambda)}{\partial \lambda} = -sO_2 \cdot (k_{Oxy} - k_{Deoxy}) l_b + k_{Deoxy} l_b + \alpha. \quad (3.11)$$

It is clear that Eq. 3.11 establishes a linear relationship between the spectral derivative of the OD function and sO_2 , while $(k_{Oxy} - k_{Deoxy})l_b$ serves as a constant scaling factor. l_b is a constant determined by the choice of ROI. Its exact value can be estimated by measuring the mean optical path on the OCT angiograph. However, in the presented study, its value, together with the value of α , are implicitly determined through calibration.

3.3 Material and Methods

3.3.1 Scanning protocol for vis-OCT angiography

The vis-OCT angiography adopts a uni-directional raster-scanning protocol. Throughout the chapter, the fast-scan direction is denoted as the x axis, and slow-scan direction the y axis. Each B-scan consists of 400 A-lines parallel to the x axis. The sampling rate is 50 kHz per A-line. Immediately after the finish of each B-scan, the laser spot is returned to the x axis origin without acquiring any data at four times the forward speed. A new B-scan is started immediately thereafter. Thus, the inter-frame dwell time is exactly 10 millisecond. Each y location is repeated five times before moving to the next one. The entire vis-OCT angiographic volumetric scan consists of 512 y locations, or a total of $400 \times 5 \times 512 = 1024000$ A-lines. It takes 25.6 seconds to acquire the whole angiographic vis-OCT data set.

3.3.2 Phantom experiment preparation

A polystyrene capillary phantom is fabricated to verify the OCT angiography-based oximetry using spectral derivative is not affected by varying flow velocity. The inner diameter of the tube is 125 μm , which is comparable to vessels found in human retinal circulation. The tube is then filled with anticoagulated bovine whole blood (Quad Five). The blood is fully oxygenated by exposing it to normal air at room temperature for 1 hour prior to the experiment. To mimic other scattering retinal tissues surrounding the blood vessel, the phantom is embedded beneath 2.5 % agarose gel mixed with 0.5% Intralipid.

The blood perfusion rate is controlled using a syringe pump (PHD 2000 Infusion, Harvard Apparatus). Various flow rates within the physiological range from 0.0 mL/min to 0.05 mL/min are tested to investigate their effects on retrieving sO_2 .

3.3.3 Animal preparation

All experiment procedures are approved by the Northwestern University IACUC and conformed to the Association for Research in Vision and Ophthalmology Statement on Animal Research.

Wild-type Long Evans rats are anesthetized using Ketamine/Xylazine cocktail solution (11.45 mg Ketamine and 1.71 mg Xylazine per milliliter of solution, respectively) via intraperitoneal injection (IP). The initial dose contains 87 mg Ketamine and 13 mg Xylazine per kilogram of body weight. A supplementary dose (30% of the original volume) is administered after 30 minutes of the initial injection to maintain deep anesthesia. Prior to imaging, 0.5% Tetracaine hydrochloride

ophthalmic solution and 1% Tropicamide ophthalmic solution are applied for local eye anesthesia and pupil dilation.

The rat is subsequently transferred to a custom-made stage for imaging. During the entire procedure, its core body temperature is maintained at 37 °C using an electronic heating pad with feedback control (FHC Inc).

Normal air (21% O₂, 79% N₂) at 4.2 Standard Liter per Minute (SLPM) is supplied to the rat when a baseline OCT image is taken. Then, the rat is ventilated the following gas mixtures in the order of: (1) 5% carbon dioxide (21% O₂, 74% N₂, and 5% CO₂); (2) pure oxygen (100% O₂); and (3) 10% oxygen (10% O₂ and 90% N₂). Normal air is supplied for at least 3 minutes whenever there is a change in gas compound. After switching, the rat is allowed to stabilize for at least 3 minutes before OCT imaging. A pulse oximeter attached to the rear limb of the animal provided real-time monitoring of its heart rate and systemic arterial oxygen saturation. If either one shows significant variation (>2% over 10 seconds), the rat is allowed more time to stabilize.

One final acquisition is taken after the sequence with normal air ventilation. For each OCT measurement, the corresponding oximeter readings are also recorded simultaneously.

3.3.4 Vis-OCT imaging of retinal microvasculature

3.3.4.1 OCT angiography

OCT angiographic contrast originates from flowing blood cells as they introduce random phase and amplitude fluctuations to the back-scattered light. It is analogous to laser speckle imaging [99], but additionally offers depth-resolved volumetric imaging of vascular structure.

In OCT angiography, the dynamically back-scattered OCT signal from blood can be separated from static tissue signals through high-pass filtering. Phase-sensitive complex-decorrelation algorithm, i.e. calculating the complex valued difference between adjacent B-scans, is usually used to generate OCT angiographic contrast [87, 96, 100]. Unfortunately, bulk tissue motion, caused by normal physiological processes such as heart beating and breathing and rotating scanning mirrors, is inevitable and interferes with the algorithm. Care must be taken to cancel these effects so only dynamic contrast from within the blood contributes to the final OCT angiograph. Due to the relatively short inter-frame dwell time (10 ms), motion artifacts other than non-rotational rigid translation are neglected.

A two-step approach is therefore adopted to correct bulk-tissue motion between adjacent B-scans at the same y location. Without loss of generality, the notation $A(x, z, t)$ is used to represent the complex vis-OCT B-scan stack from the same y location, where x and z represent the lateral and axial coordinate, respectively; t is the index of the B-scan in time order, whose value ranges from 1 to 5 in this case. The first step is to co-register the five real-valued OCT structure image using rigid translation, so that motion artifacts greater than the imaging resolution are corrected. The cross-correlation function between the two adjacent B-scan images ($t+1$ and t) is calculated and its peak position indicates the amount of movement. The later image is then shifted back so the two images were properly registered.

The second step is to correct the phase of the complex B-scan stack, so that residual bulk motion smaller than imaging resolution is also accounted for [101]. Two global phase modulators, the axial global phase fluctuations (AGPF) modulator and lateral global phase fluctuations (LGPF)

modulator, are applied consecutively on the co-registered OCT B-scan stacks. The AGPF can be estimated by integrating the phase variation along the A-line axial direction (z axis) as

$$AGFP(x) = -arg[\int A^*(x, z, t_2)A(x, z, t_1)dz], \quad (3.12)$$

while the LGPF can be estimated by integrating the phase variation along the x axis as

$$LGFP(z) = -arg[\int A^*(x, z, t_2)A(x, z, t_1)dx]. \quad (3.13)$$

The AGFP and LGFP modulators are then z - or x - extended and multiplied to the corresponding B-scans pixel by pixel. The resulting bulk-motion-corrected complex B-scan stack is denoted $A'(x, z, t)$. Thus, one can calculate the complex-differential among B-scan stack to generate the angiographic B-scan, $AG(x, z, t)$, at each y location,

$$AG(x, z) = \mathbb{E}|A'(x, z, t_{\tau+1}) - A'(x, z, t_{\tau})|, \quad (3.14)$$

where \mathbb{E} represents the expected value; and $|\cdot|$ represents the modulus operation. The process is iterated for each y location to obtain the volumetric angiographic stack, $AG(x, y, z)$.

Finally, *en face* angiogram of the fundus is generated by integrating the first 15 pixels of the highest motion contrast along z direction.

3.3.4.2 Retrieving sO₂ from vis-OCT angiogram using spectral derivative

Four Gaussian-shaped STFT windows, each with 10 nm full-width-at-half-maximum (FWHM), are empirically chosen to estimate the spectral derivative of the wavelength-dependent vis-OCT angiogram, $AG(x, y, z, \lambda)$ [86, 87, 96]. The center wavelength of the four spectral windows are 565 nm, 568 nm, 571 nm, and 574 nm, respectively. This spectral range is chosen to be near the HbO₂/HbR isosbestic point to maximize spectral contrast.

The retinal circulation and choroidal circulation are manually separated. The first 15 consecutive pixels with the highest angiographic contrast is integrated and projected along the z axis to generate *en face* fundus angiograph $AG(x, y)$. The integration interval of 15 is empirically chosen and found to yield best signal-to-noise ratio in the projected fundus angiogram. Meanwhile, the angiographic contrast is averaged laterally within each identified vessel to generate angiographic A-line, $AA(z, \lambda)$, which is first described in section 3.2.

Following the theoretical formulation outlined in section 3.2, one first normalizes $AA(z, \lambda)$ using the corresponding source spectrum $I_0(\lambda)$ to calculate the localized $OD(z, \lambda)$. Then, linear regression is used to estimate the partial derivative against wavelength across the four selected center wavelengths.

Finally, this spectral derivative is converted to absolute sO_2 using calibration points provided by pulse oximetry spO_2 readings. During this calibration, it is assumed that major retinal arteries had the same sO_2 as systemic arterial sO_2 . The calibration is performed independently for each animal. After calibration, venous sO_2 can be retrieved using the established calibration function.

Table 3.1 summarizes the procedures to retrieve sO_2 from vis-OCT angiogram.

Table 3.1 Summary of data processing procedures to extract sO₂.

Operations procedure to extract sO ₂ for any given blood vessel	
1	To generate wavelength-dependent OCT angiography using STFT and motion enhanced dynamic scattering contrast according to Eq. 3.14 Input: Raw interference spectrum, STFT window Output: $AG(x, y, z, \lambda)$
2	To choose a region of interest within a vessel from <i>en face</i> OCT fundus image and average the signal over x, y extents Input: $AG(x, y, z, \lambda)$, ROI of a vessel (x, y) Output: $AA(z, \lambda)$
3	To calculate localized optical attenuation function $OD(z, \lambda)$ according to Eq. 3.4 Input: $AA(z, \lambda)$, source spectrum $I_0(\lambda)$ Output: $OD(z, \lambda)$
4	To calculate partial derivative on $OD(z, \lambda)$ against wavelength according to Eq. 3.5 Input: $OD(z, \lambda)$, λ Output: $\frac{\partial OD(z, \lambda)}{\partial \lambda}$ (spectral derivative)
5	To calculate average $\frac{\partial OD(z, \lambda)}{\partial \lambda}$ long the z axis and to calibrate all the major retinal arteries against systemic spO ₂ Input: spO ₂ , $\frac{\partial OD(z, \lambda)}{\partial \lambda}$ Output: calibration function
6	To convert $\frac{\partial OD(\lambda)}{\partial \lambda}$ to sO ₂ according to Eq. 3.11 Input: $\frac{\partial OD(\lambda)}{\partial \lambda}$ of selected vessel, calibration function Output: absolute sO ₂

3.4 Results

3.4.1 Phantom experiment verification

Figure 3.1 compares cross-sectional B-scans between OCT structural images and motion-enhanced angiograms from the fabricated polystyrene tube sample. The flow rate of the blood is changed within normal physiological range from 0.00 mL/min to 0.05 mL/min with 0.01 mL/min step size. OCT structural B-scans (upper row) have strong background signal outside the blood vessel. The background signal originates from the back-scattered photon from Intralipid within surrounding agarose gel. In comparison, this static background is largely suppressed in the angiographic B-scan (lower row). Meanwhile, OCT angiography (OCTA) greatly enhances the contrast from flowing blood using dynamic motion contrast. Even when the flow rate is set to zero, intrinsic random Brownian motion is sufficient to enhance the contrast (the left column).

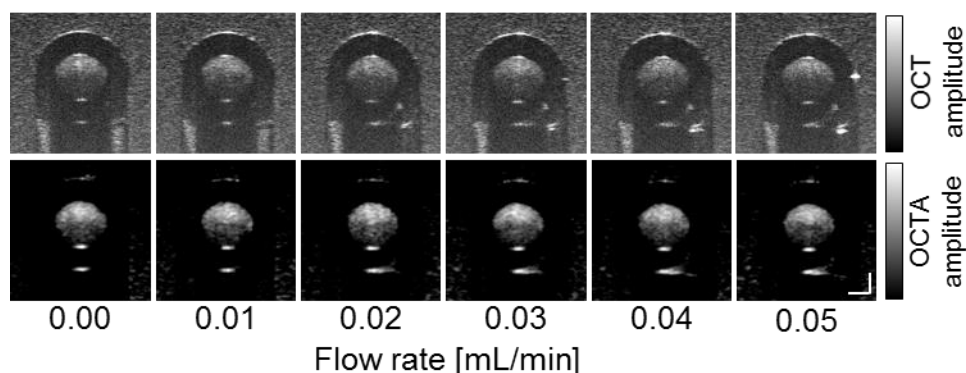


Figure 3.1 Cross-sectional B-scan of the tube using OCT structural (top row) and OCT angiographic (bottom row) contrast. The images are acquired at varying flow speed from 0.00 mL/min to 0.05 mL/min. Scale bar: 50 μm .

The volumetric OCT angiographic contrast is subsequently projected along z -axis to generate the *en face* view of the polystyrene capillary tube, Fig. 3.2(a). Four rectangular region-of-interest

(ROI) of equal size are selected along the longitudinal axis of the tube. These ROI represents where spectroscopic OCTA contrast is retrieved and are indicated by yellow box. Figure 3.2(b) plots the mean and standard deviation (S.D.) of the OCTA spectra obtained from the zero-flow tube. The shape of the averaged spectrum shows similar features to the absorption spectrum of oxygenated whole blood.

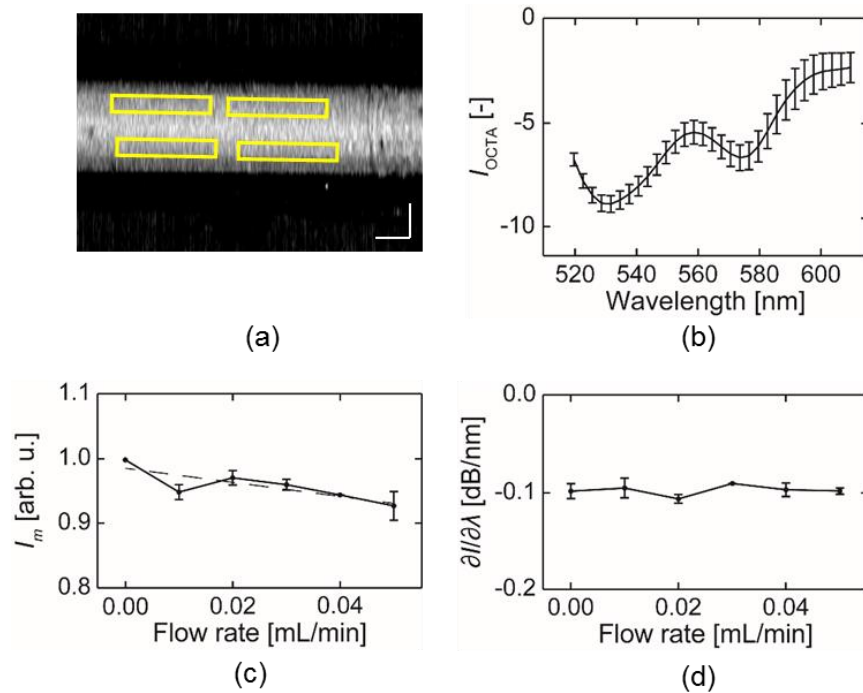


Figure 3.2 (a) *En face* OCT angiography image of the polystyrene capillary tube. The yellow rectangles indicate the places where OCTA spectra are retrieved. Scale bar: 50 μm; (b) OCTA spectrum (I_{OCTA}) retrieved from phantom tube with flow rate = 0.00 mL/min. (c) Averaged intensity I_m from capillary tube at increasing flow rate; (d) The spectral derivative of I_{OCTA} spectrum within 560-580 nm from the capillary tube at increasing flow rates. Error bar = S.D.

Two parameters are subsequently investigated to characterize OCTA spectra for oximetry purpose. The first parameter, the mean OCTA intensity (I_m), is plotted against increasing flow rate in Fig. 3.2(c). A linear regression shows clear negative velocity-dependence of I_m on increasing flow rate ($p < 0.001$). Thus, I_m is not suitable for OCT oximetry applications as it introduces

confounding factor related to flow velocity. On the contrary, the spectral derivative ($\partial I/\partial\lambda$) from 565 nm to 574 nm is almost unaffected by increasing flow rate, as shown in Fig. 3.2(d). The slope of the $\partial I/\partial\lambda$ curve does not deviate from zero ($p = 0.74$). This result verifies that $\partial I/\partial\lambda$ is flow-independent across the investigated physiological range. Thus, sO₂ estimation using $\partial I/\partial\lambda$ should not be affected by different flow rate.

3.4.2 Vis-OCT angiographic imaging using dynamic contrast

Figure 3.3 compares the cross-sectional OCT structural B-scan and angiographic contrast acquired from a rat retina *in vivo*. In the OCT structural B-scan, Fig. 3.3(a), the anatomical features of the retina can be clearly distinguished and are labeled accordingly. In addition, two major circulation systems in the eye, the retinal circulation and choroidal circulation, is revealed in the OCT angiogram, Fig. 3.3(b). The structural and angiographic B-scans are further overlaid in Fig. 3.3(c), showing locations of each vessel within the retina. The location of OCTA contrast reregisters well with the structure image, with major blood contrast originating from the inner boundary of the nerve fiber layer (NFL), inner boundary of the outer plexiform layer (OPL), and in the choroid layer. However, caution must be asserted where the highly scattering outer retinal layers (photoreceptors and retinal pigment epithelium, RPE) create vessel artifacts due to shadowing from the inner retina vessels.

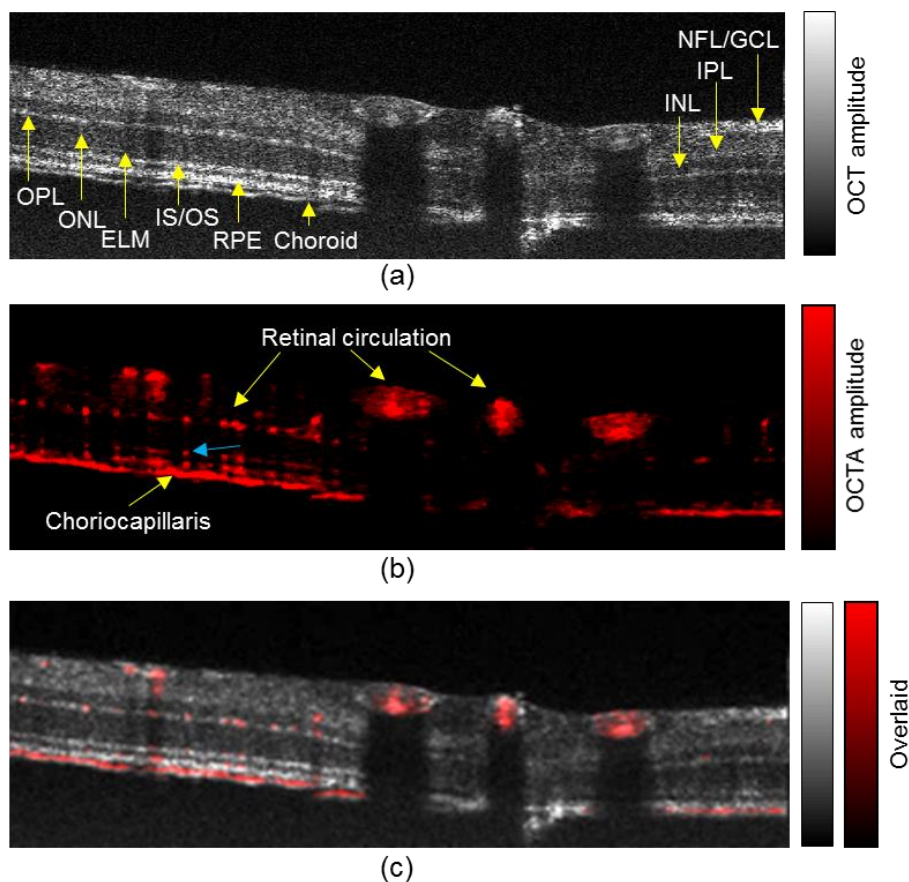


Figure 3.3 Cross-sectional B-scan from (a) OCT structural image, and (b) OCTA contrast, in rat retina *in vivo* using vis-OCT. Anatomical layers labeled include: NFL/GCL-nerve fiber layer/ganglion cell layer, IPL-inner plexiform layer, INL-inner nuclear layer, OPL-outer plexiform layer, ONL-outer nuclear layer, ELM-external limiting membrane, IS/OS-inner segments/outer segments, and RPE-retinal pigment epithelium. Vessels in retinal circulation and choriocapillaries are identified. Artifacts created by the hyper-reflective layers in IS/OS and RPE are indicated with a blue arrow. (c) Overlaid image from (a) and (b). The choriocapillaris lays beneath RPE layer.

Figure 3.4 further compares the *en face* fundus projection using OCT structural image and angiographic contrast. Although superficial vessels, i.e. branch retinal arteries and veins, can be clearly visualized, smaller vessels and the capillary bed cannot be well resolved in the conventional structural image, Fig. 3.4(a). In contrast, the OCT angiographic image from the same field-of-view (FOV), Fig. 3.4(b), enhances the contrast of the blood vessel by removing hyper-reflective signals

from surrounding static tissues. Notably, the choriocapillary layer is excluded through simple segmentation as it appeared as a single bright layer due to limited lateral resolution. Finally, Fig. 3.4(c) renders three-dimensional (3D) vascular structure. Besides the dominating branches of central retinal arteries and veins, spatial distribution of retinal circulation vessels, including laminated micro-vasculatures structures of within nerve fiber layer (NFL) and outer plexiform layer (OPL), can be appreciated.

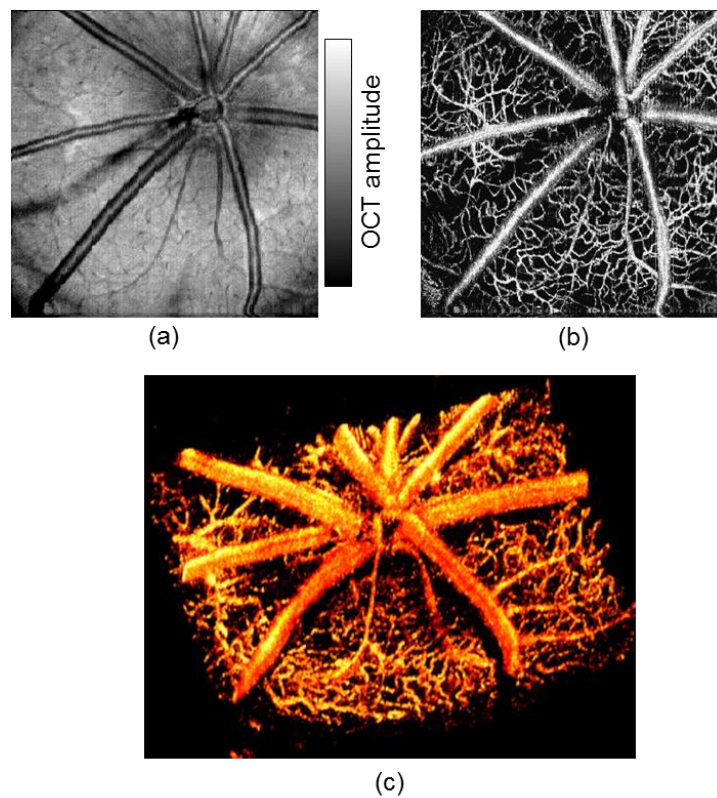


Figure 3.4 Vis-OCT *en face* fundus projection of a rat retina using *in vivo*. (a) Vis-OCT structural fundus image (b) Vis-OCT angiographic fundus image. (c) Three-dimensional (3D) of rat retinal microvasculature.

3.4.3 Measuring absolute retinal circulation sO₂ using spectroscopic OCTA

Spectral derivative ($\partial I/\partial \lambda$) from 565 nm to 574 nm are calculated using all identified retinal circulation arteries and veins. Following the step 5 outlined in table 3.1, mean arterial $\partial I/\partial \lambda$ from 8 rats under each inhalation states are calibrated against systemic spO₂ readings using linear least-squares fitting. Figure 3.5 plots the calibrated OCTA arterial sO₂ against systemic spO₂. The linear regression indicates strong positive correlation ($R^2 = 0.87$) between the two independent measurements, indicating that the calibrated OCTA oximetry using spectral derivative offers reasonably good estimation of the true sO₂.

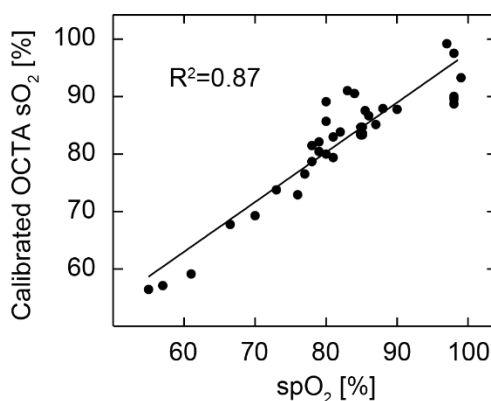


Figure 3.5 Measured arterial sO₂ calibrated against pulse oximetry readings ($R^2=0.87$) from n=8 rats. Black line is the linear regression of the data

Using the established calibration curve, sO₂ from branch retinal arteries and veins are retrieved. The mean and S.D. arterial and venous sO₂ from 8 rats during inhalation oxygen challenge are plotted in Fig. 3.6. The supplying gas compound is alternated in the order of normal air, 5% CO₂, pure oxygen, and 10% oxygen. As one can see, the arterial and venous sO₂ are significantly different ($p < 0.05$), except when pure oxygen was inhaled and the shunting between arterioles and venules elevated the venous sO₂. Besides the arteriovenous sO₂ difference, one can also observe a moderate increase ($p=0.06$) in both arterial and venous sO₂ when we supplied 5% CO₂ gas. This

increased sO_2 is expected because 5% CO_2 has the effect of vasodilation, which improves tissue oxygenation [102, 103]. Both the arterial and venous sO_2 increased significantly ($p < 0.05$) under pure O_2 and decreased significantly ($p < 0.01$) under 10% O_2 .

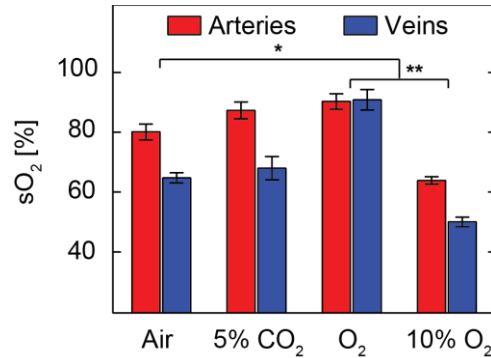


Figure 3.6 Measured mean sO_2 of branch retinal arteries and veins upon changes of inhalation gas mixtures ($n=8$ for each bar). Error bar = S.E.M. *: $p < 0.05$. **: $p < 0.01$.

3.4.4 Measuring relative sO_2 change in choriocapillaris using OCTA

Unfortunately, individual choriocapillaris are not resolvable due to tissue scattering and the limited lateral imaging resolution of the current set-up. Instead, the mean spectral derivative ($\partial I / \partial \lambda$) is retrieved from the OCTA segment containing the entire choriocapillary layer. Notably, image segmentation is performed to remove areas that are shadowed by superficial retinal vessels. In addition the OCTA spectrum is further normalized by the structural OCT intensity spectrum from the layer directly above RPE, which serves as the best estimation for I_0 in the summarized step 3.

The $sO_2 - \partial I / \partial \lambda$ calibration curve cannot be established for choriocapillary measurements due to lack of well-defined reference points. Thus, the same calibration coefficients from the retinal circulation curve is used to convert $\partial I / \partial \lambda$ fluctuation into relative sO_2 change. The relative sO_2 fluctuation with respect to the baseline sO_2 from normal air breathing is plotted in Fig. 3.7 against

different inhaling gas compounds. When 5% CO₂ gas mixture is supplied, the average sO₂ in choriocapillaris increases moderately by 2% ($p = 0.29$). When pure O₂ or 10% O₂ gas mixture are supplied, the average sO₂ increases by 3.5% ($p < 0.001$) or decreases by 5% ($p < 0.001$), respectively.

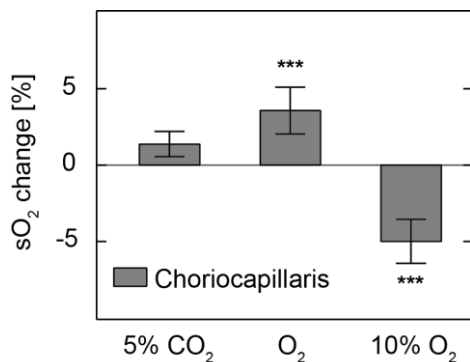


Figure 3.7 Measured relative choriocapillaris sO₂ change comparing to normal air breathing ($n = 6$). ***: $p < 0.001$

3.5 Discussion

In this chapter, an extended theoretical formulation for OCT angiography-based oximetry is presented. Using spectral derivative within the wavelength range of 565 nm to 574 nm, this approach provides robust oximetry results with little blood flow-dependency. The use of OCTA contrast allows retrieval of sO₂ from smaller vessels and in choroidal capillaries. In addition, the need for complex image segmentation is almost eliminated entirely for even smoother application.

Most importantly, measurements of relative sO₂ variations in choriocapillaris right beneath the RPE under different inhalation conditions is achieved. The choroidal circulation is very different from the retinal circulation, both anatomically and functionally [104]. The choroidal blood is supplied through posterior ciliary arterioles and drained through vortex vein. In the context of

blood sO_2 , the major difference between the two circulations is that the choroidal circulation has a very small arteriovenous sO_2 difference, whereas the retinal circulation has a large arteriovenous sO_2 difference [105, 106]. This results in an almost uniform sO_2 level in the choriocapillaris under normal physiology conditions, which allows us to measure average sO_2 over a relatively large area of choriocapillaris.

However, there are a few complications that prevent absolute sO_2 measurements in choriocapillaris. First, the true sO_2 level in choriocapillaris is still unknown. The most accurate reference is the direct measurement of oxygen tension using an invasive oxygen sensitive microelectrode [104]. Although it is commonly assumed that the choroidal circulation has the systemic oxygenation as in the arterioles, the microelectrode measurements turned out to be lower than expected [104]. Without a reliable reference, it is not possible to calibrate spectral derivative as per retinal vessels. Alternatively, one might consider using the least squares fitting method with the full spectral range of the hemoglobin absorption contrast to characterize choriocapillaris sO_2 . However, the optical properties of dispersed single blood cells in capillary network are not entirely clear, which would bring another uncertainty in the least square fitting method. Second, light passes through entire retina before reaching choriocapillaris. The accumulated attenuation is also wavelength dependent, which would affect the spectral derivative. Nonetheless, the presented work is the first time a non-invasive measurement can be implemented to measure relative choriocapillaris sO_2 variations.

In addition, the introduction of spectral derivative approach has the potential to limit the exposure spectral range to 560 nm – 580 nm without significant loss in the OCTA axial resolution. Though the relative wide illumination band (520 nm – 610 nm) is still used in this work, future

applications can benefit by limiting the exposure bandwidth, and thus reduce the incidence power by about 2/3. By removing unnecessary exposure, the laser safety margin for vis-OCT can be significantly improved and the discomfort can be dramatically reduced. Though OCTA oximetry using the shorter spectral range requires independent oxygenation measurements for calibration purpose, this requirement can be easily satisfied using a pulse oximeter measuring systemic arterial spO_2 . The measured spO_2 is equal to sO_2 in major retinal arteries immediately exiting optic nerve. This allows the calibration of spectral derivatives and yields absolute sO_2 measurements.

CHAPTER 4

A combined SLO/OCT ophthalmological imaging system for human subjects

This chapter presents the development of a combined laser scanning ophthalmoscopy (SLO) and optical coherence tomography (OCT) imaging system for human subjects using visible-light illumination. The faster SLO provides guidance and real-time image feedback for alignment purpose. The OCT subsystem acquires high quality three-dimensional tomography of the retina. The unique advantage of the system lies in its sub-micrometer axial resolution and spectroscopic analysis capability for retinal oximetry.

The first part of this chapter describe the hardware implementation of the combined visible-light SLO/OCT ophthalmic imaging system. Its imaging capability is demonstrated and compared against a commercial NIR-OCT.

In the second part, the feasibility of retinal oximetry using visible-light OCT (vis-OCT) is demonstrated. To overcome the challenge of low signal-to-noise ratio (SNR) associated with human vis-OCT images, a statistical fitting-based approach is introduced to retrieve true OCT intensity from noisy images. Retinal oximetry results from four healthy subject are presented.

4.1 Introduction

There are growing evidences suggesting that tissue activity alters well before observable structural changes during pathological development of retinal diseases [107-112]. Retinal metabolic rate of oxygen (rMRO₂), a key biomarker of cell metabolism, shows signs of variation in early stages of leading blinding diseases such as diabetic retinopathy (DR) and age related macular degeneration (AMD) [107, 110, 113, 114]. Monitoring rMRO₂ can provide a practical approach for early disease screening, evaluation of disease severity, and monitoring response to therapeutic intervention. Thus, it has the potential to transform the current reactive eye care practice into preventive medication, greatly reducing the cost and improving outcome.

Direct measurement of rMRO₂ by monitoring cellular respiration at high spatial and temporal resolution remains challenging, if not impossible. To date, most researchers still relies on mass balance equation to infer regional oxygen consumption, i.e. the difference of oxygen content between the supplying and draining blood vessels. Two parameters are generally needed, retinal blood flow (RBF) and blood oxygen content. RBF reflects the rate of oxygen-rich blood is supplied, and can be reliably quantified using the state-of-the-art ophthalmic imaging tools [72, 80, 115]. Meanwhile, the measurement of blood oxygen content is quite a different story.

Direct measurement oxygen tension (pO₂) using intra-retina microelectrode is by far the most accurate approach in laboratory ophthalmic research [112, 116-118]. Unfortunately, its highly invasive nature prevents it from clinical applications. Only approximate measurements from retinal surfaces have been reported on human subjects undergoing surgical procedures (vitrectomy) [116]. In addition, it is often impractical to generate pO₂ map over a larger retinal area using microelectrodes, as is required for diagnosis and monitoring purpose.

Non-invasive or minimally invasive imaging-based methods are thus preferable to investigate the spatial variation of retinal oxygenation. Potential candidates include functional magnetic resonance imaging (MRI). MRI can detect dynamic retinal oxygenation response following inhalation challenge in humans [119, 120]. However, it has low resolution and provides only qualitative measurement. Most importantly, this approach relies on dynamic contrast variation after oxygen challenge and cannot provide steady-state measurements [120]. Meanwhile, optical imaging techniques are also viable choices in ophthalmological applications. For example, phosphorescence lifetime imaging, a technique frequently used in laboratories on non-human animal subjects, can reveal retinal pO_2 using oxygen-dependent emission quenching of the injected phosphorescent dye [121, 122]. Unfortunately, the introduction of toxic fluorescent dye into systemic circulation makes it inappropriate for clinical applications.

Over the past decades, researchers have turned their focus onto intrinsic hemoglobin absorption contrast. Depending on whether the binding sites have been occupied by oxygen molecules, hemoglobin has two forms, oxyhemoglobin (HbO_2) and deoxyhemoglobin (HbR), which have distinctively different optical absorption spectra within the visible and near-infrared (NIR) spectral range. Thus, their relative concentration can be determined by measuring the combined absorption spectrum of blood. Multi-wavelength fundus photography [108-111], multi-wavelength scanning laser ophthalmoscopy (SLO) [123], and hyperspectral imaging [124, 125] are all examples of measuring retina circulation sO_2 using hemoglobin absorption contrast in human. These three approaches share the same imaging principle, which relies on back-scattered photons within blood vessels. The major drawback, however, is their inability to provide depth resolved image. As it is impossible to differentiate signals from within blood and other retinal layers, they inevitably suffer from interference from (1) multiply scattered photons, (2) variations in blood vessel

diameter, and (3) melanin concentration in the retinal pigment epithelium (RPE). A previous numerical study using Monte Carlo simulation suggests that all these factors can collectively contribute up to 20% error in sO_2 measurements [55]. One answer to this issue is to use multi-wavelength photoacoustic ophthalmoscopy (PAOM) to directly map the optical absorption spectrum of the tissue. Its three-dimensional (3D) imaging capability improves its tolerance toward interfering layers. Though successfully demonstrated on animal organs *in vivo* [76, 92, 126], PAOM have not been applied to measuring retinal circulation sO_2 in human. One major hindering factor is that PAOM requires physical contact between tissue and the ultrasonic transducer, which complicate its application and introduces concerns such as infection.

Recently, functional optical coherence tomography (OCT) has emerged as a non-invasive imaging modality suitable for quantifying blood sO_2 using hemoglobin absorption contrast [30-35, 94, 95]. In the chapter 2 of this dissertation, the feasibility and accuracy of retinal OCT oximetry is investigated using both numerical simulation and experimental data. Chapter 2 also demonstrates that visible-light (wavelength range 500 nm – 600 nm) is more appropriate than NIR (wavelength longer than 800 nm) for OCT oximetry. In summary, here lists a few key factors that contribute to the conclusion. First and most importantly, sO_2 -dependent hemoglobin optical absorption has the strongest spectral contrast within the visible-light wavelength range, which facilitates inverse sO_2 quantification [66]. Second, optical-scattering cross-section in biological tissue is often inversely correlated with the wavelength, giving visible-light OCT (vis-OCT) image stronger back-scattered intensity than NIR ones under same illumination irradiance [127, 128]. In addition, using a shorter wavelength range, vis-OCT has intrinsically higher axial and lateral imaging resolution than its NIR counter parts with comparable bandwidth, further improving its performance. Previous studies have shown the capability of vis-OCT to quantify retinal sO_2 in

rodents under both normal conditions and during oxygen challenge [35, 129, 130]. In addition, dynamic $rMRO_2$ measurement was also demonstrated [129].

Unfortunately, all commercially-available clinical OCT retinal imaging systems used NIR illumination, precluding the possibility of OCT retinal oximetry. The work presented in this chapter focuses on translating vis-OCT retinal oximetry from benchtop to clinical applications. If vis-OCT retinal oximetry can be successfully developed for human subjects, it will have the following advantages: (1) 3D imaging and coherent detection minimize the influence from surrounding tissues to warrant high sO_2 quantification accuracy; (2) vis-OCT has access to a more continuous optical absorption spectrum of blood, which facilitates inverse calculation since spectral fitting provides much higher sample density than discrete multi-wavelength measurements in other modalities; (3) because conventional OCT is routinely used in ophthalmic clinics worldwide, adding functional imaging capability to OCT will enable a quick clinical adoption [131]; (4) OCT is a versatile technology which has already demonstrated accurate measurement of vessel diameter and blood flow velocity within retinal vessels [80, 92]. Therefore, vis-OCT, providing both sO_2 and blood flow measurements, has the potential to quantify $rMRO_2$ by a single imaging modality, which has not been previously possible.

The first part of this chapter presents a novel hardware implementation of vis-OCT prototype for human imaging. The system is improved and translated from the previously reported rodent vis-OCT system [132]. The combined SLO/OCT imaging system share the same visible-light illumination source. Its imaging capability around fovea and optic nerve head (ONH) is demonstrated and compared against a commercial NIR OCT system.

Using the implemented vis-OCT prototype, the second part seeks to quantify retinal circulation sO_2 in healthy human volunteers. A statistical fitting-based algorithm is developed to sample true OCT intensity from human vis-OCT images with low signal-to-noise ratio (SNR). This is non-trivial because human vis-OCT images have lower quality compared with that of rodents, suffering from reduced illumination power and stronger optical attenuation from larger eyeball. Finally, vis-OCT oximetry results reveal that retinal arteries and veins in close proximity to the optic nerve head had around 20 percentage points (pp) difference in blood sO_2 . Moreover, sO_2 variations at different arterial branch levels are observed.

4.2 Developing the hardware platform for vis-OCT imaging

4.2.1 A combined visible-light SLO/OCT ophthalmoscope prototype for imaging human subjects

Figure 4.1 illustrates the schematic diagram of the visible-light SLO/OCT dual modality ophthalmic imaging system. Both the SLO and OCT subsystems share the same supercontinuum light source (SuperK EXW-6, NKT Photonics). The ultra-broad-band light output from the supercontinuum source is first filtered using a pair of edge pass filters (FF01-496/LP and BSP01-633R, Semrock) toward the desired wavelength range from 496 nm to 632 nm. The filtered light is then delivered to a free-space Michelson interferometer via a single-mode fiber (P3-460B-FC, Thorlabs). The Michelson interferometer consists of a 70:30 (reflection : transmission) cube beam splitter (BS019, Thorlabs). This configuration ensures that the majority of the back-scattered photons from the sample is directed towards the detection arm. In the sampling arm, a pair of

galvanometer mirrors (QS-7, Nutfield Technology) raster-scanned the beam across a user-defined acquisition angle. The scanning pattern is then projected onto the retina via a Keplerian telescope ($0.7\times$ magnification, Focal length 50 mm : 35 mm). The distance between these two lens elements can be adjusted to compensate for the refractive error of the eye. In the reference arm, dispersion mismatch and intensity are carefully balanced using BK-7 glass plates and a continuously adjustable reflective ND filter (NDC-50C-2M, Thorlabs), respectively.

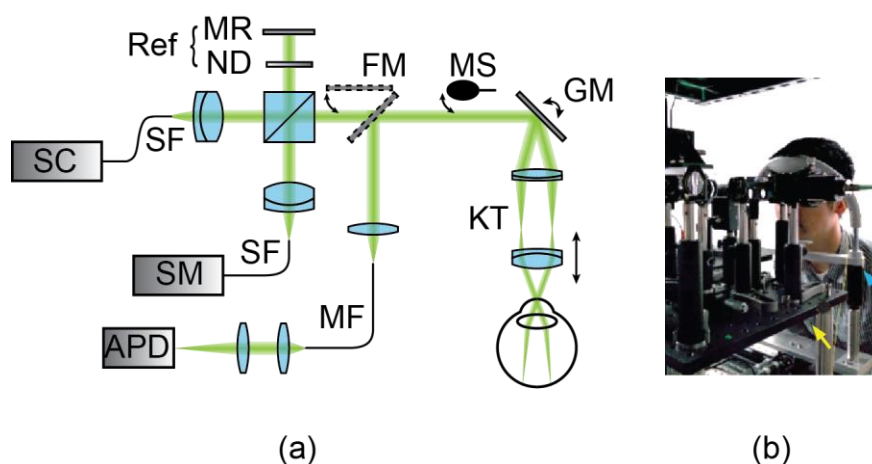


Figure 4.1 (a) Schematic of the combined visible light SLO and OCT prototype system for human subjects. SC: Supercontinuum laser source; SF: Single-mode fiber; SM: Spectrometer; Ref: Reference arm; MR: Reflective mirror; ND: Neutral density filter; FM: Motorized flip mirror; MS: Motorized beam stop; GM: Galvanometer mirror; KT: Keplerian telescope; MF: Multimode fiber; APD: Avalanche photodiode. (b) photograph of system. A blue arrow points to the three-dimensional translational chin rest for adjusting eye position; a yellow arrow points to the stationary optics board.

The SLO and OCT subsystems have separate detection scheme. The SLO subsystem provides guidance and acquires rapid alignment image for the slower vis-OCT subsystem. During SLO imaging, a 50/50 beam splitter (FM, BS004, Thorlabs) is flipped into the optical path of the sampling arm. The reflected light from the sample is then focused onto the core of a multimode fiber ($50\ \mu\text{m}$ core size, M16L01, Thorlabs), which also serves as a pinhole. An avalanche

photodetector (APD110A2, Thorlabs) sample the intensity and the data is recorded using a multifunction acquisition card (PCI-6251, National Instruments) at 100 kHz sampling rate.

When the system operates in the vis-OCT mode, the reflected sampling and reference beams are recombined at the beam splitter, recoupled into a single-mode fiber, and delivered to a homemade spectrometer. The spectrometer consists of an 1800-lpmm transmission grating (Wasatch Photonics) set at Littrow's angle optimized for a center wavelength of 564 nm. A line scan camera (spL2048-140km, Basler) digitize the dispersed spectrum at a speed of 25 kHz. The exposure time is set to 37 μ s, allowing 3 μ s for data readout. The spectrometer is calibrated to cover the spectral range from 506 nm to 621 nm, which is slightly narrower than the illumination spectrum to ensure all spectrometer pixels are utilized.

The entire optical system is mounted on a stationary optical breadboard. Proper Eye position is accomplished using a 3D motorized translational stage to move the head of the subject with respect to the imaging optics.

4.2.2 Imaging acquisition protocols

Either one or both eyes are imaged for each volunteer. When being imaged, the subject is instructed to follow a fixation target using the fellow eye. SLO imaging is usually performed first as it is inherently faster and more suitable for alignment purposes. Two raster scanning protocols are subsequently used to optimize imaging quality. First, low density (LD) SLO images (256 \times 64) are acquired at 6 frames-per-second (FPS) with real-time display. It helps to locate the desired region-of-interest (ROI) and provide a reference for rough refractive error adjustment. Then, a series of high density (HD) SLO images (512 \times 512) are taken. Between each acquisition, the

imaging Keplerian telescope is fine tuned to achieve highest SLO image quality by correcting as much refractive error as possible. Each HD SLO acquisition took 2.6 seconds.

Then the system is switch to vis-OCT mode by automatically removing the 50:50 beam splitter (FM) out of the sampling optic path. The vis-OCT subsystem should be imaging the same ROI as the SLO subsystem. However, the location of the reference mirror still needs to be adjusted to match the optical path length between the sampling and reference beam. During axial alignment, LD vis-OCT images (128×32 A-lines) are acquired and processed at 6 volumes per second (VPS) continuously. Finally, HD vis-OCT images are acquired using one of the following resolution: 256×256, 256×512, 512×512, 2048×128, or 4096×64 A-lines. The selected values represent the tradeoff between image quality, imaging time, and total light exposure.

The entire imaging session is limited to 5 minutes per eye to avoid discomfort from prolonged exposure to bright visible light. As a safety measurement, an electronic beam shutter automatically block the light to avoid unnecessary exposure before and immediately after the acquisition. For added the security, the galvanometer mirrors are also programed to divert the probing light into a beam dumper after each imaging session.

4.2.3 Laser safety considerations

The maximum permissible exposure (MPE) are calculated according to ANSI standards according to equations 17 – 20 in reference [133] by Delori *et al.* Though these equations were originally laid out for SLO, they also applies to the OCT imaging modality as the two share the same scanning scheme. To be conservative, the parameters used in the calculation represents the highest illumination density encountered, which correspond to the smallest scanning field-of-view

(FOV) ($10^\circ \times 10^\circ$ square), the highest scanning density (512×512) and the lowest rate (25 kHz). Following the calculation, the maximum permissible exposure (MPE) is 3.6 mW for continuous exposure up to two hours.

The incident visible-light illumination power is $226 \mu\text{W}$ at the pupil plane. It is more than ten times weaker than the ANSI MPE and should be considered safe. The detailed calculations for the MPE can be found in appendix A.

4.2.4 Human subject recruitment

The presented study is approved by the Northwestern University Institutional Review Board (IRB), and adheres to the tenets of the Declaration of Helsinki. All procedures take place in the Ophthalmology Department at the Northwestern Memorial Hospital. Healthy volunteers are recruited during their routine clinical visits. Informed consents are obtained from all participating volunteers. Prior to imaging, all subjects underwent a complete eye examination performed by an ophthalmologist. Inclusion criteria required that the subject should have normal or near-normal vision. If the subject wore corrective lenses, they were eligible if the refractive error was in the range of +2 to -6 diopters. Subjects with known retinal diseases, significant cataract, or vitreous cloudiness were excluded. Subjects underwent pupil dilation during their routine eye examination before vis-OCT imaging.

For each volunteer, the whole procedure consisted of three to four sessions; each session included SLO and/or OCT imaging, as described above. The total time of a session was limited to five minutes, even if the images were not satisfactory. Volunteers were allowed to freely blink. Between the two sessions, volunteers were allowed to rest for at least five minutes to recover.

After finishing all the imaging sessions, we asked the volunteers to rate the comfort of the procedure, and we monitored the subjects until their vision returned to normal, which usually took around five minutes or less. All the volunteers were evaluated using standard clinical retinal NIR-OCT and fundus auto-fluorescence (488nm and 787nm) imaging, and showed no sign of retinal damage.

4.2.5 Data processing

All acquired data are post-processed using MATLAB (R2013b, MathWorks). For the SLO data sets, each acquisition sequence is projected back to Cartesian coordinates to generate fundus image. Histogram equalization is employed to enhance the image contrast. 3×3 median filtering is also applied to remove excessive salt-and-pepper noise [134]

Structural vis-OCT images are reconstructed following algorithms reported earlier for Fourier domain OCT (FD-OCT). Briefly, the background spectrum and fixed pattern noise is subtracted from each A-line. It is then linearly resampled to be equal interval in wave number (k -space). Following fast Fourier transform operations, the modulus of the complex OCT signal is calculated to generate vis-OCT amplitude images. Axial eyeball motion is corrected using rigid cross-correlation between adjacent B-scans. *En face* fundus image is generated by projecting mean OCT intensity across the entire retina thickness on the axial direction. All vis-OCT images are displayed in logarithm scale to enhance the dynamic range.

4.2.6 Results

4.2.6.1 Performance

The theoretical axial resolution for the vis-OCT subsystem is estimated to be $0.75\ \mu\text{m}$ in vacuum (or $0.54\ \mu\text{m}$ in tissue, assuming refractive index $n=1.38$) when considering optical double-pass in the sampling arm. The actual axial resolution, as well as detection sensitivity and sensitivity roll-off, are characterized using the same method as described in section 2.3.1.2 of Chapter 2. Briefly, a silver mirror is placed at the pupil plane to reflect the sampling beam. One additional neutral density (ND) filter (Optical density = 2.0, Thorlabs) is also inserted into the optical path to bring the light intensity into normal imaging range.

Figure 4.2 plots the axial impulse response of the vis-OCT system against increasing imaging depth. The first two peaks have the highest amplitude and narrowest width. In accordance with the normal practice that imaged features are roughly placed at a depth of $200\ \mu\text{m}$ near the zero-delay line, the second peak is chosen as the benchmark for sensitivity and axial resolution. Thus, the system sensitivity of the vis-OCT subsystem is estimated to be 86 dB based on its relative height (46 dB) against the noise floor and the 40 dB attenuation introduced by the inserted ND filter. The full-width-half-maximum (FWHM, -6 dB) of the first peak is $0.97\ \mu\text{m}$, which is about 129% of the theoretical value.

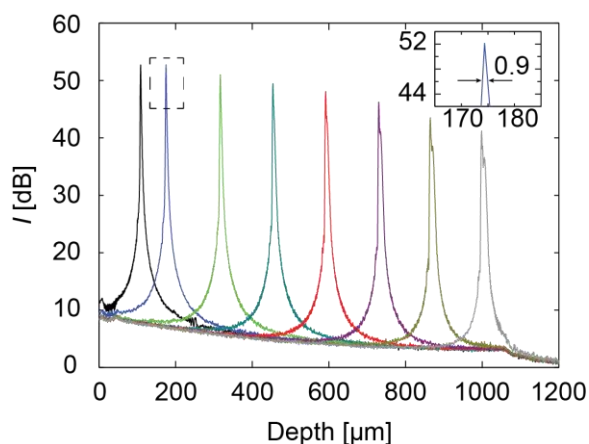


Figure 4.2 OCT axial impulse response from the reflection of a mirror surface. The insert shows a magnified view of the height and full-width-at-half-maximum (FWHM) of the second peak.

4.2.6.2 SLO and vis-OCT fundus images centered on fovea

All images presented are taken from a healthy 32-year-old male volunteer. The subject has moderate myopia and wears prescription eyeglass (-3.0 Diopter) for far seeing. The refractive error is corrected by adjusting the Keplerian telescope prior to HD acquisition. Figure 4.3 shows HD SLO images (512×512) of the subject's right eye centered on fovea. The left image, Fig 4.3(a), covers the FOV of 20°×20°. The center hyper-reflective area corresponds to the foveal avascular zone (FAZ). There is a dark spot in the center of the FAZ, corresponding to the fovea umbo. The hyper reflective ring in the para fovea region is possibility caused by specular reflection due to the physiological curvature of the retina in the region.

Figure 4.3(b) further magnified the region indicated by the red box from HD SLO scan over a smaller 10°×10° FOV. Retinal capillaries surrounding the fovea can be clearly visualized

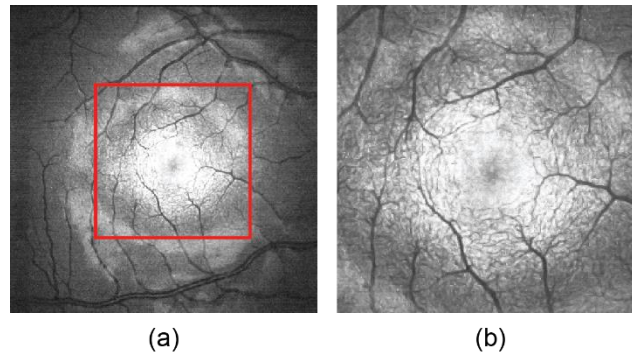


Figure 4.3 SLO image centered at the fovea. (a) $20^{\circ} \times 20^{\circ}$ FOV. (b) $10^{\circ} \times 10^{\circ}$ FOV, magnification of the red box.

The vis-OCT images of the same ROI are shown in Fig. 4.4. The projected *en face* vis-OCT fundus image, Fig. 4.4(a) and (b), show similar retinal capillary features as the corresponding SLO image. Figure 4.4(c) is a vis-OCT HD B-scan consisting of 2048 A-lines, acquired separately at the location indicated by the dashed line. A total of 12 retinal layers can be recognized from the cross-section. The inner retina shows weaker scattering compared with the outer retina and the retinal pigment epithelium (RPE). Especially in the outer retina, the boundary between the photoreceptor inner and outer segment (IS/OS), the outer segment of photoreceptors (OS), and the RPE have strong OCT intensity, indicating increased back-scattering in these layers. Meanwhile, the nerve fiber layer (NFL) have the highest signal strength among inner retina layers.

In addition, the vis-OCT B-scan also reveals that NFL on the nasal side of the fovea is much thicker than the temporal side. In addition, the Bruch's membrane (BM) can be distinctly resolved in the vis-OCT image due to its sub-micrometer axial resolution. However, little light penetrates through the RPE due to its strong optical absorption. As a result, choroid is not visible in the cross-sectional image.

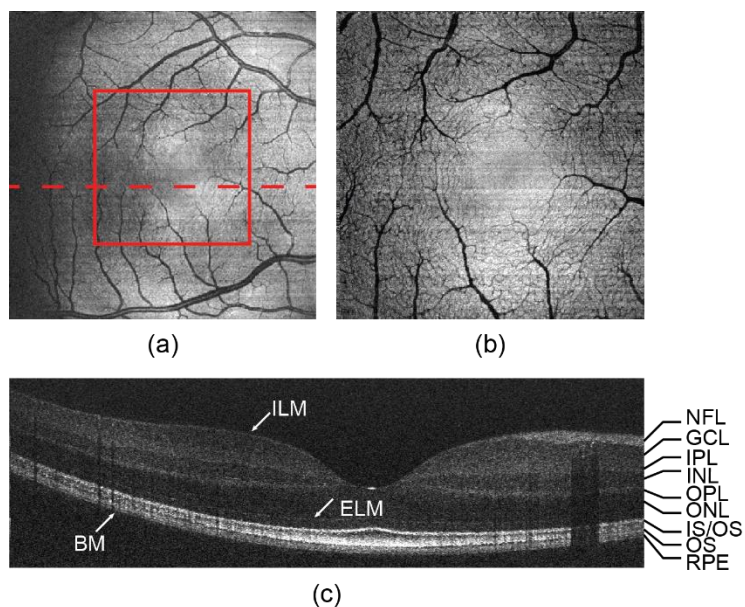


Figure 4.4 Vis-OCT image centered on fovea. (a) $20^{\circ} \times 20^{\circ}$ FOV. (b) $10^{\circ} \times 10^{\circ}$ FOV, magnification of the red box. (c) Vis-OCT B-scan crosssection image showing layered retinal structures around fovea, acquired from the location highlighted in (a). 12 distinctively identified layers are labeled: ILM: Inner-limiting membrane; NFL: Nerve fiber layer; GCL: Ganglion cell layer; IPL: Inner plexiform layer; INL: Inner nuclear layer; OPL: Outer plexiform layer; ONL: Outer nuclear layer; IS/OS: Inner/outer segment junction; OS: Outer segment of photoreceptor; RPE: Retinal pigmented epithelium; BM: Bruch's membrane.

4.2.6.3 SLO and vis-OCT fundus images centered on optic nerve head (ONH)

Figure 4.5 shows the HD SLO imaging result centered on ONH from the same healthy male volunteer. The FOV of Fig. 4.5(a) and (b) covers $20^{\circ} \times 20^{\circ}$ and $10^{\circ} \times 10^{\circ}$, respectively. Fig 4.5(b) is acquired at the location indicated by the red box. Both SLO images clearly revealed physiological arrangement of vessels in the retinal circulation. In addition, the fine anatomical structures of lamina cribrosa can be appreciated with high resolution. Unfortunately, the anatomical curvature of the eye cause slight blurring on the right-hand (nasal) side of the image.

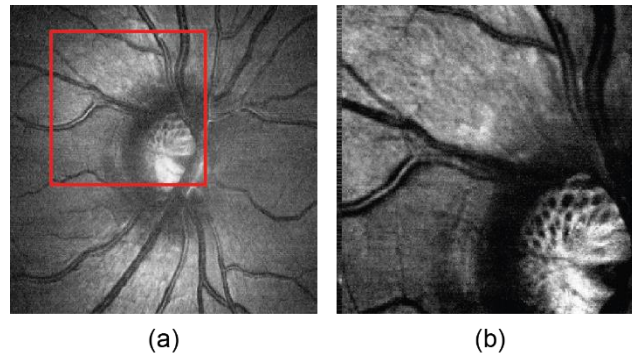


Figure 4.5 SLO image centered at the ONH. (a) $20^{\circ}\times 20^{\circ}$ FOV. (b) $10^{\circ}\times 10^{\circ}$ FOV, magnification of the red box.

Similarly, Fig. 4.6 shows vis-OCT images centered on ONH. Both *en face* projections show similar features as the SLO image. In addition, vis-OCT fundus image visualize the NFL texture originating from stratified axons of ganglion cell. Figure 4.6(c) shows the B-scan consisting of 2048 A-lines extracted from the dashed line shown in Fig. 4.6(a). The normally increased thickness of NFL close to ONH is obvious. Strong absorption in the major retinal blood vessels and most of the smaller vessels creates shadows beneath them. Scattering from blood within the vessels also can be observed.

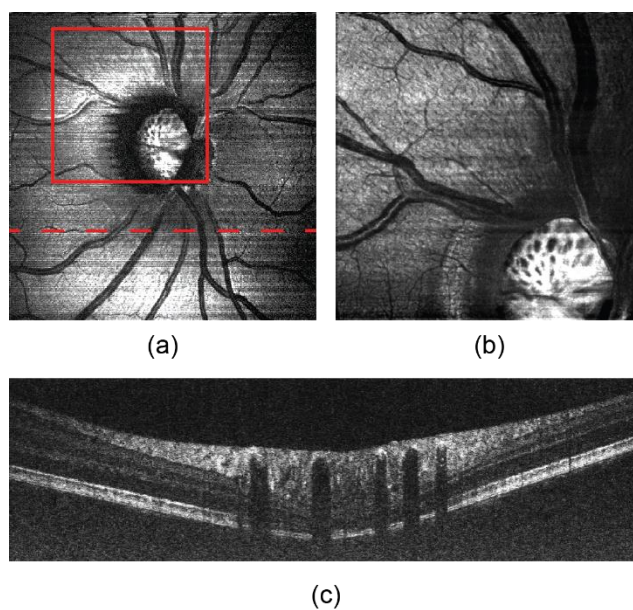


Figure 4.6 Vis-OCT image centered on ONH. (a) $20^\circ \times 20^\circ$ FOV. (b) $10^\circ \times 10^\circ$ FOV, magnification of the red box. (c) Vis-OCT B-scan crosssection image showing layered retinal structures around ONH, acquired from the location highlighted in (a).

Figure 4.7 demonstrate the benefit of sub-micrometer axial resolution when imaging retinal layers. The outer and inner segment are respectively magnified and labeled. In the outer retina, Fig. 4.7(b), the details of IS/OS, OS interdigitation zone, RPE, and BM are clearly distinguishable. Although the RPE melanin attenuates the visible light significantly, OCT signal scattered back from choroid can still be identified in this specific image, which lies immediately beneath BM. In the inner retina layers, Fig. 4.7(c), the fine details of the NFL texture can be visualized. This texture may arise from the regular arrangement of ganglion cell axons.

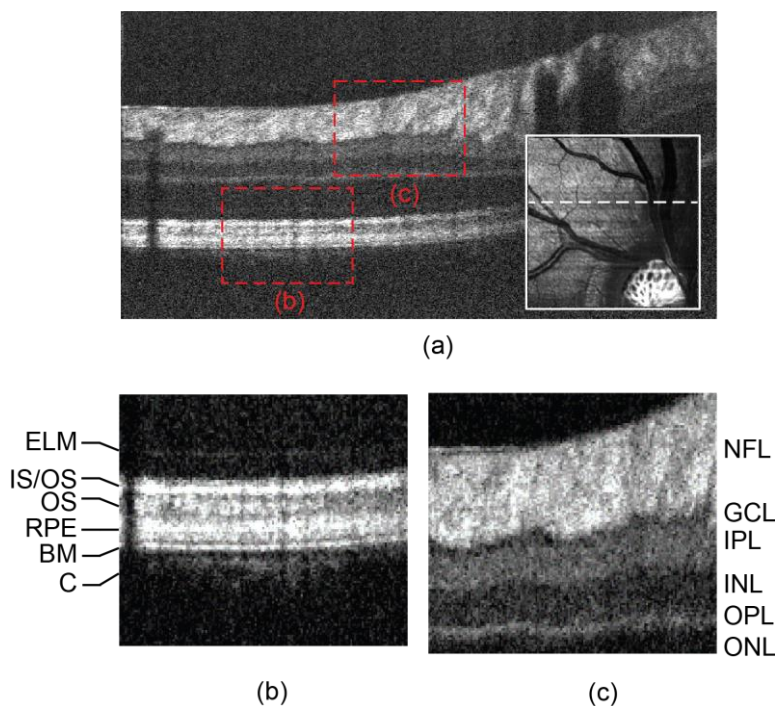


Figure 4.7 (a) Cross-sectional vis-OCT image around ONH. The inset at the bottom-right corner shows the *en face* projection where the B-scan is taken from. (b-c) Magnified in images from the squared areas in (a)

4.2.6.4 Comparison between the vis-OCT prototype and commercial NIR-OCT

Figure 4.8 compares the B-scan cross-sectional image from the vis-OCT prototype and a commercial NIR OCT system (Cirrus-HD-OCT, Carl Zeiss Meditec) from the same healthy male volunteer. The vis-OCT image, Fig. 4.8(a) consist of 2048 A-lines and is averaged from three consecutive B-scans. Though details are not available, similar imaging procedures are believed to be used by the commercial system to generate Fig. 4.8(b).

Admittedly, the vis-OCT image to date has lower SNR than the commercial NIR counterpart. This major drawback is due to the fact that the illumination power used in the vis-OCT prototype is only 226 μW as compared to about ~ 1.0 mW used in the commercial NIR systems.

Despite lower SNR, vis-OCT cross-sectional image still demonstrates superior axial resolution, which facilitate layer separation. The detailed layer identification is presented in the previous section 2.2.6.2 and 2.2.6.3.

In the vis-OCT image, the inner retina other than NFL has considerably lower OCT intensity than that of our retina in the same image or that in the NIR image. One hypothesis is that human retina is naturally designed to transmit visible light, so it may be optimized for visible range used and appears to be less scattering. However, more study is warranty to investigate this phenomenon.

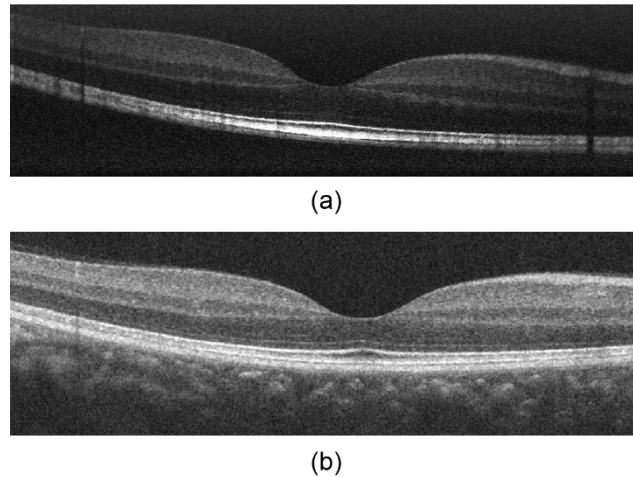


Figure 4.8 Comparison between B-scan image from (a) vis-OCT prototype, and (b) a commercial NIR OCT system (Cirrus-HD-OCT, Carl Zeiss Meditec)

4.3 Retrieving retinal circulation sO_2 using spectroscopic analysis on vis-OCT images

4.3.1 Spectroscopic analysis

The procedures and algorithms for inverse calculation of blood sO_2 through spectroscopic vis-OCT analysis have been discussed in great details in previous publications [34, 35] and in Chapter 2. The accuracy and stability of vis-OCT sO_2 measurements have been established using mathematical modeling [75], phantom experiments *ex vivo* [95, 129], and rodent imaging studies *in vivo* [34, 35, 129]. This section seeks to investigate blood sO_2 variations in retina circulation from healthy human subjects by adopting the established analytical tool chain used in rodent imaging.

Wavelength-dependent OCT is reconstructed from a series of short-time Fourier transforms (STFT) along the spectral domain. The major blood vessels are manually identified and segmented. For each identified blood vessel, back-scattered OCT intensity is calculated from a volume-of-interest (VOI) placed in the middle of the vessel along the longitudinal axis of each identified vessel. The axial thickness of VOI is 25 μm thick. Its length and width depend on the actual vessel geometry so the VOI always reside within the corresponding vessel. The retrieved OCT intensity spectrum is then least square fitted against the known attenuation spectra of oxygenated and deoxygenated whole blood based on the modified Beer-Lambert law described in reference [35].

One major obstacle preventing direct application of the established methods is that human vis-OCT images usually have sub-optimal SNR from lower illumination intensity due to safety and

comfort limitations. Usually the most straightforward approach to cancel of effects of noise is to calculate the arithmetic mean value of a larger VOI within the vessel. Unfortunately, the noises in OCT intensity images are not zero-mean due to the modulus operation applied, biasing the arithmetic mean results. As retrieving unbiased true vis-OCT intensity from the target blood VOI is the key to accurate sO₂ calculation, it is non-trivial to develop a fitting-based approach based on the noise characteristics to retrieve true OCT intensity in vis-OCT images.

4.3.2 Statistical modeling of noises in OCT amplitude images

This section present a statistical fitting method to retrieve unbiased estimation of the true OCT intensity. The approach is based on the statistical distribution model of OCT intensity in noisy images. Though the derivation presented assumes the form of spectral-domain OCT (SD-OCT), it can be adapted for swept-source OCT (SS-OCT).

The model starts by assigning each spectrometer detector element recorded interferogram intensity $D[k_i]$, where i indicate the sequence of the elements ($i = 1, 2, \dots, N$; N is the total number of elements); k_i is the corresponding optical wavenumber for the i^{th} element. Discrete Fourier transform translate the spectral domain interferogram into complex OCT A-line profiles $d[x_i]$ in the spatial domain,

$$d[x_i] = \frac{1}{N} \sum_{n=1}^N D[k_n] e^{-jk_n x_i}, \quad (4.1)$$

where x_i is the depth index. The scaler term, $1/N$, normalizes the transform so that the result is independent of transformation length. OCT intensity can be expressed as the modulus of the complex profile, $|d[x_i]|$. In a noise-free system, $|d[x_i]|^2$ is proportional to the amount of light energy

back-scattered from sample depth x_i . Thus, the goal is to estimate the true value of $|d[x_i]|$ when it is biased by noises, or to address the question that how stochastic noise translates from the spectral domain to the spatial domain.

The derivation presented thereafter assumes a shot-noise limited OCT system. It is an accepted model to study SNR in OCT [42, 43]. Shot-noise originates from the discrete nature of photons, which arrive at the CCD detector at random interval during the exposure time. This stochastic process can be modeled by Poisson distribution. When the photon number is large, it approximates normal distribution. Thus, the general expression of shot-noise limited spectrometer signal for each detector element is,

$$D[k_i] = D_s[k_i] + D_n[k_i], \quad (4.2)$$

where $D_s[k_i]$ is the noise-free signal and $D_n[k_i]$ is an additive noise term. For each k_i , $D_n[k_i]$ is independent and obeys normal distribution, where its expected value $E\{D_n[k_i]\} = 0$. At the current stage, it is safe to assume that all $D_n[k_i]$ share the same variance, $\text{Var}\{D_n[k_i]\} = \sigma^2$. These treatments are consistent with earlier discussion on the SNR of OCT systems [43]. Combining Eq. 4.1 and Eq. 4.2 leads to

$$\begin{aligned} d[x_i] &= \frac{1}{N} \sum_{n=1}^N \{D_s[k_n] + D_n[k_n]\} e^{-jk_n x_i} \\ &= \frac{1}{N} \sum_{n=1}^N D_s[k_n] e^{-jk_n x_i} + \frac{1}{N} \sum_{n=1}^N D_n[k_n] e^{-jk_n x_i} \\ &= d_s[x_i] + d_n[x_i]. \end{aligned} \quad (4.3)$$

Apparently, $d_s[x_i]$ is the noise-free A-line and $d_n[x_i]$ is the additive noise term.

4.3.2.1 Background intensity noise in OCT images

When $d_s[x_i] = 0$, Eq. 4.3 corresponds to the background noise in OCT images. Decomposing Eq. 4.3 using Euler's formula leads to

$$\begin{aligned}
 d_0[x_i] &= d_n[x_i] \\
 &= \frac{1}{N} \sum_{n=1}^N D_n[k_n] e^{-jk_n x_i} \\
 &= \frac{1}{N} \sum_{n=1}^N D_n[k_n] \cos(k_n x_i) - j \frac{1}{N} \sum_{n=1}^N D_n[k_n] \sin(k_n x_i) \\
 &= Re - j \cdot Im.
 \end{aligned} \tag{4.4}$$

For simplicity, one can define $Re = \frac{1}{N} \sum_{n=1}^N D_n[k_n] \cos(k_n x_i)$ and $Im = \frac{1}{N} \sum_{n=1}^N D_n[k_n] \sin(k_n x_i)$. The OCT intensity can thus be expressed as the modulus of the complex profile,

$$|d_0[x_i]| = \sqrt{Re^2 + Im^2}. \tag{4.5}$$

It becomes clear that the statistical distribution of OCT background intensity $|d_0[x_i]|$ depends on the statistical distribution of Re and Im . Here, only explicit analysis on Re is provided, as the two terms are symmetrical and readers can apply the same approach to reach the conclusion for Im . Based on the notion that $D_n[k_i]$ are independent and follow normal distribution, the expected value of Re is,

$$E\{Re\} = E\left\{\frac{1}{N} \sum_{n=1}^N D_n[k_n] \cos(k_n x_i)\right\} = \frac{1}{N} \sum_{n=1}^N \cos(k_n x_i) E\{D_n[k_n]\} = 0,$$

(4.6)

while its variance is,

$$\begin{aligned} \text{Var}\{Re\} &= \text{Var}\left\{\frac{1}{N} \sum_{n=1}^N D_n[k_n] \cos(k_n x_i)\right\} = \frac{1}{N^2} \sum_{n=1}^N \cos^2(k_n x_i) \text{Var}\{D_n[k_n]\} \\ &= \frac{1}{N^2} \sigma^2 \sum_{n=1}^N \cos^2(k_n x_i). \end{aligned}$$

(4.7)

Here one can introduce a scalar, $C = \frac{1}{N} \sum_{n=1}^N \cos^2(k_n x_i)$, to simplify the expression to $\text{Var}\{Re\} = \frac{C}{N} \sigma^2$. When N is large, C is approximately 0.5. In addition to the known mean and variance expression, Re also follows normal distribution, as it is the weighted sum of independent normally distributed random variables. Thus, one has $Re \sim \text{Normal}\left(0, \frac{C}{N} \sigma^2\right)$. Similarly, it can also be obtained that $Im \sim \text{Normal}\left(0, \frac{C}{N} \sigma^2\right)$. One can further prove that Re and Im are uncorrelated, as their covariance are zero due to the orthogonality of the trigonometric functions. In addition, as the vector pair $\langle Re, Im \rangle$ satisfies the definition of multivariate normal distribution, it leads to the conclusion that that Re and Im are indeed two independent random variables, even though they share the same origin.

Upon inspection of Eq. (5), it becomes clear that OCT background intensity $|d_0[x_i]|$ follows generalized chi distribution with two degrees of freedom, or Rayleigh distribution. The probability density function (pdf) of $|d_0[x_i]| = t$ is,

$$f(t) = \begin{cases} \frac{Nt}{c\sigma^2} e^{-\frac{Nt^2}{2c\sigma^2}}, & t > 0; \\ 0, & \text{otherwise.} \end{cases} \quad (4.8)$$

Thus, the background noise intensity distribution in a shot-noise limited OCT image is established.

4.3.2.2 Feature intensity noise in OCT images

When $d_s[x_i] \neq 0$ in Eq. 4.3, the expression corresponds to the imaged features in OCT images. The same analytical chain shown in section 4.3.2.2 can be applied. Similarly, one can decompose the noise-free A-line into real and imaginary parts, $d_s[x_i] = a + jb$, where a and b are both deterministic functions of x_i . $|d_s[x_i]| = \sqrt{a^2 + b^2}$ is the desired true OCT intensity. Thus, Eq. 4.4 and Eq. 4.5 can be re-written as,

$$d[x_i] = a + j \cdot b + Re - j \cdot Im = (a + Re) + j(b - Im) \quad (4.9)$$

and

$$|d[x_i]| = \sqrt{(a + Re)^2 + (b - Im)^2}. \quad (4.10)$$

It is again apparent that $(a + Re)$ and $(b - Im)$ are two normally distributed random variables and one has $(a + Re) \sim \text{Normal}\left(a, \frac{c}{N}\sigma^2\right)$ and $(b - Im) \sim \text{Normal}\left(b, \frac{c}{N}\sigma^2\right)$, respectively. Thus, $|d[x_i]|$ follows non-central generalized chi distribution with two degrees of freedom, also known as Rice distribution. The pdf for $|d[x_i]| = t$ is,

$$g(t) = \begin{cases} \frac{t}{\varepsilon^2} e^{-\left(\frac{t^2+v^2}{2\varepsilon^2}\right)} I_0\left(\frac{tv}{\varepsilon^2}\right), & t > 0; \\ 0, & \text{otherwise.} \end{cases} \quad (4.11)$$

I_0 is the modified Bessel function of the first kind. One can further introduce a scaler $\varepsilon^2 = \frac{C}{N} \sigma^2$ to simplify the expression. It has the same expression as the variance of the above Rice distribution. Another scaler $v = \sqrt{a^2 + b^2}$ has the same expression as $|d_s[x_i]|$. Notably, v is independent from the noise term σ . Thus, we have successfully separated OCT signal from noise, while the value of v represents the true OCT intensity. For small signal $v \rightarrow 0$, $g(t)$ degenerates to $f(t)$ as expected. Thus, Eq. (11) can be used as a general expression to model the statistical distribution of OCT pixel intensity.

Figure 4.9 illustrates the above derivation and provides numerical verification through simulation. A sinusoidal waveform is constructed as the desired noise-free signal ($N = 2048$), which is analogous to OCT spectral interferogram from a single mirror surface. Random white Gaussian noise is introduced additively. The shaded area depicted \pm S.D of the noise. In the reconstructed signal following discrete Fourier transform, the amplitude of the non-DC peak has SNR of 30 dB with respect to background S.D. The corresponding complex value of the non-DC peak is subsequently plotted in the Cartesian coordinate, Fig. 4.9(b). The simulation is repeated 10,000 times for a statistically stable solution. The process is analogous to laterally sample a homogenous region in the OCT image at a specific depth.

One can calculate the two-dimensional (2D) probability density function of the complex values from non-DC peaks. It has the form of bivariate normal distribution as discussed above. In addition, both the real and imaginary components follows univariate normal distribution. The gray solid line in Fig. 4.9(c) is the calculated pdf of the modulus from all points, r . The curve can be perfectly

fitted using Rice distribution ($R^2 > 0.99$), and the parameter ν from the fitting agrees with the modulation amplitude of the constructed sinusoidal waveform.

For comparison, the entire simulation is repeated using another sinusoid waveform with smaller modulation amplitude. The reconstructed non-DC peaks have SNR of 10 dB. In this case, the pdf of r shows a nonsymmetrical distribution (gray dashed line). Statistical-fitting against Eq. 4.11 again verifies r still follows Rice distribution, and more importantly, the retrieved parameter ν agrees with the new modulation amplitude.

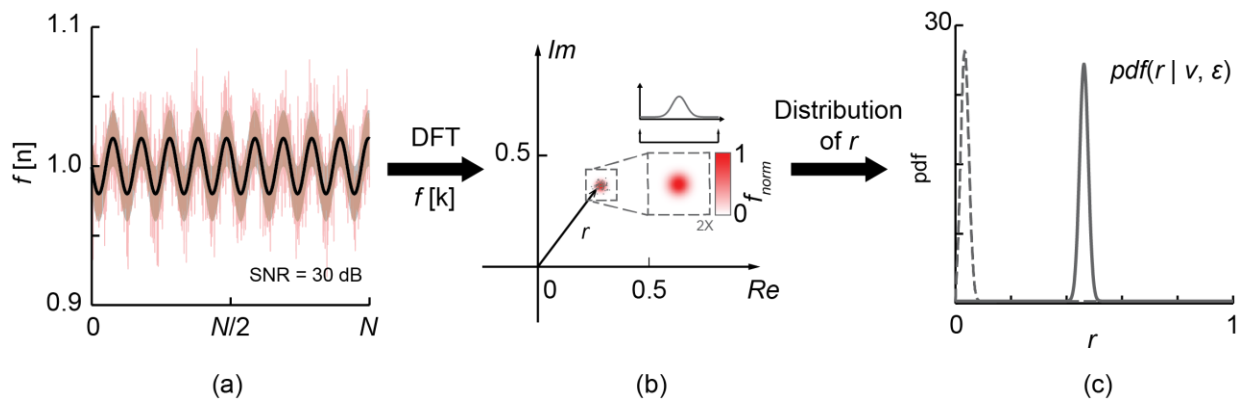


Figure 4.9 Statistical characteristics of noise in OCT. (a) Simulated interferogram with added Gaussian noise from a single reflective surface (red solid line). The black solid line is the noise free interferogram. The shaded area depicts S.D. of the added noise, which corresponds to SNR = 30 dB for the reconstructed image; (b) The distribution of the corresponding non-DC peak values on the 2D complex plane after discrete Fourier transform reconstruction. The insert shows the spatial distribution of the complex values in the 2D plane, which were tested to follow bivariate normal distribution. (c) The distribution of the modulus r . The solid line is generated using the data from (a) and (b). The dashed line showed a nonsymmetrical case where SNR was much worse (10 dB).

4.3.2.3 Verification on human vis-OCT image

Following the derivation and numerical simulation presented in section 4.3.2.2, it is established that unbiased estimation of true OCT intensity can be retrieved by statistical-fitting OCT signals within the VOI against the Rice distribution. The retrieved parameter ν represents true OCT

intensity and can be then used in subsequent oximetry analysis. The following flowchart, Fig. 4.10, summarizes the steps for retrieving true OCT intensity from human vis-OCT images.

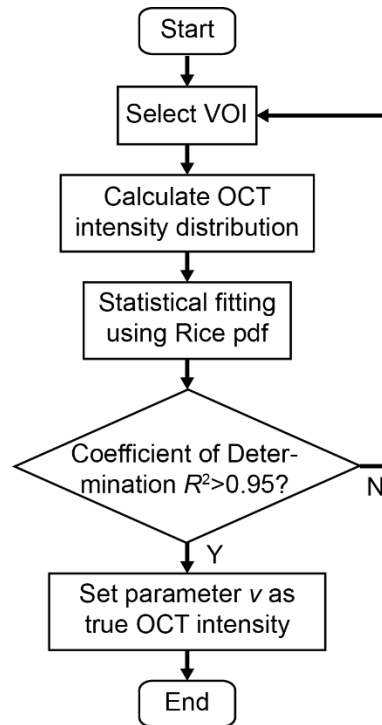


Figure 4.10 Flowchart showing the steps of retrieving true OCT intensity using statistical fitting approach. VOI: volume-of-interest. For OCT oximetry, the same VOI is used for all narrow-band images.

Figure 4.11 provides a sample on how to retrieve true OCT intensity using a moderate-quality vis-OCT image. The vessel area has regional SNR (rSNR) of ~ 5 dB, as calculated from the ratio between mean OCT intensity within the VOI and the background S.D. The background S.D. is calculated using B-scans from the same volumetric scan that do not contain any identifiable features at the given depth location. Three VOI's, one reside within the blood vessel and two from the background are assigned as indicated in Fig. 4.11(a). The corresponding OCT intensity pdf are plotted in Fig. 4.11(b) to (c) in gray solid lines. They are subsequently fitted against Rice pdf and the results are plotted in red solid lines. The coefficient of determination (R^2) are at least 0.96 for

all three scenarios. In Fig. 4.11(b), a small discrepancy can be observed between the arithmetic mean (gray arrow) and the fitted parameter ν representing true vis-OCT intensity (red arrow). Though small in this case, the improvement is non-trivial and can be significant when rSNR is worse, as is often encountered during spectroscopic analysis.

In both background areas, the arithmetic means (gray arrows) are biased even though they should be zero. However, the statistical fitting is unaffected. The retrieved parameter ν are close to zero (< 0.01) for both images.

It is worth noting that even though the statistical model is developed assuming that the added noise is independent among detector elements, it could also be applied to situations when added noise share certain correlations. Specifically, there existed cross-talk between adjacent detector elements as introduced by the limited optical resolution of the spectrometer optics. In addition, the supercontinuum laser source used in the vis-OCT system contained high levels of relative intensity noise (RIN), which had strong $1/f$ dependency. It led to the observation that A-line regions closer to the zero delay line had higher background noise. If simple arithmetic mean were used, it would appear that the region closer to the zero-delay line (box b) had higher averaged OCT intensity than the one further away from the zero-delay line (box c). However, the statistical-fitting model is unaffected by this influence. The differences in noise level manifest itself in terms of the variance of the distribution, or the width of the pdf curves plotted, which does not affect the estimated OCT intensity.

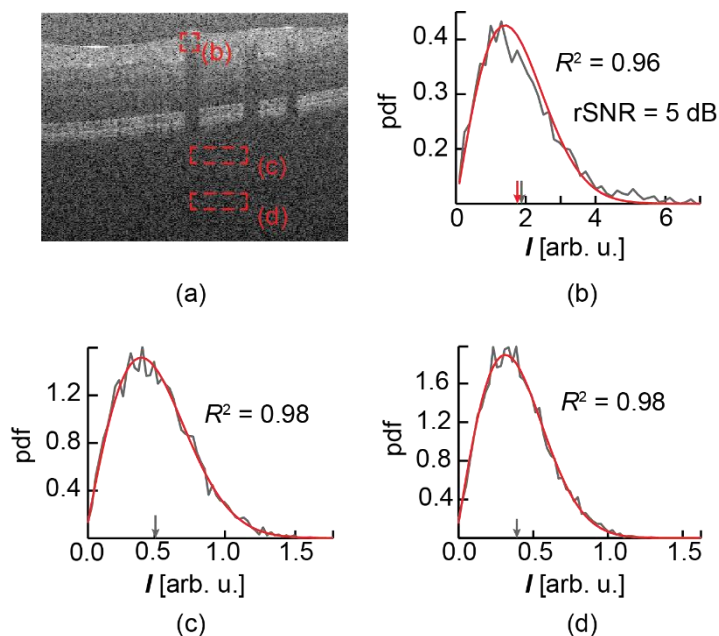


Figure 4.11 (a) A typical human vis-OCT B-scan image showing three sampling regions: one from within a blood vessel and two from the background at different depths. (b) The intensity probability density function (pdf) of OCT features (gray line) and its statistical fitting (red line). The gray and red arrows indicate the arithmetic mean and fitted OCT intensity, respectively. (c) and (d) The pdfs of pure OCT noise intensities from the background at their respective depths in gray lines. Red lines are the corresponding statistical fittings. The gray arrows indicate arithmetic means. The fitted OCT intensities are both approximately zero.

4.3.3 Vis-OCT oximetry on healthy subjects

This section presents vis-OCT retinal oximetry results obtained from four healthy volunteers. The FOV is positioned in close proximity to the optic nerve head (ONH) to visualize the first- and second- order branches of the central retinal arteries and veins. At the current stage, the selection of FOV is not related to any particular physiological or pathological conditions, but intended to test sO_2 quantification at different vascular branching levels. All images presented have FOV of $18^\circ \times 18^\circ$.

4.3.3.1 Case I

Case I includes data from a 27 year-old-female. The subject has normal vision and does not wear prescription eyeglasses. Figure 4.12(a) is a vis-OCT fundus image with FOV on the nasal side of the ONH. This is a relative high quality image, which has peak rSNR \approx 12 dB within the blood vessel. Arterioles and venules as small as 25 μ m in diameter can be visualized. In addition, the stripe patterns near the ONH correspond to NFL [135].

Vis-OCT oximetry was performed on two identified major vessels of the retinal circulation, one artery (A_1) and one vein (V_1). The retrieved OCT intensity spectra are plotted in Fig. 4.12(b) and (c), respectively. A_1 has sO_2 of 92% and V_2 has sO_2 of 77%. This represents a 16 percentage points (pp) difference between arterial and venous blood with close proximity to ONH.

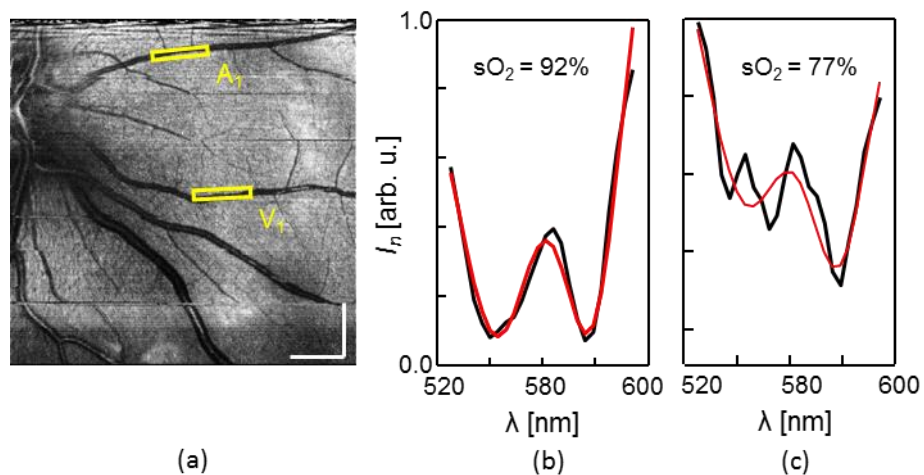


Figure 4.12 Vis-OCT image from a 27-year-old female. (a) Vis-OCT fundus image. (b) OCT intensity spectrum taken from the identified branch retinal artery (A_1 , black curve) and its least-squares fitting (red line). (c) OCT intensity spectrum taken from the identified branch retinal vein (V_1 , black curve) and its least-squares fitting (red line).

4.3.3.2 Case II

Case II includes data from a 27 year-old-male. The subject has normal vision, but wears corrective eyeglasses with a prescription of -6.00 D. Figure 4.13(a) is a vis-OCT fundus image with FOV inferotemporal to the ONH. This is also an image with relatively high quality, whose peak rSNR \approx 12 dB within the blood vessel. Smaller arterioles, venules, and the NFL strip pattern are all visible in this image.

The identified first-order branch retinal artery (A_1) has an sO_2 value of 92%. Its OCT intensity spectrum is plotted in Fig. 4.13(b). Thereafter, A_1 bifurcates into two second-order branch arteries, A_2 and A_3 . A_2 and A_3 both have lower sO_2 compared to A_1 , measured to be 90% and 89%, respectively. This spatial variation of arterial sO_2 may indicate oxygen unloading in a branch retinal artery. Though not reported in the previous literature on spatial distribution of retinal sO_2 [136, 137], these observations are consistent with Murray's law [138]. Murray's law established a predictive model between the transmural oxygen gradient and perfusion pressure gradient, which suggested that higher branch-level vessels should have greater oxygen unloading rate, or lower sO_2 values.

Similarly, two identified segment of branch retinal veins, V_1 and V_2 , have sO_2 of 75% and 73%, respectively. The OCT intensity spectra for V_1 is plotted in Fig. 4.12(c). Interestingly, as V_2 is closer to the ONH and downstream to V_1 , it also seems to have slightly higher sO_2 . It is possible that the area close to the ONH has higher regional oxygen tension due to the proximity to supplying arteries and lower photoreceptor density. Thus, higher venular sO_2 may result as unutilized oxygen molecules diffuse back into the vein [137].

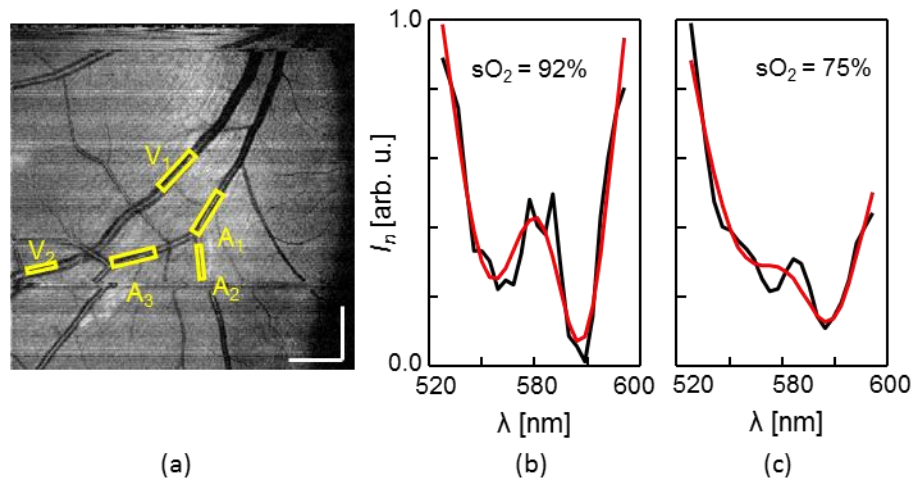


Figure 4.13 Vis-OCT image from a 27-year-old male. (a) Vis-OCT fundus image. (b) OCT intensity spectrum taken from the identified branch retinal artery (A_1 , black curve) and its least-squares fitting (red line). (c) OCT intensity spectrum taken from the identified branch retinal vein (V_1 , black curve) and its least-squares fitting (red line).

4.3.3.3 Case III

Case III includes data from a 38 year-old-female. The subject has normal vision, but wears corrective eyeglasses with a prescription of -3.75 D. Figure 4.14(a) is a vis-OCT fundus image with FOV inferior to the ONH. This image has moderate quality and has peak rSNR of 9.3 dB within the blood vessel.

Similar to the findings in Case II, three consecutive branch retinal artery segments (A_1 to A_3) show a decreasing sO_2 trend as the artery travels downstream and bifurcates. The respective sO_2 for the three identified segments are, 97% for A_1 , 94% for A_2 and 89% for A_3 . Specifically, the OCT intensity spectrum from A_1 is plotted in Fig. 4.14(b).

The identified branch retinal vein has sO_2 of 77%. Its OCT intensity spectrum is plotted in Fig. 4.14(c).

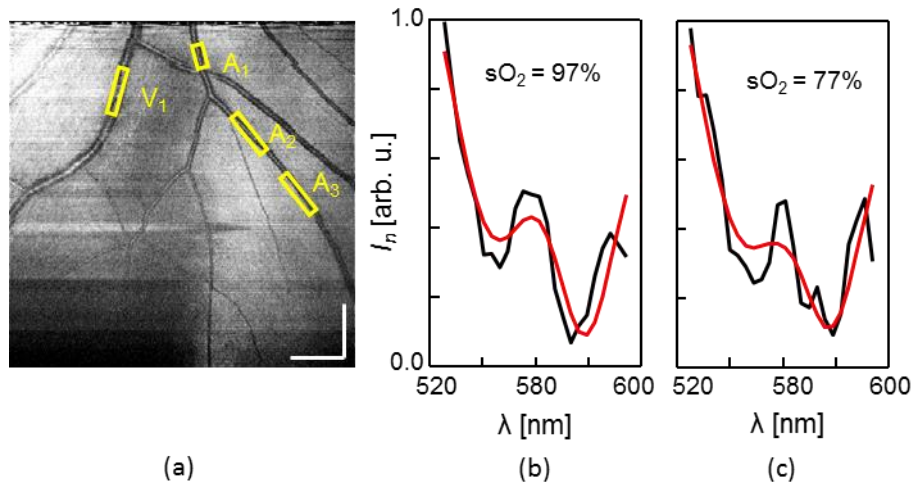


Figure 4.14 Vis-OCT image from a 38-year-old female. (a) Vis-OCT fundus image. (b) OCT intensity spectrum taken from the identified branch retinal artery (A_1 , black curve) and its least-squares fitting (red line). (c) OCT intensity spectrum taken from the identified branch retinal vein (V_1 , black curve) and its least-squares fitting (red line).

4.3.3.4 Case IV

Case IV includes data from a 60 year-old-female. The subject has minor cataracts and wears corrective eyeglass with a prescription of -3.00 D. Figure 4.14 is a vis-OCT fundus image with FOV inferotemporal to the ONH. This image has the lowest quality with peak rSNR of 8.4 dB, possibly due to extensive attenuation in the probing beam caused by age and minor cataract.

Vis-OCT oximetry was performed on two identified major retinal vessels, one artery (A_1) and one vein (V_1). The retrieved OCT intensity spectra are plotted in Fig. 4.14(b) and (c), respectively. A_1 has sO_2 of 95% and V_2 has sO_2 of 81%. This represents a 16 pp difference.

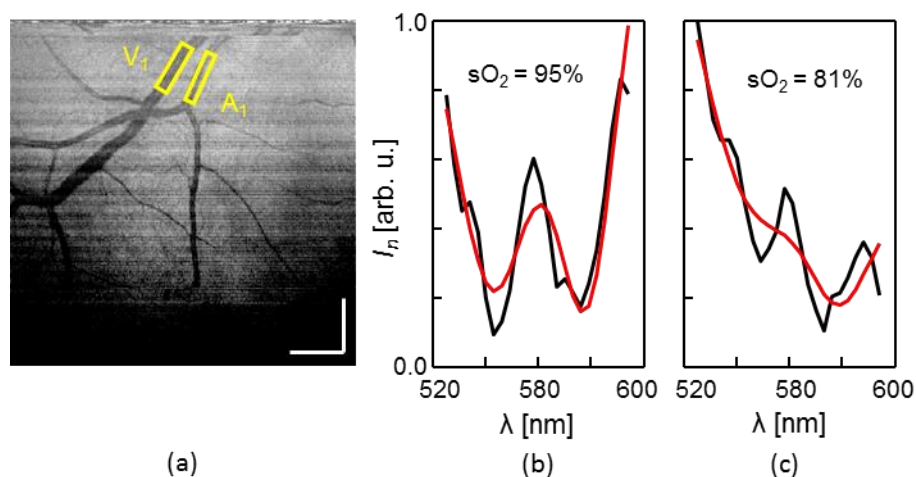


Figure 4.15 Vis-OCT image from a 60-year-old female. (a) Vis-OCT fundus image. (b) OCT intensity spectrum taken from the identified branch retinal artery (A_1 , black curve) and its least-squares fitting (red line). (c) OCT intensity spectrum taken from the identified branch retinal vein (V_1 , black curve) and its least-squares fitting (red line).

4.3.3.5 Comparison between OCT oximetry results using simple arithmetic mean and statistical fitting method

In additional to extracting retinal sO_2 from selected VOI's, it is further verified that the statistical fitting method (SF) can reduce OCT oximetry measurement error when compared to an arithmetic mean approach (AM). For each vessel branch identified in Case I to IV, the sampling VOI position and size were randomly permuted by a small amount within the vessel segment ten times. Blood sO_2 was then re-calculated using both SF and AM for each VOI. Table 4.1 summarizes the mean and S.D. of the sO_2 measurements using both methods. First, sO_2 measurement error generally increased as rSNR worsened. Second, SF sO_2 results yielded smaller errors than the corresponding AM values at all tested rSNR levels. Third, the largest measurement reduction for the SF method appeared at lower rSNR values. Specifically, when rSNR fell below 8.7 dB, SF gave us a 5 pp reduction in the error.

Table 4.1 Reduction on sO₂ measurement error ($\Delta\sigma$) using statistical fitting (SF) against arithmetic mean (AM). sO₂ values are mean \pm S.D of 10 measurements.

	Case I		Case II				
	A ₁	V ₁	A ₁	A ₂	A ₃	V ₁	V ₂
rSNR [dB]	10.5	10.7	10.4	9.7	8.7	9.4	8.7
SF sO ₂ [%]	92 \pm 3	77 \pm 4	92 \pm 4	90 \pm 5	89 \pm 4	75 \pm 5	73 \pm 5
AM sO ₂ [%]	92 \pm 5	78 \pm 6	89 \pm 7	89 \pm 9	89 \pm 9	78 \pm 8	74 \pm 10
$\Delta\sigma$ [pp]	2	2	3	4	5	3	5

Table 4.1 Continued

	Case III				Case IV	
	A ₁	A ₂	A ₃	V ₁	A ₁	V ₁
rSNR [dB]	9.3	9.1	8.1	8.9	8.4	5.5
SF sO ₂ [%]	97 \pm 3	94 \pm 3	89 \pm 4	77 \pm 5	95 \pm 4	81 \pm 6
AM sO ₂ [%]	95 \pm 5	95 \pm 5	89 \pm 7	76 \pm 8	95 \pm 7	81 \pm 11
$\Delta\sigma$ [pp]	2	2	3	3	3	5

4.4 Discussion

In this chapter, a vis-OCT imaging system for human fundus imaging was developed and demonstrated for the first time. The axial resolution of the vis-OCT images is 0.54 μ m in tissue. Using 226 μ W illumination power on the entrance pupil, the vis-OCT imaging sensitivity is about 86 dB.

Retinal images from a healthy volunteer are demonstrated with 20 $^\circ$ \times 20 $^\circ$ and 10 $^\circ$ \times 10 $^\circ$ FOV centered at both the fovea and optic nerve head. The anatomical features in vis-OCT are similar to NIR-OCT. However, due to the shorter wavelength of visible light, and the fact that the human eye is optimized to sense visible light, some discrepancies are expected. Specifically, there is less

image contrast from INL, IPL, ONL and OPL in vis-OCT images. In addition, one can observe better separation of the outer segment of photoreceptors and BM. These fine details of the anatomical structures revealed by vis-OCT may be a beneficial supplement to standard clinical NIR-OCT.

We also demonstrated sO_2 measurements within the retinal circulation from four healthy volunteers using the developed vis-OCT. Though consistent results were obtained from all subjects, it is worth noting that the measured retinal vein sO_2 is at the higher range among previously reported values [136, 137, 139, 140]. All those results were obtained by the less accurate multiple wavelength diffusive fundus imaging, which has intrinsic vulnerability due to lack of axial resolution and strong influences from vessels diameter and RPE pigmentation variations [55]. There are also a few other possible reasons that we cannot completely rule out currently. First, our sampling ROI's are close to the root of ONH. It is possible that the higher oxygen tension around ONH leads to elevated sO_2 within veins [137]. However, due to the lack of a gold standard in retinal oxygenation measurements, it is premature to draw a definitive conclusion on this discrepancy.

Second, the elevated venous sO_2 might be the result of light-retina interaction and the subsequent neural-vascular coupling. Although this does not invalidate the presented measurements, caution must be asserted when future studies are conducted on disease-induced retinal $rMRO_2$ alterations. There are two contributing factors that might lead to changes in $rMRO_2$ following vis-OCT imaging. One is that the exposure to visible light illumination during both alignment and acquisition stages mimics the effect of a flickering light excitation. It has been reported by various group that flickering light causes vasodilation in central retinal circulation and

elevated venous sO_2 [141]. The increase in sO_2 may simply indicate that a smaller fraction of oxygen is unloaded from a larger volume is supplied due to increased blood flow by reduced resistance [142]. Second, it is well known that light decreases photoreceptor metabolism [143], while oxygen metabolism in the inner retina remains unchanged [144, 145]. Interestingly though, it is also reported that retinal circulation has lower sO_2 in light than in dark, likely due to vasoconstriction induced by reduced metabolism demand [145]. However, it remains possible that these two factors combined can lead to the observed elevated venular sO_2 , caused by increased supply and diminished demand. Unfortunately, it is not possible to verify the hypothesis using the current setup and more thorough investigations are necessary. One solution is to limit the visible light illumination strictly to the duration of rapid acquisition phase, making it possible to take a snapshot of the pre-response sO_2 measurements of the retinal circulation. To achieve this goal, a NIR- and vis- dual-band OCT system similar to the one developed in chapter 2 may be useful.

Nevertheless, vis-OCT oximetry is a principally new technology and extensive studies are needed to establish its accuracy and reliability. In addition, an automated algorithm to assign ROI to retinal vessels, preferably based on image segmentation, is desirable to facilitate clinical applications in the future.

CHAPTER 5

Vis-OCT applications beyond ophthalmological imaging

Besides ophthalmic imaging applications, optical coherence tomography (OCT) has been applied to various biological research studies and clinical practices, including dermatology, cardiology, urology, dentistry, oncology, pulmonary, etc. [146].

In this chapter, a translational application is presented using the developed functional visible light OCT (vis-OCT) angiography and oximetry to monitor hemodynamic response in the mouse cortex following surgically induced ischemic stroke. Both morphological changes and cerebral circulation sO_2 are investigated before and after the stroke onset.

5.1 Introduction

Continuous cerebral circulation and sufficient oxygen supply are critical for maintaining the normal functionality of the brain [147]. During ischemic stroke (IS), impairments of the vascular network restrict the ability of brain to regulate blood supply [148]. Reduced cerebral blood flow (CBF) results in a shortage of oxygen delivery and the accumulation of toxic metabolic wastes, causing irreversible brain injury [149].

The underlying mechanisms of neuronal death in IS depend on several factors, including the severity of the ischemia, the location of neurons, and the time course along IS onset. For example, in the ischemic core, where the blood supply relies solely on the occluded vessel, excitotoxicity and acidotoxicity contribute to acute neuron necrosis. In contrast, in the penumbra region, where collateral blood flow can maintain certain cell functions, delayed neuron death may be caused by peri-infarct depolarization, oxidative and nitrative stress, inflammation, and apoptosis [149-151].

The activation of these stroke pathophysiological pathways is often associated with changes in the cerebral oxygen metabolism ($CMRO_2$). Alterations in $CMRO_2$ and neuron survivability are hypothesized to be closely related [152, 153]. Fundamental studies on such connections will shed light on how they affect and determine the destiny of neurons. Such discoveries can help to evaluate the effectiveness of treatments in terms of regulating neuron metabolism and preventing cell death, eventually benefiting IS patients.

Current techniques for monitoring $CMRO_2$ can be classified into three main categories: (1) functional magnetic resonance imaging (fMRI), (2) positron emission tomography (PET), and (3) functional optical imaging. fMRI and PET are well-established methods in functional brain imaging and the only ones that are clinically available; however, both fMRI and PET have low spatial (~ 1 mm) and temporal resolution. Moreover, the need for radioactive tracers further impedes the applications of PET.

Functional optical imaging is a collection of emerging research tools for brain hemodynamics [99, 154-157]. Among these tools, two-photon (TP) and multi-photon (MP) fluorescence microscopy have been commonly adopted in neuroscience studies due to their enhanced imaging depth into the cortex (> 1 mm) [158, 159]. Using oxygen-sensitive fluorescent dye, TP and MP

fluorescence microscopy can provide three-dimensional (3D) oxygen mapping at micrometer-scale resolution [160]. When combined with optical blood flow measurements, regional oxygen consumption can be obtained [99, 161]; however, the required extrinsic contrast agents increase the complexity of the experiment and may introduce additional confounding factors.

Meanwhile, label-free optical determination of blood oxygenation is achievable thanks to the contrasting optical absorption spectrum of oxy- and deoxy-hemoglobin. Using two or more imaging wavelengths, optical intrinsic signal (OIS) imaging and laser speckle imaging (LSI) can yield information about changes in blood oxygenation and blood flow; however, both OIS and LIS lack depth resolution and can only be applied to superficial vessels [158]. Functional photoacoustic (PA) microscopy, on the other hand, can generate 3D tomography of cortical vascular structure based solely on absorption contrast. High-definition cortical vascular network and blood oxygen saturation (sO_2) maps acquired by PA microscopy have been reported [155], yet the required mechanical coupling between the target tissue and the ultrasonic transducer poses a major challenge: such coupling cannot be guaranteed if the cranial window is sealed for long-term monitoring or if a large field-of-view is desirable.

Function optical coherence tomography (OCT) recently has emerged as a potential candidate for $CMRO_2$ monitoring. Recent advances in OCT technology have enabled hemodynamic measurements in ophthalmic applications. Notably, multiple groups have explored cortical vascular networks and cerebral circulation using OCT angiography (OCTA) [100, 162, 163]. In addition, spectroscopic OCT is intrinsically sensitive to the oxygen saturation (sO_2)-dependent hemoglobin absorption, especially when broadband visible light illumination is used [94-96]. Attempts to quantify blood sO_2 in major cortical vessels have been reported [97].

In all previous OCT and OCTA oximetry attempts, tissue scattering was either compensated for numerically or ignored completely [35, 97]; however, these approaches are inadequate when dealing with cortical tissues, which are highly optical scattering. In this chapter, a new sampling and normalization strategy is proposed. The new method takes the spectroscopic OCTA measurement at two different depth planes to minimize the adverse influences from strong wavelength-dependent tissue scattering. The corresponding theoretical formation and its implications are developed and discussed.

In this study, the hemodynamic changes on mouse cortex following acute focal ischemic stroke are investigated *in vivo* using visible-light OCT (Vis-OCT). The stroke model is induced through photothrombosis, which is favored by many researchers because the infarct size and location can be easily controlled [164-166]. By comparing functional vis-OCT angiography and oximetry results before and after photothrombosis, morphology and oxygenation variations in the cerebral circulation are characterized *in vivo* following focal ischemic stroke.

5.2 Material and Methods

5.2.1 System design

The vis-OCT cortical imaging system is adapted from the established ophthalmic setup described in earlier chapters. The main modification is that a scan lens (LSM03-VIS, Thorlabs) replaces the Keplerian telescope to focus the probing beam onto the mouse cortex. Figure 5.1 provides the schematic diagram of the modified spectral-domain vis-OCT system.

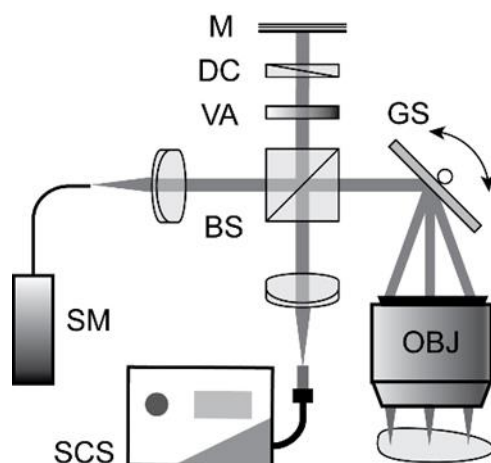


Figure 5.1 Schematic diagram of the visible-light optical coherence tomography angiographic system for imaging mouse cortex. BS: beam splitter; DC: dispersion compensator; GS: galvanometer scanning mirror; M: reference mirror; OBJ: scanning lens; SCS: supercontinuum source; SM: spectrometer; VA: variable neutral density attenuator.

The illumination spectrum centers at 566 nm with full-width-at-half-maximum (FWHM) bandwidth of 93 nm. Thus, the theoretical axial resolution is estimated to be 1.6 μm in vacuum, or 1.2 μm in mouse cortex assuming its average refractive index is around 1.37 [167]. The entrance beam diameter and the effective focal length (EFL) of the scan lens is 2.0 mm and 39 mm, respectively. This corresponds to an effective numerical aperture (NA) of 0.03, leading to 11.9 μm theoretical lateral resolution. The total irradiation intensity on the sample is set at 1.0 mW, which is measured using a calibrated power meter (Model 1918-R with 918-SL-OD2R detector, Newport Corporation).

5.2.2 Animal preparation and surgery

All experiment protocols in this study are approved by the Northwestern University Institutional Animal Care and Use Committee (IACUC). Young adult wild-type C57BL/6 mice (20 to 25 g) are used in this study. Each mouse is independently anesthetized using isoflurane/air

mixture (4% volume fraction for induction and 1.5-1.8% afterwards). The mouse is then transferred to and secured on a stereotaxic frame (World Precision Instruments). Throughout the entire procedures thereafter, the mouse core temperature is maintained at 37 °C using a homeothermic blanket system with feedback control (FHC, Stoelting).

A cranial window approximately 4×4 mm² is created to enable vis-OCT imaging. Prior to craniotomy, dexamethasone (2.0 mg/kg body weight) is injected subcutaneously to minimize cerebral edema. The fur around the surgical area is carefully removed to expose the scalp. Further local anesthesia is provided by applying lidocaine topically. Then, a midline incision is made to expose and remove soft tissues. Afterwards, the skull above the right cerebral hemisphere is thinned using a dental drill and subsequently removed. Meanwhile, caution is asserted to keep the dura intact.

If no bleeding or excessive tissue damage are present after visual inspection, a homemade steel head bar is gently attached to the exposed skull using dental cement. The head bar has a center hole of 5×6 mm² for imaging. The mouse is then transferred to an animal holder for imaging (Fig. 5.2). The head bar is also attached to the animal holder to suppress excessive motion. A pulse oximeter is attached to the rear limb of the mouse to monitor the heart rate and peripheral oxygenation (spO₂).



Figure 5.2 A mouse is secured in the animal holder ready for vis-OCT imaging. The headbar is attached to the holder to reduce motion artifacts. The headbar has a center hole of $5 \times 6 \text{ mm}^2$.

Baseline vis-OCT images are acquired if all vital signs and the condition of the exposed cortex are normal. Meanwhile, heart rate and spO_2 from the pulse oximeter are also recorded.

After initial acquisition, focal ischemic stroke is introduced through photothrombosis. Rose Bengal dye solution (40 mg/mL saline solution) is injected via tail vein at a dosage of 133 mg/kg body weight. Immediately after the injection, the exposed cortex is irradiated by 532 nm green light from a laser diode for about 30 minutes. The light spot diameter and the irradiation energy is 2.6 mm and 30 mW, respectively. After the exposure, visual inspection confirms the occlusion of major cortical vessels. In addition, vital signs are monitored through the entire photocoagulation period to ensure the mouse stays in a physiological stable stage.

Once photothrombosis is successfully induced, a second vis-OCT imaging session proceeds to investigate cortical hemodynamic response. The mouse is euthanized after imaging. A total of 15 mice were imaged. Among them, five mice underwent photothrombosis.

5.2.3 Vis-OCT angiographic protocol and angiogram

The vis-OCT scanning protocol for cortical imaging is similar to the one used in ophthalmic applications described in earlier chapters. Each B-scan location is repeated five times to generate dynamic motion contrast. One volumetric scan includes $400 \times 5 \times 512$ (# A-lines/B-scan \times # Repetition \times # B-scan locations) A-lines acquired at 50 kHz. Each individual OCT angiogram covers a square field of view (FOV) of $2 \times 2 \text{ mm}^2$. The FOV location can be laterally translated by moving the animal holding stage. A larger FOV image covering $3.2 \times 3.2 \text{ mm}^2$ is obtained by stitching smaller FOV images together.

OCT angiograms are reconstructed following the same algorithms described earlier [1, 168, 169]. Similarly, a two-step approach is employed to compensate bulk tissue motion artifacts. The first is to use image correlation to detect and correct larger movements at pixel level [170]. The second step includes using two phase modulators, the axial global phase fluctuation (AGFP) and lateral global phase fluctuation (LGFP), to compensate residue motion displacement smaller than imaging resolution [101]. After motion correction, the mean modulus of complex differential between adjacent frames is calculated at each B-scan location to yield OCT angiographic data.

For each angiographic A-line, the mean value of 15 adjoining pixels with the highest intensity is projected along the depth axis to generate *en face* angiogram of the cortex. The mean axial location of these pixels is also recorded as the depth for the corresponding vessel. The empirical choice of 15 pixels corresponds to a physical thickness of $16.2 \mu\text{m}$, which is close to the theoretical lateral resolution. Afterwards, image post-processing is performed to adjust aspect ratio of the OCT angiogram to be the same as the physical dimension of the FOV. Quantitative imaging analysis was then performed using the measurement toolbox in ImageJ.

5.2.4 Vis-OCT angiography-based oximetry

Spectroscopic OCTA analysis, which is similar to the one described in previous chapters for ophthalmic application, is performed to retrieve blood sO₂ from cerebral circulation. Briefly, the raw spectrum is split into narrow bands. Each narrow-band OCT spectrum is independently reconstructed to yield corresponding wavelength-dependent OCT angiographic contrast. The bandwidth of each narrowband has equal width of 0.23 μm⁻¹ in *k*-space, so the spectroscopic OCT angiographic also has uniform axial resolution.

Unlike ophthalmic applications, scattering from cortical tissues has strong wavelength-dependency. Thus, the back-scattered intensity spectrum cannot be simply normalized by source spectrum without introducing severe bias. To address this issue, a dual-depth sampling strategy is developed. The corresponding theoretical formulation is presented as following. The formulation neglects the finite resolution and sensitivity roll-off of a practical OCT system to simplify the expression without affecting the validity of subsequent spectral analysis. The wavelength-dependent (λ) depth-resolved (z) angiography intensity (AI) is related to the reconstructed angiography A-line (AA) following,

$$AI(z, \lambda) = [AA(z, \lambda)]^2 = I_0(\lambda)r(z, \lambda)\eta(z, \lambda)G(v), \quad (5.1)$$

where $I_0(\lambda)$ is the incidence light intensity; $r(\lambda)$ is a wavelength-dependent coefficient that characterizes the backward-scattered light that fell within the collection solid angle of the OCT detection; $G(v)$ is a non-negative scalar representing motion contrast enhancements; and v is the local velocity. $G(v)$ assumes 0 if and only if the tissue is static. We define $\eta(z, \lambda)$ as the cumulative attenuation when light double-passes the tissue

$$\eta(z, \lambda) = e^{-\int_0^z 2\mu_t(z', \lambda) dz'}, \quad (5.2)$$

where μ_t is the total attenuation coefficient of local tissue attributed to both optical absorption (μ_a) and scattering (μ_s). As scattering in biological tissue has a strong forward tendency, μ_t is estimated by reduced total attenuation coefficient, $\mu_t = \mu_a + (1 - g)\mu_s$, where g is the anisotropy factor of the scattering process.

The dual-depth sampling strategy takes two measurements at two different depth plane within each identified blood vessel. After three-dimensional (3D) threshold-based image segmentation on angiographic contrast, the lateral and axial location of each blood vessel is identified. The first sampling plane is located at the superficial surface of the vessel (Z_1). The second plane is 20 – 50 μm beneath the vessel surface (Z_2). The specific depth for Z_2 was determined by the actual vessel diameter so that it always resided within the vessel. The thickness of either plane is 10 pixels, or 11.1 μm . Thus, the analogous optical density function can be calculated by taking the nature logarithm of the ratio between the two angiography intensities from different depths,

$$\begin{aligned} OD &= \ln\left(\frac{AI(z_2, \lambda)}{AI(z_1, \lambda)}\right) = \ln\left(\frac{I_0(\lambda)r(z_2, \lambda)\eta(z_2, \lambda)G(v, z_2)}{I_0(\lambda)r(z_1, \lambda)\eta(z_1, \lambda)G(v, z_1)}\right) \\ &= \ln\left(\frac{\eta(z_2, \lambda)}{\eta(z_1, \lambda)}\right) = -2\bar{\mu}_t(\lambda)d = -2d[sO_2 \cdot \mu_{HbO_2}(\lambda) + (1 - sO_2) \cdot \mu_{Hb}(\lambda)] \end{aligned} \quad (5.3)$$

where $d = z_2 - z_1$. Because both signals originate from the blood, $r(z_2, \lambda)$ equals $r(z_1, \lambda)$ and they cancel each other in the equation. In this application, the spectrometer integration time (17 μs) and inter-frame dwell time (10 ms) guarantee that (1) the fringe washout threshold is higher than the peak cortical blood flow rate, and (2) the displacement of blood cells is fully randomized

with respect to the illumination wavelength between frames. Thus, both of the two $G(v)$ terms lose velocity dependence and cancel each other in Eq. 5.3. Even though blood flow has a parabolic profile within vessels, it had limited effects on the subsequent spectroscopic analysis. Unfortunately, the treatment implied that the blood sO_2 was homogenous within the containing vessel. Although this it is likely to be true in larger pial vessels, smaller penetrating arteriole and venules may display inhomogeneous sO_2 distribution [171]. Thus, all subsequent quantitative sO_2 analysis are restricted to major pial branches, which are also more accessible to visible-light illumination.

The vascular sO_2 map is obtained by least square fitting the retrieved spectroscopic OCT angiographic contrast using known attenuation spectra of oxy- and deoxy- hemoglobin pixel-by-pixel. It is then smoothed using a Gaussian filter about the size of system lateral resolution ($12 \mu\text{m}$) to reduce noise.

5.2.5 Quantitative fluorescence microscopy

Rose Bengal (RB) dye has a similar absorption spectrum to that of deoxyhemoglobin in the visible wavelength range, both of which are shown in Fig. 5.3. If excessive RB is present in the circulation system, it can lead to underestimation in cerebral sO_2 . Fortunately, RB has high blood clearance rate: its initial plasma concentration half-life was previously characterized to be around 2 minutes at low blood concentrations [172]. At the dosage used, the RB blood concentration should fall below the detection limit at the end of 30 minutes exposure time. Therefore, it is unlikely that the use of RB will have a significant impact on vis-OCT oximetry.

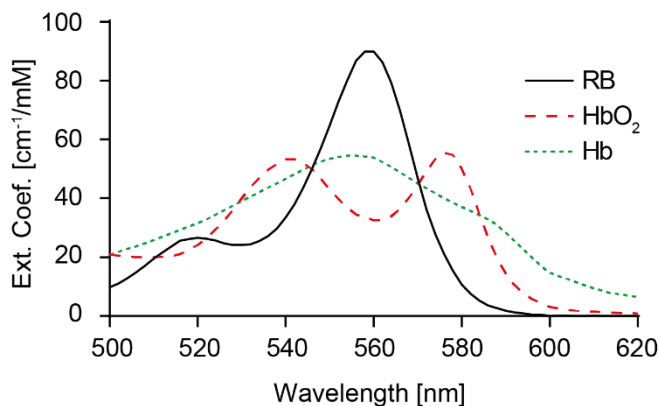


Figure 5.3 Extinction coefficient of Rose Bengal, oxygenated hemoglobin (HbO₂), and deoxygenated hemoglobin (HbR). These three chromophores have strong overlapping absorption within the wavelength range from 500 nm – 580 nm.

To verify this hypothesis, quantitative fluorescence microscopy is performed to investigate blood RB concentration after injection. The fluorescence intensity from homogenous RB solution is first calibrated against its known concentration. Then blood is drawn from tail vein at 8, 16, 24, and 32 minutes post-tail vein injection. Each blood sample is diluted 10,000 times to avoid interference from blood absorption and prevent fluorescent quenching. The measured blood RB fluorescence intensity is then compared against the calibration curve to yield blood RB concentration.

5.3 Results

5.3.1 Vis-OCT angiography

Figure 5.4 compares the depth-encoded vis-OCT angiograms before and after photothrombosis. In the pre-photothrombosis (Pre-PT) angiogram, Fig. 5.4(a), the vascular network is clearly

visualized. Most major vessels, e.g., middle cerebral artery (MCA, denoted A) and superficial pial veins (denoted V), reside close to the cortex surface, typically within 50 μm below the surface. In contrast, smaller vessel branches and capillaries dive deeper into the cortical tissue, reaching a depth of 85 μm and beyond. The revealed spatial distribution of cerebral circulation vessels agrees with the physiological arrangements reported in earlier publications [158].

In the post-photothrombosis (Post-PT) angiogram, Fig. 5.4(b), the ischemic core can be identified due to diminished dynamic motion contrast in the occluded vessels. Meanwhile, non-occluded region shows very similar vascular network as the Pre-PT image. Only minor lateral and depth variations in the vessel location can be found. This slight shift is most likely to be caused by edema and fluid accumulation that developed after vessel occlusion [165].

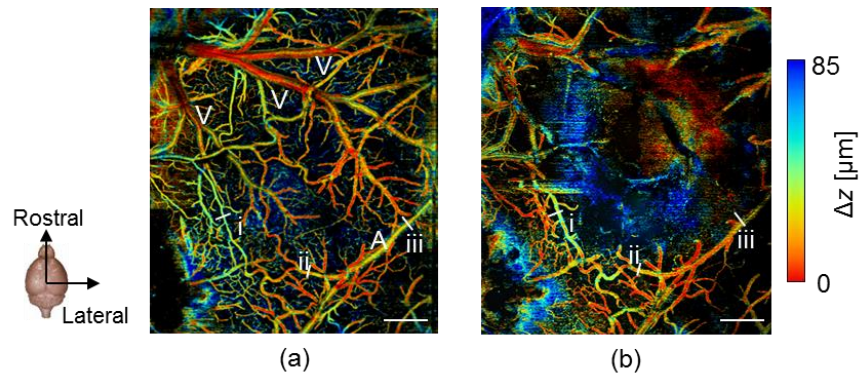


Figure 5.4 Depth-coded OCT angiograph in a mouse cortex before and after photothrombosis induced focal ischemic stroke. (a) Pre-photothrombosis (Pre-PT) microvascular structure. A: middle cerebral artery. V: superficial pial veins (b) Post-photothrombosis (Post-PT) microvascular structure. Scale bar: 500 μm .

In addition, quantitative imaging analysis reveals universal vessel dilation across the non-occluded area within the FOV. Figure 5.5 shows the cross-sectional vis-OCT angiographic vessel profile of three vessel segments, denoted i, ii, and iii in Fig. 5.4. Specifically, vessel segment ii

and iii are identified as different branches of the middle cerebral artery. The diameters of three vessel segments are determined by the FWHM of the angiographic profile.

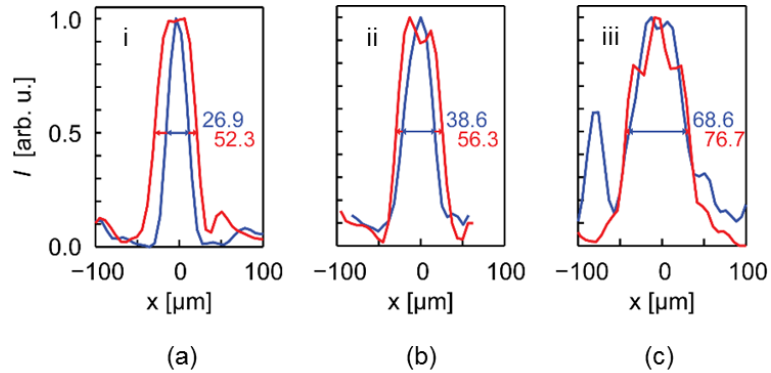


Figure 5.5 Vessel profiles measured from respective locations indicated in Fig. 5.4. (a) OCTA profile for vessel i. (b) OCTA profile for vessel ii. (c) OCTA profile for vessel iii. Blue line: pre-photothrombosis; red line: post-photothrombosis.

The observed diameter dilation for vessel i, ii, and iii are 94.4%, 45.9%, and 11.8%, respectively. Smaller vessels tend to have a larger percentage of increase in diameter. This observation agrees with previous reports on mouse cortex using the transient middle cerebral artery occlusion (tMCAO) model [173]. In that work, it is hypothesized that active vessel regulation in response to regional hypoxia challenge may have played a major role in mediating vessel dilations. In addition, Ishikawa *et al* conducted photothrombotic experiments in the rat cortex and reported similar observations [174]. In the same study, Ishikawa *et al* proposed that free radical activation, i.e., hydroxyl radicals, served as a potential vasodilator following focal photothrombosis.

3.3.2 Vis-OCT angiography-based oximetry in brain cortex

Figure 5.6 compares the wavelength-dependent OCT angiographic contrast, normalized using either source spectrum and dual-depth approach, for sO_2 calculation. The spectra are retrieved

from the identified middle cerebral artery and pial vein, respectively. In the Fig. 5.6(a), the OCTA spectra normalized by source spectrum, I_{norm} , show strong positive correlation against the increasing wavelength. In comparison, the dual-depth normalization $\frac{AI(z_2)}{AI(z_1, \lambda)}$ from the same artery and vein pair largely corrected this bias. The corrected spectrum is further compared with standard attenuation spectrum from fully oxygenated and deoxygenated blood using Beer-Lambert law [66]. The corrected spectrum agrees with the theoretical attenuation curve within the wavelength range from 520 nm to 580 nm. Especially, the arterial spectrum, due to its high oxygenation, overlaps with the theoretical spectrum of oxygenated whole blood. Meanwhile, the venous spectrum shows the combined oxy- and deoxy- whole blood spectrum shape, indicating that it is partially oxygenated. However, caution should be asserted as excessive uncorrected bias is observed for wavelengths outside the 520 nm – 580 nm range, possibly due to reduced illumination energy and thus low SNR. The data points in this range are subsequently excluded in following analysis.

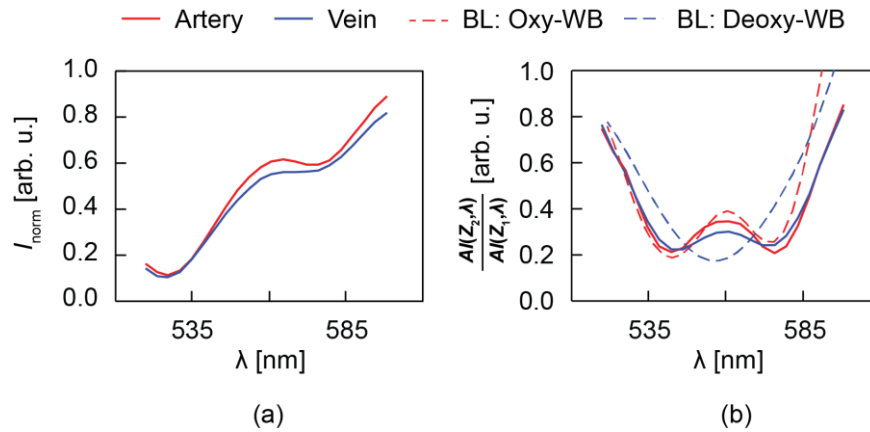


Figure 5.6 Normalized wavelength-dependent OCT angiographic contrast using different methods. (a) Normalized spectra I_{norm} using source spectrum. (b) dual-depth normalization $\frac{AI(z_2)}{AI(z_1, \lambda)}$ spectra. Dashed lines are simulated theoretical values for fully oxygenated whole blood (Oxy-WB) and fully deoxygenated whole blood (Deoxy-WB), which are calculated using Beer-Lambert law and compiled literature data for the optical properties of whole blood [66].

In addition, sO_2 are retrieved using the same least squares fitting model from both spectra. For the same artery and vein pair, the statistical distribution of measured sO_2 is plotted in Fig. 5.7. The conventional approach tends to underestimate blood sO_2 and has a wider distribution range. Figure 5.7(a) indicates it has a relatively large error margin of $89\% \pm 13\%$ and $72\% \pm 14\%$ for arterial and venous blood, respectively. On the contrary, the new dual-depth approach provides more precise and consistent sO_2 estimations. Figure 5.7(b) shows much more precise sO_2 measurement of $93\% \pm 3\%$ for the artery and $75\% \pm 6\%$ for the vein, respectively.

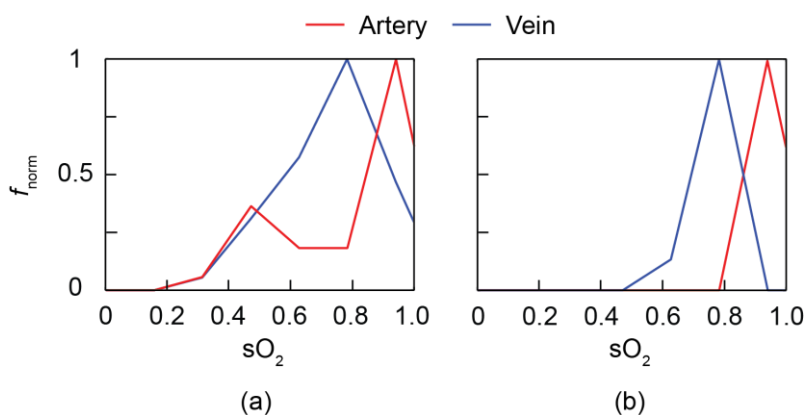


Figure 5.7 Retrieving sO_2 from conventionally normalized spectra and dual-depth method. (a) Normalized frequency (f_{norm}) of calculated sO_2 using the conventional method. (b) f_{norm} of calculated sO_2 using the new dual-depth method.

Figure 5.8 compares cerebral circulation blood sO_2 before and after photothrombosis. In the Pre-PT sO_2 map, Fig. 5.8(a), arteries and veins could be identified according to their measured sO_2 values in pseudo color. This identification agrees with previous classification based on the orientation and morphology of the cortical vessels. The mean sO_2 is subsequently calculated for various identified vessel segments. The calculation reveals that arterial sO_2 decreases as the artery travels downstream and unloads oxygen into the tissue. For example, in the first imaged branch of the middle cerebral artery (A_1), the measured sO_2 value is $93 \pm 3\%$. The value agreed with systemic oxygen saturation (spO_2) of 95% measured by the pulse oximeter. The mean sO_2 drops to $90 \pm 3\%$

in the next middle cerebral artery branch (A_2). A similar trend is also observed in veins: three branch segments of the pial vein are identified as V_1 , V_2 , and V_3 . V_1 is the largest branch and V_3 the smallest. As expected, V_3 has the lowest sO_2 of $73\pm 4\%$, while V_1 has the highest at $86\pm 8\%$. The sO_2 from the V_2 branch, $80\pm 4\%$, falls in between. Unfortunately, only averaged sO_2 can be measured in the regions where the artery and vein overlaps with each other. One such region is highlighted in the elliptic circle in Fig. 5.8(a).

In the Post-PT image, Fig 5.8(b), vascular sO_2 differentiation can no longer be appreciated. The vessels had a uniform green-blue color, indicating a mean sO_2 below 70%. The same vessel branches labeled as A_1 and A_2 had a mean sO_2 value $67\pm 7\%$ and $64\pm 6\%$, respectively.

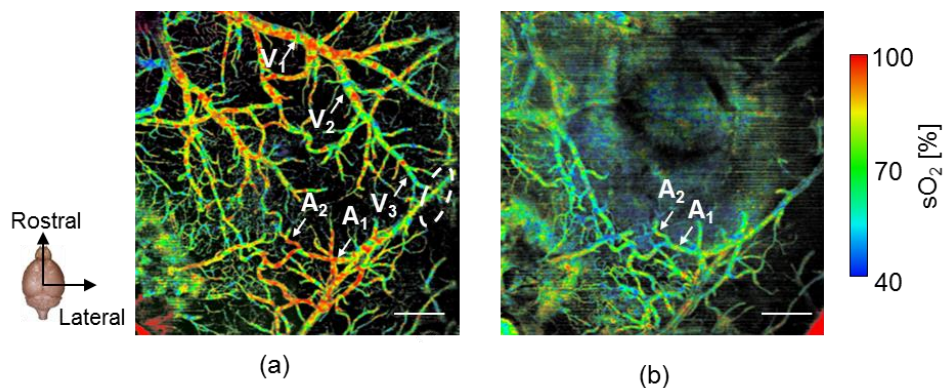


Figure 5.8 Vascular sO_2 map before and after photothrombosis induced focal ischemic stroke. (a) Before photothrombosis (Pre-PT). (b) After photothrombosis (Post-PT). Scale bar: 500 μm . Arrows indicate the vessels where mean sO_2 is calculated. Elliptical area indicates where arteries and veins overlap each other and only averaged sO_2 is displayed.

5.3.3 Quantitative measurement of blood Rose Bengal concentration

Mean fluorescence intensity of the Rose Bengal (RB) solution is plotted against its known concentration in Fig. 5.9(a). Linear regression reveals that RB fluorescence intensity forms positive

linear correlation with its concentration in dilute solution ($R^2 = 0.97$). The RB fluorescence intensity from diluted blood sample drawn from the tail vein at 8, 16, 24, and 32 minutes after RB injection is plotted on top of the calibration curve to yield blood RB concentration. Blood RB clearance curve is subsequently plotted in Fig. 5.9(b). Only trace amounts ($[RB] = 0.019$ mM, versus $[HbT] = 2.3$ mM) of RB are detected after the 24-minute mark. The results indicate that blood RB concentration was extremely low when vis-OCT is performed. Thus, it should have little impact on the aforementioned spectroscopic analysis of cerebral circulation sO_2 .

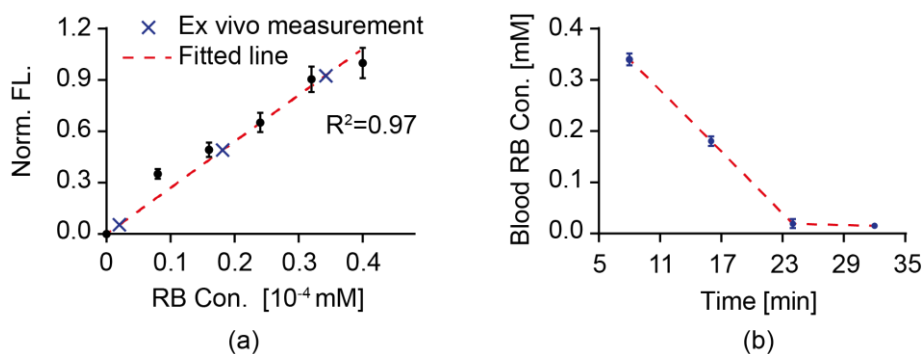


Figure 5.9 Measuring blood Rose Bengal (RB) concentration using quantitative fluorescence microscopy. (a) Calibration curve for quantitative fluorescence microscopy measurement of RB concentration. Black dots: Mean RB fluorescent intensity (FL) is plotted against known concentration of RB solution. Error bar is standard deviation (S.D) Red dashed line: linear regression of the calibration points, $R^2=0.97$. Blue cross: RB fluorescent intensity as measured in diluted blood drawn from the mouse after injection. The points are registered to the calibration curve to yield RB concentration of the solution. (b) Blood RB concentration as estimated using quantitative FL measurements at time points 8, 16, 24, and 32 minutes after intravenous RB injection.

5.4. Discussion

This chapter demonstrates one potential application of functional visible-light OCT beyond ophthalmic imaging, to monitor hemodynamic variations in the mouse cerebral circulation. A dual-

depth sampling method is used to correct excessive wavelength-dependent scattering from turbid cortical tissue. The generated full-field sO_2 map reveals spatial variation of blood oxygen content within the cerebral circulation. Similar observations were previously reported on mouse cortex using function two-photon microscopy [171], as well as in different organs [175]. Two hypotheses have been proposed [171]: (1) Arteriovenous communication pathways allow direct oxygen advection, thereby elevating venous sO_2 in larger pial branches. Though scarcely reported, such communicating pathways may exist [176]. (2) oxygen can diffuse back toward venules where tissue oxygen partial pressure is higher [177]. Unfortunately, these explanations cannot be confirmed without further investigation due to the complex and heterogeneous nature of the cerebral microvascular network.

Theoretically, spectroscopic vis-OCT angiography can provide absolute concentration of oxyhemoglobin (HbO) and deoxyhemoglobin (HbR) using optical path length measurement afforded by its 3D imaging capability. However, only the relative HbO₂ and HbR concentration, $sO_2 = \frac{[HbO_2]}{[HbO_2]+[HbR]}$, is retrieved instead due to following considerations. First, calculating absolute hemoglobin requires accurate knowledge of the path length parameter d ; however, the employment of STFT limited the axial resolution to around 11.7 μm . Given that the depth separation between two sampling locations could be as small as 20 μm in smaller vessels, measurement error in d could generate large error margin in the measurement of absolute concentration. Second, total hemoglobin concentration is unlikely to change significantly during the short imaging period, while its value can be conveniently and accurately measured from blood samples using well-established methods. In contrast, measuring local sO_2 was much more challenging and it revealed more crucial information on oxygen metabolism than absolute hemoglobin concentrations.

One drawback of the presented approach is that it is impossible to retrieve useable angiography data within the ischemic core due to lack of dynamic flow contrast. Fortunately, this implication will depend on the specific aims of different studies. In most cases, neurons in the region will inevitably undergo cell death due to severe oxygen deprivation; therefore, such measurements offer limited insight because there are no surviving cells. In contrast, the Vis-OCT angiography approach successfully retrieved hemodynamic parameters in the penumbra region, which was the primary target in most stroke studies. In the cases where the oxygen metabolism around the ischemic core needs to be measured, non-blood-flow-based method, e.g., regular structure OCT oximetry, functional two-photon fluorescence microscopy, photoacoustic microscopy, and functional magnetic resonance imaging, are more desirable.

In summary, the vis-OCT angiography and oximetry provided quantitative tools for analyzing hemodynamic response in mouse cortex. Although only demonstrated on a mouse ischemic stroke in the presented study, these tools potentially have much broader applications, such as in cancer angiogenesis and traumatic brain injury studies, where the quantification of cortical hemodynamic response is required.

CHAPTER 6

Conclusion and future work

6.1 Conclusion

The work presented in this dissertation seeks to extend the current structure-based optical coherence tomography (OCT) imaging practice towards function-based analysis. Great effort is placed upon the development and verification of OCT oximetry, which can retrieve blood hemoglobin oxygen saturation (sO_2) using intrinsic optical attenuation contrast. Blood sO_2 is a vital hemodynamic parameter as it reflects the utilization of total oxygen carrying capacity of the circulation system. If combined with blood perfusion rate, a parameter much easier to acquire, they can provide insight on oxygen metabolism rate (MRO_2) of region tissues. MRO_2 is closely associated with the activity and function of cells, and its variation is of great importance during both normal condition and pathological disease progression. Major challenges associated with OCT oximetry are outlined and addressed throughout this dissertation.

In chapter 2, we comprehensively investigated the first and foremost challenge facing OCT oximetry: is quantitative inverse calculation of blood sO_2 feasible using blood optical attenuation properties retrieved from spectroscopic OCT analysis? To address this concern, two drastically

different approaches were taken: the first was to establish a numerical model of spectroscopic OCT using the Monte Carlo method; and the other was to examine the experimental data acquired from mouse retinal circulation *in vivo*. Despite the different nature, both the numerical simulation and experimental results indicated that it was feasible to retrieve usable sO_2 -dependent blood attenuation spectrum using visible light illumination covering the hemoglobin isosbestic points around 546 nm and 570 nm. Numerical simulation suggested that OCT oximetry results was stable and independent from physiological variations such as predefined blood oxygenation and vessel diameter. In contrast, it was nearly impossible to recover sO_2 from spectroscopic OCT spectrum using near infrared (NIR) illumination, even though it included the hemoglobin isosbestic point around 797 nm. Specifically, optical scattering, rather than absorption, dominate the light attenuation process in the NIR wavelength range. In addition, optical attenuation originated from scattering is less defined and has less usable contrast for inverse calculation. This is again obvious following the calculation of blood optical properties using Mie theory in chapter 2.

Experimental results further verified our conclusion that only visible-light OCT (vis-OCT) can reliably retrieve sO_2 from mouse retinal circulation *in vivo*. In addition, we also compared imaging quality of both OCT using visible light and NIR illumination. Both Vis- and NIR-OCT images showed reasonably similar anatomical and angiographic structures when imaging the mouse retina. One notable difference is that vis-OCT offers sub-micrometer axial resolution, while NIR-OCT has larger penetration depth. Thus, vis-OCT may be advantageous when higher resolution is required to differentiate the retinal pigment epithelium (RPE) [76] or to measure nerve fiber layer (NFL) thickness [77]. Meanwhile, NIR-OCT should be used when investigating deeper layers such as choroid. Flowmetry-wise, both vis- and NIR-OCT provided reliable absolute blood flow

measurements within the retina circulation in the study. However, due to the shorter wavelength used, vis-OCT was more vulnerable to the 2- π phase-wrapping.

Once the feasibility and accuracy of OCT oximetry was demonstrated, we took one step forward to another challenge: is it possible to perform label-free sO_2 measurement on micro vessels that are generally not resolvable in conventional OCT structure images. Another related question to be answered is if there exists a workaround to avoid complicated image segmentation algorithms to isolate blood signal from surrounding tissues. Chapter 3 seeks to address these challenges by investigating OCT angiography (OCTA) based oximetry. By introducing retinal hyperoxia and hypoxia using oxygen inhalation challenge, it is demonstrated that OCT angiography oximetry is also sensitive to blood sO_2 . A theoretical formulation is presented to establish a linear correlation between the spectral derivative of wavelength-dependent OCTA and blood sO_2 . Absolute sO_2 retrieved from branch retinal arteries and veins agrees with systemic spO_2 and reported literature values, respectively. For the first time, relative sO_2 variation in the choriocapillaris is measured following oxygen challenge. Meanwhile, OCTA oximetry enables the use of narrower wavelength band, which has the potential to reduce illumination power to about one third of the currently value, greatly benefiting future clinical applications.

Following theoretical evaluation and animal experiments, the focus was placed on translating the developed vis-OCT imaging and oximetry system towards clinical applications. In chapter 4, a prototype visible-light SLO/OCT dual modality system designed for human subjects is developed. The vis-OCT prototype demonstrated similar imaging quality to commercially available NIR-OCT systems. Especially, the higher axial resolution afforded by the use of visible light enables the differentiation of RPE and Bruch's membrane. In the same chapter, a statistical

model is established to allow us to recover true OCT intensity from low signal-to-noise ratio (SNR) images. Using this approach, the accuracy and precision of OCT oximetry is improved on lower quality OCT images. It is demonstrated successfully that retinal circulation sO_2 can be retrieved from healthy subjects of both genders with an age span from 20s to 60s.

Finally, chapter 5 explores the potential of OCT oximetry beyond ophthalmic applications. We demonstrated that Vis-OCTA can be used to monitor hemodynamic variations in the cortical circulation in mouse. We developed a novel dual-depth sampling approach using OCTA to minimize the interference from strongly scattering cortical tissue. Morphological OCTA analysis reveals vasodilation following surgically induced ischemic stroke. Functional OCTA oximetry reveals spatial sO_2 variation in normal cortex as well as sO_2 disruption following stroke onset. Although only demonstrated on a mouse ischemic stroke model in the presented study, the investigating tool enabled by vis-OCT, vis-OCTA, and vis-OCT oximetry potentially have much broader applications, such as in traumatic brain injury and cancer angiogenesis and studies, where the quantification of hemodynamic response is crucial.

6.2 Future work

6.2.1 Investigating the impact of visible light illumination on retinal hemodynamic response

There are still several practical considerations unanswered before applying vis-OCT in clinical diagnosis. One major question is whether the visible laser beam will affect retinal physiology,

particularly when using vis-OCT to perform quantitative measurements such as blood flow and sO_2 . It has been found that both flow and retinal metabolism change when the retina transitions from dark adaptation to light or under flicker stimulation [178-180]; however, we do not expect such changes to occur when the retina has already been light-adapted [144, 181]. To address this concern and eliminate the potential confounding factor introduced by visible light illumination, the influence of vis-OCT acquisition on the retina metabolism must be thoroughly investigated. One potential approach is to use a vis-/NIR- dual band system similar to the one developed in chapter 2 to study hemodynamic changes, i.e. vessel diameter and flow rate following both NIR and vis-light OCT scans.

6.2.2 Angiographic-based OCT oximetry in human subjects

So far, retrieving sO_2 using vis-OCT angiography has only been demonstrated in the animal retina. Theoretically, the same algorithm should also apply to human subjects. However, there still are certain limitations preventing its implementation. First, the safety concern and increased optical attenuation associated with the human eye limits the signal intensity detected by the spectrometer. Thus, a more sensitive detector needs to be used to reduce camera integration time to achieve optimal frame rate and inter-frame dwell time suitable for OCT angiography.

Second, the visible scanning light cause considerable distraction for the subject. It is sometimes inevitable for the subject to try to follow the scanning spot, causing severe motion artifacts. Thus, integrating eye-ball tracking and a proper fixation target may help to reduce motion artifacts and provide better imaging success rate and quality.

6.2.3 Improving the functionality and hardware implementation of the vis-OCT prototype

The quantification of retinal metabolic rate of oxygen (MRO_2) is yet to be demonstrated in human subjects. In addition to blood sO_2 in the retinal circulation, blood flow rate of branch arteries and veins are required to calculate oxygen consumption using mass balance equation. It is desirable to obtain both blood sO_2 and flow using a single imaging modality, and desirably, during a single acquisition process. For example, vis-OCT flowmetry using dual-ring scanning trajectory is a good candidate to yield the information. However, its capability in human subjects is yet to be tested, especially when considering the fact that vis-OCT is more vulnerable to phase-wrapping when measuring higher flow velocity.

In addition, we seek to implement hardware-based OCT reconstructing routine to accelerate calculation of spectroscopic OCT. OCT imaging, especially spectroscopic OCT analysis, is computationally intensive due to its higher data density, and can inherently benefit from parallel computing. Thus, using hardware based calculation unit such as digital signal processor (DSP), field programmable gated array (FPGA), or graphic processing unit (GPU/CUDA), the performance of OCT and spectroscopic OCT analysis can be greatly improved. The goal is to achieve real-time display of sO_2 map, flow map and MRO_2 map over the entire field-of-view (FOV) during the imaging session.

Finally, opto-mechanical design of the vis-OCT prototype can benefit from introducing a motorized focusing lens and reference mirror to enable automated alignment, which can greatly reduce imaging time. It can reduce light exposure thus minimizing discomfort of the subject.

6.2.4 Extend the OCT intensity model to include speckles

When developing the numerical model that describes the intensity variation of OCT signal from Fourier domain systems, we ignored the effect of speckles and focused on low SNR situations. However, speckle variance is one of the major noise sources in higher quality OCT images. Speckle arises as the interference of diffusely reflected light. Unfortunately, the diffusive nature of the speckle mandates that its properties are difficult to describe using a simple formula, as it is affected by a combination of the illumination light and the microscopic structure of the sample.

As early as 1999, Schmitt *et al* explored the characteristics of speckle in OCT when imaging biological tissues [44]. They found that the OCT intensity from single polarized quasi-monochromatic illumination follows an exponential distribution. For unpolarized light, the incoherent addition of the two orthogonal components leads to a first order negative exponential distribution, which is related to Rayleigh distribution [44]. More recently, Mahmud *et al* reported in a review article on OCT speckle variance that OCT intensity follows Gaussian distribution in solid tissues, while it changes to Rayleigh distribution in fluids [182].

Following the discussion in chapter 4, we demonstrated that OCT intensity follows Rice distribution. It is worth noting that the Rice distribution approximates the Gaussian distribution when $\varepsilon \ll \nu$, or the Rayleigh distribution when $\nu \ll \varepsilon$. Thus, it is possible that a unified mathematical model can be established to describe both noises and speckle variance. Thus, it is worth extending the current OCT intensity model, which will potentially lead to better de-noising algorithms and other speckle-relevant imaging contrasts.

References

1. A. F. Fercher, W. Drexler, C. K. Hitzenberger, and T. Lasser, "Optical coherence tomography-principles and applications," *Reports on progress in physics* **66**(2), 239 (2003).
2. D. Huang, E. A. Swanson, C. P. Lin, J. S. Schuman, W. G. Stinson, W. Chang, M. R. Hee, T. Flotte, K. Gregory, C. A. Puliafito, and J.G. Fujimoto, "Optical coherence tomography," *Science* **254**(5035), 1178-1181 (1991).
3. J. G. Fujimoto and D. Huang, "Foreword: 25 Years of Optical Coherence Tomography," *Investigative Ophthalmology & Visual Science* **57**(9), OCTi-OCTii (2016).
4. A. A. Michelson and E. W. Morley, "On the relative motion of the Earth and the luminiferous ether," *American Journal of Science* **34**(203), 333-345 (1887).
5. A. F. Fercher, "Ophthalmic interferometry," in *Optics in Medicine, Biology and Environmental Research First International Conference on Optics Within Life Sciences (OWLS I), Garmisch-Partenkirchen, Germany*, 12-16 (1990).
6. C. K. Hitzenberger, "Optical measurement of the axial eye length by laser Doppler interferometry," *Investigative ophthalmology & visual science* **32**(3), 616-624 (1991).
7. A. F. Fercher, C. K. Hitzenberger, G. Kamp, and S. Y. El-Zaiat, "Measurement of intraocular distances by backscattering spectral interferometry," *Optics communications* **117**(1-2), 43-48 (1995).
8. B. Golubovic, B. E. Bouma, G. J. Tearney, and J. G. Fujimoto, "Optical frequency-domain reflectometry using rapid wavelength tuning of a Cr 4+: forsterite laser," *Opt. Lett.* **22**(22), 1704-1706 (1997).
9. W.-Y. Oh, B. J. Vakoc, M. Shishkov, G. J. Tearney, and B. E. Bouma, "> 400 kHz repetition rate wavelength-swept laser and application to high-speed optical frequency domain imaging," *Opt. Lett.* **35**(17), 2919-2921 (2010).
10. W. Wieser, B. R. Biedermann, T. Klein, C. M. Eigenwillig, and R. Huber, "Multi-Megahertz OCT: High quality 3D imaging at 20 million A-scans and 4.5 GVoxels per second," *Opt. Express* **18**(14), 14685-14704 (2010).
11. B. Potsaid, B. Baumann, D. Huang, S. Barry, A. E. Cable, J. S. Schuman, J. S. Duker, and J. G. Fujimoto, "Ultrahigh speed 1050nm swept source / Fourier domain OCT retinal and anterior segment imaging at 100,000 to 400,000 axial scans per second," *Opt. Express* **18**(19), 20029-20048 (2010).
12. M. Wolman, "Polarized light microscopy as a tool of diagnostic pathology," *Journal of Histochemistry & Cytochemistry* **23**(1), 21-50 (1975).
13. W. S. Bickel, J. Davidson, D. Huffman, and R. Kilkson, "Application of polarization effects in light scattering: a new biophysical tool," *Proceedings of the National Academy of Sciences* **73**(2), 486-490 (1976).
14. M. R. Hee, D. Huang, E. A. Swanson, and J. G. Fujimoto, "Polarization-sensitive low-coherence reflectometer for birefringence characterization and ranging," *JOSA B* **9**(6), 903-908 (1992).
15. J. F. De Boer, T. E. Milner, M. J. van Gemert, and J. S. Nelson, "Two-dimensional birefringence imaging in biological tissue by polarization-sensitive optical coherence tomography," *Opt. Lett.* **22**(12), 934-936 (1997).

16. M. Everett, K. Schoenenberger, B. Colston, and L. Da Silva, "Birefringence characterization of biological tissue by use of optical coherence tomography," *Opt. Lett.* **23**(3), 228-230 (1998).
17. K. Schoenenberger, B. W. Colston, D. J. Maitland, L. B. Da Silva, and M. J. Everett, "Mapping of birefringence and thermal damage in tissue by use of polarization-sensitive optical coherence tomography," *Applied Optics* **37**(25), 6026-6036 (1998).
18. C. K. Hitzenberger, E. Götzinger, M. Sticker, M. Pircher, and A. F. Fercher, "Measurement and imaging of birefringence and optic axis orientation by phase resolved polarization sensitive optical coherence tomography," *Opt. Express* **9**(13), 780-790 (2001).
19. S. Huard, "Polarization of light," *Polarization of Light*, by Serge Huard, pp. 348. ISBN 0-471-96536-7. Wiley-VCH, January 1997. **1**((1997)).
20. G. Yao and L. V. Wang, "Two-dimensional depth-resolved Mueller matrix characterization of biological tissue by optical coherence tomography," *Opt. Lett.* **24**(8), 537-539 (1999).
21. Y. Yasuno, S. Makita, Y. Sutoh, M. Itoh, and T. Yatagai, "Birefringence imaging of human skin by polarization-sensitive spectral interferometric optical coherence tomography," *Opt. Lett.* **27**(20), 1803-1805 (2002).
22. S. Jiao and L. V. Wang, "Two-dimensional depth-resolved Mueller matrix of biological tissue measured with double-beam polarization-sensitive optical coherence tomography," *Opt. Lett.* **27**(2), 101-103 (2002).
23. Z. Chen, T. E. Milner, D. Dave, and J. S. Nelson, "Optical Doppler tomographic imaging of fluid flow velocity in highly scattering media," *Opt. Lett.* **22**(1), 64-66 (1997).
24. J. A. Izatt, M. D. Kulkarni, S. Yazdanfar, J. K. Barton, and A. J. Welch, "In vivo bidirectional color Doppler flow imaging of picoliter blood volumes using optical coherence tomography," *Opt. Lett.* **22**(18), 1439-1441 (1997).
25. Y. Zhao, Z. Chen, C. Saxer, S. Xiang, J. F. de Boer, and J. S. Nelson, "Phase-resolved optical coherence tomography and optical Doppler tomography for imaging blood flow in human skin with fast scanning speed and high velocity sensitivity," *Opt. Lett.* **25**(2), 114-116 (2000).
26. S. Yazdanfar, A. M. Rollins, and J. A. Izatt, "Ultrahigh-velocity resolution imaging of the microcirculation in-vivo using color Doppler optical coherence tomography," in *BiOS 2001 The International Symposium on Biomedical Optics*, (International Society for Optics and Photonics, 2001), 156-164.
27. J. Ambati, B. K. Ambati, S. H. Yoo, S. Ianchulev, and A. P. Adamis, "Age-Related Macular Degeneration: Etiology, Pathogenesis, and Therapeutic Strategies," *Survey of Ophthalmology* **48**(3), 257-293 (2003).
28. U. Morgner, W. Drexler, F. Kärtner, X. Li, C. Pitris, E. Ippen, and J. Fujimoto, "Spectroscopic optical coherence tomography," *Opt. Lett.* **25**(2), 111-113 (2000).
29. R. Leitgeb, M. Wojtkowski, A. Kowalczyk, C. Hitzenberger, M. Sticker, and A. Fercher, "Spectral measurement of absorption by spectroscopic frequency-domain optical coherence tomography," *Opt. Lett.* **25**(11), 820-822 (2000).
30. D. J. Faber, E. G. Mik, M. C. G. Aalders, and T. G. van Leeuwen, "Light absorption of (oxy-)hemoglobin assessed by spectroscopic optical coherence tomography," *Opt. Lett.* **28**(16), 1436-1438 (2003).

31. D. J. Faber, E. G. Mik, M. C. G. Aalders, and T. G. van Leeuwen, "Toward assessment of blood oxygen saturation by spectroscopic optical coherence tomography," *Opt. Lett.* **30**(9), 1015-1017 (2005).
32. L. Kagemann, G. Wollstein, M. Wojtkowski, H. Ishikawa, K. A. Townsend, M. L. Gabriele, V. J. Srinivasan, J. G. Fujimoto, and J. S. Schuman, "Spectral oximetry assessed with high-speed ultra-high-resolution optical coherence tomography," *Journal of Biomedical Optics* **12**(4), 041212-041212-041218 (2007).
33. C.-W. Lu, C.-K. Lee, M.-T. Tsai, Y.-M. Wang, and C. C. Yang, "Measurement of the hemoglobin oxygen saturation level with spectroscopic spectral-domain optical coherence tomography," *Opt. Lett.* **33**(5), 416-418 (2008).
34. F. E. Robles, C. Wilson, G. Grant, and A. Wax, "Molecular imaging true-colour spectroscopic optical coherence tomography," *Nat Photon* **5**(12), 744-747 (2011).
35. J. Yi, Q. Wei, W. Liu, V. Backman, and H. F. Zhang, "Visible-light optical coherence tomography for retinal oximetry," *Opt. Lett.* **38**(11), 1796-1798 (2013).
36. B. Karamata, P. Lambelet, M. Laubscher, M. Leutenegger, S. Bourquin, and T. Lasser, "Multiple scattering in optical coherence tomography. I. Investigation and modeling," *JOSA A* **22**(7), 1369-1379 (2005).
37. B. Karamata, P. Lambelet, M. Leutenegger, M. Laubscher, S. Bourquin, and T. Lasser, "Multiple scattering in optical coherence tomography. II. Experimental and theoretical investigation of cross talk in wide-field optical coherence tomography," *JOSA A* **22**(7), 1380-1388 (2005).
38. R. K. Wang, "Signal degradation by multiple scattering in optical coherence tomography of dense tissue: a Monte Carlo study towards optical clearing of biotissues," *Physics in medicine and biology* **47**(13), 2281 (2002).
39. L. Thrane, H. T. Yura, and P. E. Andersen, "Analysis of optical coherence tomography systems based on the extended Huygens–Fresnel principle," *JOSA A* **17**(3), 484-490 (2000).
40. L. Liu, J. A. Gardecki, S. K. Nadkarni, J. D. Toussaint, Y. Yagi, B. E. Bouma, and G. J. Tearney, "Imaging the subcellular structure of human coronary atherosclerosis using micro-optical coherence tomography," *Nature medicine* **17**(8), 1010-1014 (2011).
41. F. Robles, R. N. Graf, and A. Wax, "Dual window method for processing spectroscopic optical coherence tomography signals with simultaneously high spectral and temporal resolution," *Opt. Express* **17**(8), 6799-6812 (2009).
42. R. Leitgeb, C. Hitzenberger, and A. F. Fercher, "Performance of fourier domain vs. time domain optical coherence tomography," *Opt. Express* **11**(8), 889-894 (2003).
43. M. A. Choma, M. V. Sarunic, C. Yang, and J. A. Izatt, "Sensitivity advantage of swept source and Fourier domain optical coherence tomography," *Opt. Express* **11**(18), 2183-2189 (2003).
44. J. M. Schmitt, S. H. Xiang, and K. M. Yung, "Speckle in Optical Coherence Tomography," *Journal of Biomedical Optics* **4**(1), 95-105 (1999).
45. J. G. Fujimoto, "Optical coherence tomography for ultrahigh resolution in vivo imaging," *Nat Biotech* **21**(11), 1361-1367 (2003).
46. A. M. Zysk, F. T. Nguyen, A. L. Oldenburg, D. L. Marks, and S. A. Boppart, "Optical coherence tomography: a review of clinical development from bench to bedside," *Journal of Biomedical Optics* **12**(5), 051403-051403-051421 (2007).

47. J. M. Schmitt, "Optical coherence tomography (OCT): a review," *Selected Topics in Quantum Electronics*, IEEE Journal of **5**(4), 1205-1215 (1999).
48. D. J. Faber and T. G. van Leeuwen, "Are quantitative attenuation measurements of blood by optical coherence tomography feasible?," *Opt. Lett.* **34**(9), 1435-1437 (2009).
49. S. Prahl, "Optical absorption of hemoglobin," Oregon Medical Laser Center, <http://omlc.ogi.edu/spectra/hemoglobin/index.html> **15**((1999)).
50. B. Povazay, A. A. Apolonski, A. Unterhuber, B. Hermann, K. K. Bizheva, H. Sattmann, P. S. J. Russell, F. Krausz, A. F. Fercher, and W. Drexler, "Visible light optical coherence tomography," in *International Symposium on Biomedical Optics*. International Society for Optics and Photonics 90-94 (2002).
51. L. Wang, S. L. Jacques, and L. Zheng, "MCML—Monte Carlo modeling of light transport in multi-layered tissues," *Computer methods and programs in biomedicine* **47**(2), 131-146 (1995).
52. G. Yao and L. V. Wang, "Monte Carlo simulation of an optical coherence tomography signal in homogeneous turbid media," *Physics in medicine and biology* **44**(9), 2307 (1999).
53. A. Tycho, T. M. Jørgensen, H. T. Yura, and P. E. Andersen, "Derivation of a Monte Carlo method for modeling heterodyne detection in optical coherence tomography systems," *Applied optics* **41**(31), 6676-6691 (2002).
54. M. Hammer, S. Leistriz, L. Leistriz, and D. Schweitzer, "Light paths in retinal vessel oximetry," *IEEE Transactions on Biomedical Engineering* **48**(5), 592-598 (2001).
55. W. Liu, S. Jiao, and H. F. Zhang, "Accuracy of retinal oximetry: a Monte Carlo investigation," *Journal of biomedical optics* **18**(6), 066003-066003 (2013).
56. C. E. Riva, J. E. Grunwald, S. H. Sinclair, and B. Petrig, "Blood velocity and volumetric flow rate in human retinal vessels," *Investigative ophthalmology & visual science* **26**(8), 1124-1132 (1985).
57. M. Ritt and R. E. Schmieder, "Wall-to-lumen ratio of retinal arterioles as a tool to assess vascular changes," *Hypertension* **54**(2), 384-387 (2009).
58. C. W. Oyster, "The human eye," Sunderland, MA: Sinauer (1999).
59. M. Keijzer, R. R. Richards-Kortum, S. L. Jacques, and M. S. Feld, "Fluorescence spectroscopy of turbid media: autofluorescence of the human aorta," *Applied Optics* **28**(20), 4286-4292 (1989).
60. M. Hammer, A. Roggan, D. Schweitzer, and G. Muller, "Optical properties of ocular fundus tissues-an in vitro study using the double-integrating-sphere technique and inverse Monte Carlo simulation," *Physics in medicine and biology* **40**(6), 963 (1995).
61. S. Prahl, "Tabulated molar extinction coefficient for hemoglobin in water," Oregon Medical Laser Center (1998).
62. A. Geirsdottir, O. Palsson, S. H. Hardarson, O. B. Olafsdottir, J. V. Kristjansdottir, and E. Stefánsson, "Retinal Vessel Oxygen Saturation in Healthy Individuals Retinal Vessel Oxygen Saturation," *Investigative ophthalmology & visual science* **53**(9), 5433-5442 (2012).
63. D. J. Faber, M. C. Aalders, E. G. Mik, B. A. Hooper, M. J. van Gemert, and T. G. van Leeuwen, "Oxygen saturation-dependent absorption and scattering of blood," *Physical review letters* **93**(2), 028102 (2004).

64. A. Roggan, M. Friebel, K. Dörschel, A. Hahn, and G. Muller, "Optical properties of circulating human blood in the wavelength range 400-2500 nm," *Journal of biomedical optics* **4**(1), 36-46 (1999).
65. D. Sardar and L. Levy, "Optical properties of whole blood," *Lasers in medical science* **13**(2), 106-111 (1998).
66. N. Bosschaart, G. J. Edelman, M. C. G. Aalders, T. G. van Leeuwen, and D. J. Faber, "A literature review and novel theoretical approach on the optical properties of whole blood," *Lasers in Medical Science* **29**(2), 453-479 (2014).
67. Q. Lu, X. Gan, M. Gu, and Q. Luo, "Monte Carlo modeling of optical coherence tomography imaging through turbid media," *Applied optics* **43**(8), 1628-1637 (2004).
68. J. D. Rogers, İ. R. Çapoğlu, and V. Backman, "Nonscalar elastic light scattering from continuous media in the Born approximation: erratum," *Opt. Lett.* **35**(9), 1367-1367 (2010).
69. J. Yi and V. Backman, "Imaging a full set of optical scattering properties of biological tissue by inverse spectroscopic optical coherence tomography," *Opt. Lett.* **37**(21), 4443-4445 (2012).
70. D. J. Faber, F. J. van der Meer, M. C. Aalders, and T. G. van Leeuwen, "Hematocrit-dependence of the scattering coefficient of blood determined by optical coherence tomography," in *Saratov Fall Meeting 2005: Optical Technologies in Biophysics and Medicine VII*, (International Society for Optics and Photonics, 2006), 61630Y-61630Y-61639.
71. A. Harris, R. B. Dinn, L. Kagemann, and E. Rechtman, "A review of methods for human retinal oximetry," *Ophthalmic Surgery, Lasers and Imaging Retina* **34**(2), 152-164 (2003).
72. L. Pedersen, M. Grunkin, B. Ersbøll, K. Madsen, M. Larsen, N. Christoffersen, and U. Skands, "Quantitative measurement of changes in retinal vessel diameter in ocular fundus images," *Pattern Recognition Letters* **21**(13), 1215-1223 (2000).
73. Y. Wang, B. A. Bower, J. A. Izatt, O. Tan, and D. Huang, "Retinal blood flow measurement by circumpapillary Fourier domain Doppler optical coherence tomography," *Journal of Biomedical Optics* **13**(6), 064003-064003-064009 (2008).
74. D. C. Ghiglia and M. D. Pritt, *Two-dimensional phase unwrapping: theory, algorithms, and software* (Wiley New York:, 1998), Vol. 4.
75. S. Chen, J. Yi, W. Liu, V. Backman, and H. F. Zhang, "Monte Carlo Investigation of Optical Coherence Tomography Retinal Oximetry," *Biomedical Engineering, IEEE Transactions on* **62**(9), 2308-2315 (2015).
76. X. Shu, W. Liu, and H. F. Zhang, "Monte Carlo investigation on quantifying the retinal pigment epithelium melanin concentration by photoacoustic ophthalmoscopy," *Journal of biomedical optics* **20**(10), 106005-106005 (2015).
77. S. Liu, B. Wang, B. Yin, T. E. Milner, M. K. Markey, S. J. McKinnon, and H. G. Rylander, "Retinal nerve fiber layer reflectance for early glaucoma diagnosis," *Journal of glaucoma* **23**(1), 10.1097/IJG.1090b1013e31829ea31822a31827 (2014).
78. H. Li, W. Liu, and H. F. Zhang, "Investigating the influence of chromatic aberration and optical illumination bandwidth on fundus imaging in rats," *Journal of Biomedical Optics* **20**(10), 106010-106010 (2015).
79. B. White, M. Pierce, N. Nassif, B. Cense, B. Park, G. Tearney, B. Bouma, T. Chen, and J. de Boer, "In vivo dynamic human retinal blood flow imaging using ultra-high-speed spectral domain optical coherence tomography," *Opt. Express* **11**(25), 3490-3497 (2003).

80. Y. Wang, B. A. Bower, J. A. Izatt, O. Tan, and D. Huang, "In vivo total retinal blood flow measurement by Fourier domain Doppler optical coherence tomography," *Journal of biomedical optics* **12**(4), 041215-041215-041218 (2007).
81. B. Baumann, B. Potsaid, M. F. Kraus, J. J. Liu, D. Huang, J. Hornegger, A. E. Cable, J. S. Duker, and J. G. Fujimoto, "Total retinal blood flow measurement with ultrahigh speed swept source/Fourier domain OCT," *Biomed. Opt. Express* **2**(6), 1539-1552 (2011).
82. Z. Zhi, X. Yin, S. Dziennis, T. Wietecha, K. L. Hudkins, C. E. Alpers, and R. K. Wang, "Optical microangiography of retina and choroid and measurement of total retinal bloodflow in mice," *Biomed. Opt. Express* **3**(11), 2976-2986 (2012).
83. Z. Zhi, W. Cepurna, E. Johnson, T. Shen, J. Morrison, and R. K. Wang, "Volumetric and quantitative imaging of retinal blood flow in rats with optical microangiography," *Biomed. Opt. Express* **2**(3), 579-591 (2011).
84. R. M. Werkmeister, N. Dragostinoff, S. Palkovits, R. Told, A. Boltz, R. A. Leitgeb, M. Gröschl, G. Garhöfer, and L. Schmetterer, "Measurement of Absolute Blood Flow Velocity and Blood Flow in the Human Retina by Dual-Beam Bidirectional Doppler Fourier-Domain Optical Coherence Tomography," *Investigative Ophthalmology & Visual Science* **53**(10), 6062-6071 (2012).
85. C. Dai, X. Liu, H. F. Zhang, C. A. Puliafito, and S. Jiao, "Absolute Retinal Blood Flow Measurement With a Dual-Beam Doppler Optical Coherence Tomography," *Investigative Ophthalmology & Visual Science* **54**(13), 7998-8003 (2013).
86. L. An and R. K. Wang, "In vivo volumetric imaging of vascular perfusion within human retina and choroids with optical micro-angiography," *Opt. Express* **16**(15), 11438-11452 (2008).
87. Y. Jia, O. Tan, J. Tokayer, B. Potsaid, Y. Wang, J. J. Liu, M. F. Kraus, H. Subhash, J. G. Fujimoto, J. Hornegger, and D. Huang, "Split-spectrum amplitude-decorrelation angiography with optical coherence tomography," *Opt. Express* **20**(4), 4710-4725 (2012).
88. D. Y. Kim, J. Fingler, R. J. Zawadzki, S. S. Park, L. S. Morse, D. M. Schwartz, S. E. Fraser, and J. S. Werner, "Optical imaging of the chorioretinal vasculature in the living human eye," *Proceedings of the National Academy of Sciences of the United States of America* **110**(35), 14354-14359 (2013).
89. Y. Wang, A. A. Fawzi, R. Varma, A. A. Sadun, X. Zhang, O. Tan, J. A. Izatt, and D. Huang, "Pilot Study of Optical Coherence Tomography Measurement of Retinal Blood Flow in Retinal and Optic Nerve Diseases," *Investigative Ophthalmology & Visual Science* **52**(2), 840-845 (2011).
90. Y. Jia, S. T. Bailey, D. J. Wilson, O. Tan, M. L. Klein, C. J. Flaxel, B. Potsaid, J. J. Liu, C. D. Lu, M. F. Kraus, J. G. Fujimoto, and D. Huang, "Quantitative Optical Coherence Tomography Angiography of Choroidal Neovascularization in Age-Related Macular Degeneration," *Ophthalmology* **121**(7), 1435-1444 (2014).
91. S. Srinivas, O. Tan, S. Wu, M. G. Nittala, D. Huang, R. Varma, and S. R. Sadda, "Doppler Fourier-domain optical coherence tomography measured Retinal blood flow in Chinese American adults: The Chinese American Eye Study," *Invest. Ophthalmol. Vis. Sci.* **55**(5), 214- (2014).
92. W. Song, Q. Wei, W. Liu, T. Liu, J. Yi, N. Sheibani, A. A. Fawzi, R. A. Linsenmeier, S. Jiao, and H. F. Zhang, "A combined method to quantify the retinal metabolic rate of oxygen

- using photoacoustic ophthalmoscopy and optical coherence tomography," *Scientific reports* **4**(6525) (2014).
93. J. Yao, K. I. Maslov, Y. Zhang, Y. Xia, and L. V. Wang, "Label-free oxygen-metabolic photoacoustic microscopy in vivo," *Journal of Biomedical Optics* **16**(7), 076003-076003-076011 (2011).
 94. F. E. Robles, S. Chowdhury, and A. Wax, "Assessing hemoglobin concentration using spectroscopic optical coherence tomography for feasibility of tissue diagnostics," *Biomed. Opt. Express* **1**(1), 310-317 (2010).
 95. J. Yi and X. Li, "Estimation of oxygen saturation from erythrocytes by high-resolution spectroscopic optical coherence tomography," *Opt. Lett.* **35**(12), 2094-2096 (2010).
 96. J. Yi, S. Chen, V. Backman, and H. F. Zhang, "In vivo functional microangiography by visible-light optical coherence tomography," *Biomed. Opt. Express* **5**(10), 3603-3612 (2014).
 97. S. P. Chong, C. W. Merkle, C. Leahy, H. Radhakrishnan, and V. J. Srinivasan, "Quantitative microvascular hemoglobin mapping using visible light spectroscopic Optical Coherence Tomography," *Biomed. Opt. Express* **6**(4), 1429-1450 (2015).
 98. J. D. Rogers, A. J. Radosevich, Y. Ji, and V. Backman, "Modeling Light Scattering in Tissue as Continuous Random Media Using a Versatile Refractive Index Correlation Function," *Selected Topics in Quantum Electronics, IEEE Journal of* **20**(2), 173-186 (2014).
 99. A. K. Dunn, H. Bolay, M. A. Moskowitz, and D. A. Boas, "Dynamic Imaging of Cerebral Blood Flow Using Laser Speckle," *Journal of Cerebral Blood Flow & Metabolism* **21**(3), 195-201 (2001).
 100. V. J. Srinivasan, J. Y. Jiang, M. A. Yaseen, H. Radhakrishnan, W. Wu, S. Barry, A. E. Cable, and D. A. Boas, "Rapid volumetric angiography of cortical microvasculature with optical coherence tomography," *Opt. Lett.* **35**(1), 43-45 (2010).
 101. J. Lee, V. Srinivasan, H. Radhakrishnan, and D. A. Boas, "Motion correction for phase-resolved dynamic optical coherence tomography imaging of rodent cerebral cortex," *Opt. Express* **19**(22), 21258-21270 (2011).
 102. O. Akça, A. G. Doufas, N. Morioka, S. Iscoe, J. Fisher, and D. I. Sessler, "Hypercapnia improves tissue oxygenation," *Anesthesiology* **97**(4), 801-806 (2002).
 103. G. T. Dorner, G. Garhofer, C. Zawinka, B. Kiss, and L. Schmetterer, "Response of retinal blood flow to CO₂-breathing in humans," *Eur J Ophthalmol* **12**(6), 459-466 (2002).
 104. N. D. Wangsa-Wirawan and R. A. Linsenmeier, "Retinal oxygen: Fundamental and clinical aspects," *Archives of Ophthalmology* **121**(4), 547-557 (2003).
 105. A. Alm and A. Bill, "Blood Flow and Oxygen Extraction in the Cat Uvea at Normal and High Intraocular Pressures," *Acta Physiologica Scandinavica* **80**(1), 19-28 (1970).
 106. L. Wang, P. TÖRNquist, and A. Bill, "Glucose metabolism in pig outer retina in light and darkness," *Acta Physiologica Scandinavica* **160**(1), 75-81 (1997).
 107. R. Simó, C. Hernández, and E. C. f. t. E. T. o. D. Retinopathy, "Neurodegeneration is an early event in diabetic retinopathy: therapeutic implications," *British Journal of Ophthalmology*, bjophthalmol-2012-302005 (2012).
 108. C. M. Jørgensen, S. H. Hardarson, and T. Bek, "The oxygen saturation in retinal vessels from diabetic patients depends on the severity and type of vision - threatening retinopathy," *Acta ophthalmologica* **92**(1), 34-39 (2014).

109. C. Jørgensen and T. Bek, "Increasing Oxygen Saturation in Larger Retinal Vessels After Photocoagulation for Diabetic Retinopathy," *Investigative ophthalmology & visual science* **55**(8), 5365-5369 (2014).
110. S. H. Hardarson and E. Stefánsson, "Retinal oxygen saturation is altered in diabetic retinopathy," *British journal of ophthalmology* **96**(4), 560-563 (2012).
111. M. Hammer, W. Vilser, T. Riemer, A. Mandecka, D. Schweitzer, U. Kühn, J. Dawczynski, F. Liemt, and J. Strobel, "Diabetic patients with retinopathy show increased retinal venous oxygen saturation," *Graefe's Archive for Clinical and Experimental Ophthalmology* **247**(8), 1025-1030 (2009).
112. J. C. Lau and R. A. Linsenmeier, "Increased intraretinal PO₂ in short-term diabetic rats," *Diabetes* **63**(12), 4338-4342 (2014).
113. D.-Y. Yu and S. J. Cringle, "Retinal degeneration and local oxygen metabolism," *Experimental eye research* **80**(6), 745-751 (2005).
114. T. Kurihara, P. D. Westenskow, M. L. Gantner, Y. Usui, A. Schultz, S. Bravo, E. Aguilar, C. Wittgrove, M. S. Friedlander, and L. P. Paris, "Hypoxia-induced metabolic stress in retinal pigment epithelial cells is sufficient to induce photoreceptor degeneration," *Elife* **5**(e14319) (2016).
115. W. Soliman, M. Vinten, B. Sander, K. A. E. N. Soliman, S. Yehya, M. S. A. Rahman, and M. Larsen, "Optical coherence tomography and vessel diameter changes after intravitreal bevacizumab in diabetic macular oedema," *Acta ophthalmologica* **86**(4), 365-371 (2008).
116. E. Stefansson, M. Landers 3rd, and M. Wolbarsht, "Increased retinal oxygen supply following pan-retinal photocoagulation and vitrectomy and lensectomy," *Transactions of the American Ophthalmological Society* **79**(307) (1981).
117. N. M. Holekamp, Y.-B. Shui, and D. Beebe, "Lower intraocular oxygen tension in diabetic patients: possible contribution to decreased incidence of nuclear sclerotic cataract," *American journal of ophthalmology* **141**(6), 1027-1032 (2006).
118. R. A. Linsenmeier and R. Braun, "Oxygen distribution and consumption in the cat retina during normoxia and hypoxemia," *The Journal of general physiology* **99**(2), 177-197 (1992).
119. B. A. Berkowitz, C. McDonald, Y. Ito, P. S. Tofts, Z. Latif, and J. Gross, "Measuring the human retinal oxygenation response to a hyperoxic challenge using MRI: eliminating blinking artifacts and demonstrating proof of concept," *Magnetic resonance in medicine* **46**(2), 412-416 (2001).
120. Y. Ito and B. A. Berkowitz, "MR studies of retinal oxygenation," *Vision research* **41**(10), 1307-1311 (2001).
121. O. S. Finikova, A. Y. Lebedev, A. Aprelev, T. Troxler, F. Gao, C. Garnacho, S. Muro, R. M. Hochstrasser, and S. A. Vinogradov, "Oxygen microscopy by two - photon - excited phosphorescence," *ChemPhysChem* **9**(12), 1673-1679 (2008).
122. R. D. Shonat and A. C. Kight, "Oxygen tension imaging in the mouse retina," *Annals of biomedical engineering* **31**(9), 1084-1096 (2003).
123. J. V. Kristjansdottir, S. H. Hardarson, G. H. Halldorsson, R. A. Karlsson, T. S. Eliasdottir, and E. Stefánsson, "Retinal Oximetry With a Scanning Laser Ophthalmoscope," *Investigative ophthalmology & visual science* **55**(5), 3120-3126 (2014).

124. D. Mordant, I. Al-Abboud, G. Muyo, A. Gorman, A. Harvey, and A. McNaught, "Oxygen saturation measurements of the retinal vasculature in treated asymmetrical primary open-angle glaucoma using hyperspectral imaging," *Eye* **28**(10), 1190-1200 (2014).
125. H. Li, W. Liu, B. Dong, J. V. Kaluzny, A. A. Fawzi, and H. F. Zhang, "Snapshot hyperspectral retinal imaging using compact spectral resolving detector array," *Journal of Biophotonics* (2016).
126. L. V. Wang and S. Hu, "Photoacoustic tomography: in vivo imaging from organelles to organs," *Science* **335**(6075), 1458-1462 (2012).
127. L. J. Steven, "Optical properties of biological tissues: a review," *Physics in Medicine and Biology* **58**(11), R37 (2013).
128. S. Chen, X. Shu, J. Yi, A. Fawzi, and H. F. Zhang, "Dual-band optical coherence tomography using a single supercontinuum laser source," *Journal of Biomedical Optics* **21**(6), 066013-066013 (2016).
129. J. Yi, W. Liu, S. Chen, V. Backman, N. Sheibani, C. M. Sorenson, A. A. Fawzi, R. A. Linsenmeier, and H. F. Zhang, "Visible light optical coherence tomography measures retinal oxygen metabolic response to systemic oxygenation," *Light: Science & Applications* **4**(9), e334 (2015).
130. B. T. Soetikno, J. Yi, R. Shah, W. Liu, P. Purta, H. F. Zhang, and A. A. Fawzi, "Inner retinal oxygen metabolism in the 50/10 oxygen-induced retinopathy model," *Scientific reports* **5**((2015).
131. M. Adhi and J. S. Duker, "Optical coherence tomography—current and future applications," *Current opinion in ophthalmology* **24**(3), 213 (2013).
132. W. L. Ji Yi, Siyu Chen, Vadim Backman, Nader Sheibani, Christine M. Sorenson, Amani Fawzi, Robert Linsenmeier, and Hao F. Zhang, "Visible light optical coherence tomography measures retinal oxygen metabolic response to systemic oxygenation," *Light: Science and applications* **In press**((2015).
133. F. C. Delori, R. H. Webb, and D. H. Sliney, "Maximum permissible exposures for ocular safety (ANSI 2000), with emphasis on ophthalmic devices," *JOSA A* **24**(5), 1250-1265 (2007).
134. R. C. Gonzalez, R. E. Woods, and S. L. Eddins, *Digital image processing using MATLAB* (Pearson Education India, 2004).
135. J. Yi, S. Chen, X. Shu, A. A. Fawzi, and H. F. Zhang, "Human retinal imaging using visible-light optical coherence tomography guided by scanning laser ophthalmoscopy," *Biomed. Opt. Express* **6**(10), 3701-3713 (2015).
136. D. J. Mordant, I. Al-Abboud, G. Muyo, A. Gorman, A. Sallam, P. Ritchie, A. R. Harvey, and A. I. McNaught, "Spectral imaging of the retina," *Eye* **25**(3), 309-320 (2011).
137. A. M. Shahidi, S. R. Patel, J. G. Flanagan, and C. Hudson, "Regional variation in human retinal vessel oxygen saturation," *Experimental Eye Research* **113**(143-147 (2013).
138. C. D. Murray, "The Physiological Principle of Minimum Work II. Oxygen Exchange in Capillaries," *Proceedings of the National Academy of Sciences* **12**(5), 299-304 (1926).
139. D. Schweitzer, M. Hammer, J. Kraft, E. Thamm, E. Konigsdorffer, and J. Strobel, "In vivo measurement of the oxygen saturation of retinal vessels in healthy volunteers," *IEEE Transactions on Biomedical Engineering* **46**(12), 1454-1465 (1999).
140. S. Palkovits, M. Lasta, R. Told, D. Schmidl, A. Boltz, K. J. Napora, R. M. Werkmeister, A. Popa-Cherecheanu, G. Garhöfer, and L. Schmetterer, "Retinal Oxygen Metabolism

- During Normoxia and Hyperoxia in Healthy Subjects Retinal Oxygen Metabolism in Humans," *Investigative Ophthalmology & Visual Science* **55**(8), 4707-4713 (2014).
141. M. Hammer, W. Vilser, T. Riemer, F. Liemt, S. Jentsch, J. Dawczynski, and D. Schweitzer, "Retinal Venous Oxygen Saturation Increases by Flicker Light Stimulation," *Investigative Ophthalmology & Visual Science* **52**(1), 274-277 (2011).
 142. K. Polak, L. Schmetterer, and C. E. Riva, "Influence of Flicker Frequency on Flicker-Induced Changes of Retinal Vessel Diameter," *Investigative Ophthalmology & Visual Science* **43**(8), 2721-2726 (2002).
 143. S. Wang, G. Birol, E. Budzynski, R. Flynn, and R. A. Linsenmeier, "Metabolic Responses to Light in Monkey Photoreceptors," *Current Eye Research* **35**(6), 510-518 (2010).
 144. R. D. Braun, R. A. Linsenmeier, and T. K. Goldstick, "Oxygen consumption in the inner and outer retina of the cat," *Investigative ophthalmology & visual science* **36**(3), 542-554 (1995).
 145. S. H. Hardarson, S. Basit, T. E. Jonsdottir, T. Eysteinnsson, G. H. Halldorsson, R. A. Karlsson, J. M. Beach, J. A. Benediktsson, and E. Stefansson, "Oxygen Saturation in Human Retinal Vessels Is Higher in Dark Than in Light," *Investigative Ophthalmology & Visual Science* **50**(5), 2308-2311 (2009).
 146. W. Drexler and J. G. Fujimoto, *Optical coherence tomography: technology and applications* (Springer Science & Business Media, 2008).
 147. S. P. Chong, C. W. Merkle, C. Leahy, and V. J. Srinivasan, "Cerebral metabolic rate of oxygen (CMRO₂) assessed by combined Doppler and spectroscopic OCT," *Biomed. Opt. Express* **6**(10), 3941-3951 (2015).
 148. R. K. Wang, S. L. Jacques, Z. Ma, S. Hurst, S. R. Hanson, and A. Gruber, "Three dimensional optical angiography," *Opt. Express* **15**(7), 4083-4097 (2007).
 149. U. Dirnagl, C. Iadecola, and M. A. Moskowitz, "Pathobiology of ischaemic stroke: an integrated view," *Trends in neurosciences* **22**(9), 391-397 (1999).
 150. K. P. Doyle, R. P. Simon, and M. P. Stenzel-Poore, "Mechanisms of ischemic brain damage," *Neuropharmacology* **55**(3), 310-318 (2008).
 151. B. C. White, J. M. Sullivan, D. J. DeGracia, B. J. O'Neil, R. W. Neumar, L. I. Grossman, J. A. Rafols, and G. S. Krause, "Brain ischemia and reperfusion: molecular mechanisms of neuronal injury," *Journal of the Neurological Sciences* **179**(1-2), 1-33 (2000).
 152. L. Hertz, "Bioenergetics of cerebral ischemia: A cellular perspective," *Neuropharmacology* **55**(3), 289-309 (2008).
 153. M. A. Moskowitz, E. H. Lo, and C. Iadecola, "The Science of Stroke: Mechanisms in Search of Treatments," *Neuron* **67**(2), 181-198 (2010).
 154. R. D. Frostig, E. E. Lieke, D. Y. Ts'o, and A. Grinvald, "Cortical functional architecture and local coupling between neuronal activity and the microcirculation revealed by in vivo high-resolution optical imaging of intrinsic signals," *Proceedings of the National Academy of Sciences* **87**(16), 6082-6086 (1990).
 155. S. Hu, K. Maslov, V. Tsytsarev, and L. V. Wang, "Functional transcranial brain imaging by optical-resolution photoacoustic microscopy," *Journal of Biomedical Optics* **14**(4), 040503-040503-040503 (2009).
 156. M. B. Bouchard, V. Voleti, C. S. Mendes, C. Lacefield, W. B. Grueber, R. S. Mann, R. M. Bruno, and E. M. C. Hillman, "Swept confocally-aligned planar excitation (SCAPE)

- microscopy for high-speed volumetric imaging of behaving organisms," *Nat Photon* **9**(2), 113-119 (2015).
157. M. A. Yaseen, V. J. Srinivasan, I. Gorczynska, J. G. Fujimoto, D. A. Boas, and S. Sakadžić, "Multimodal optical imaging system for in vivo investigation of cerebral oxygen delivery and energy metabolism," *Biomed. Opt. Express* **6**(12), 4994-5007 (2015).
 158. A. Y. Shih, J. D. Driscoll, P. J. Drew, N. Nishimura, C. B. Schaffer, and D. Kleinfeld, "Two-Photon Microscopy as a Tool to Study Blood Flow and Neurovascular Coupling in the Rodent Brain," *Journal of Cerebral Blood Flow & Metabolism* **32**(7), 1277-1309 (2012).
 159. S. Sakadžić, J. Lee, D. A. Boas, and C. Ayata, "High-resolution in vivo optical imaging of stroke injury and repair," *Brain Research* **1623**(174-192 (2015).
 160. S. Sakadzic, E. Roussakis, M. A. Yaseen, E. T. Mandeville, V. J. Srinivasan, K. Arai, S. Ruvinskaya, A. Devor, E. H. Lo, S. A. Vinogradov, and D. A. Boas, "Two-photon high-resolution measurement of partial pressure of oxygen in cerebral vasculature and tissue," *Nat Meth* **7**(9), 755-759 (2010).
 161. U. Dirnagl, B. Kaplan, M. Jacewicz, and W. Pulsinelli, "Continuous Measurement of Cerebral Cortical Blood Flow by Laser-Doppler Flowmetry in a Rat Stroke Model," *J Cereb Blood Flow Metab* **9**(5), 589-596 (1989).
 162. R. U. Maheswari, H. Takaoka, H. Kadono, R. Homma, and M. Tanifuji, "Novel functional imaging technique from brain surface with optical coherence tomography enabling visualization of depth resolved functional structure in vivo," *Journal of Neuroscience Methods* **124**(1), 83-92 (2003).
 163. Y. Chen, A. D. Aguirre, L. Ruvinskaya, A. Devor, D. A. Boas, and J. G. Fujimoto, "Optical coherence tomography (OCT) reveals depth-resolved dynamics during functional brain activation," *Journal of Neuroscience Methods* **178**(1), 162-173 (2009).
 164. B. D. Watson, W. D. Dietrich, R. Busto, M. S. Wachtel, and M. D. Ginsberg, "Induction of reproducible brain infarction by photochemically initiated thrombosis," *Annals of Neurology* **17**(5), 497-504 (1985).
 165. M. Schroeter, S. Jander, and G. Stoll, "Non-invasive induction of focal cerebral ischemia in mice by photothrombosis of cortical microvessels: characterization of inflammatory responses," *Journal of Neuroscience Methods* **117**(1), 43-49 (2002).
 166. M. Ginsberg and R. Busto, "Rodent models of cerebral ischemia," *Stroke* **20**(12), 1627-1642 (1989).
 167. N. Lue, J. Bewersdorf, M. D. Lessard, K. Badizadegan, R. R. Dasari, M. S. Feld, and G. Popescu, "Tissue refractometry using Hilbert phase microscopy," *Opt. Lett.* **32**(24), 3522-3524 (2007).
 168. M. Wojtkowski, R. Leitgeb, A. Kowalczyk, T. Bajraszewski, and A. F. Fercher, "In vivo human retinal imaging by Fourier domain optical coherence tomography," *Journal of Biomedical Optics* **7**(3), 457-463 (2002).
 169. M. Wojtkowski, V. J. Srinivasan, T. H. Ko, J. G. Fujimoto, A. Kowalczyk, and J. S. Duker, "Ultrahigh-resolution, high-speed, Fourier domain optical coherence tomography and methods for dispersion compensation," *Opt. Express* **12**(11), 2404-2422 (2004).
 170. M. Guizar-Sicairos, S. T. Thurman, and J. R. Fienup, "Efficient subpixel image registration algorithms," *Opt. Lett.* **33**(2), 156-158 (2008).
 171. S. Sakadžić, E. T. Mandeville, L. Gagnon, J. J. Musacchia, M. A. Yaseen, M. A. Yucel, J. Lefebvre, F. Lesage, A. M. Dale, K. Eikermann-Haerter, C. Ayata, V. J. Srinivasan, E. H.

- Lo, A. Devor, and D. A. Boas, "Large arteriolar component of oxygen delivery implies a safe margin of oxygen supply to cerebral tissue," *Nat Commun* **5**((2014).
172. C. D. Klaassen, "Pharmacokinetics of rose bengal in the rat, rabbit, dog, and guinea pig," *Toxicology and applied pharmacology* **38**(1), 85-100 (1976).
173. A. Y. Shih, B. Friedman, P. K. Drew, P. S. Tsai, P. D. Lyden, and D. Kleinfeld, "Active Dilation of Penetrating Arterioles Restores Red Blood Cell Flux to Penumbral Neocortex after Focal Stroke," *Journal of Cerebral Blood Flow & Metabolism* **29**(4), 738-751 (2009).
174. M. Ishikawa, E. Sekizuka, C. Oshio, S. Sato, N. Yamaguchi, S. Terao, K. Tsukada, H. Minamitani, and T. Kawase, "Platelet adhesion and arteriolar dilation in the photothrombosis: observation with the rat closed cranial and spinal windows," *Journal of the Neurological Sciences* **194**(1), 59-69 (2002).
175. A. G. TSAI, P. C. JOHNSON, and M. INTAGLIETTA, "Oxygen Gradients in the Microcirculation," *Physiological Reviews* **83**(3), 933-963 (2003).
176. P. Moftakhar, J. S. Hauptman, D. Malkasian, and N. A. Martin, "Cerebral arteriovenous malformations. Part 2: physiology," *Neurosurgical focus* **26**(5), E11 (2009).
177. K. Masamoto, N. Takizawa, H. Kobayashi, K. Oka, and K. Tanishita, "Dual responses of tissue partial pressure of oxygen after functional stimulation in rat somatosensory cortex," *Brain Research* **979**(1-2), 104-113 (2003).
178. J. Kur, E. A. Newman, and T. Chan-Ling, "Cellular and physiological mechanisms underlying blood flow regulation in the retina choroid in health disease," *Progress in retinal and eye research* **31**(5), 377-406 (2012).
179. P.-y. Teng, J. Wanek, N. P. Blair, and M. Shahidi, "Response of Inner Retinal Oxygen Extraction Fraction to Light Flicker Under Normoxia and Hypoxia in Rat," *Investigative Ophthalmology & Visual Science* **55**(9), 6055-6058 (2014).
180. E. A. Newman, "Functional hyperemia and mechanisms of neurovascular coupling in the retinal vasculature," *Journal of Cerebral Blood Flow & Metabolism* **33**(11), 1685-1695 (2013).
181. C. E. Riva, E. Logean, B. L. Petrig, and B. Falsini, "Effect of dark adaptation on retinal blood flow," *Klin Monbl Augenheilkd* **216**(5), 309-310 (2000).
182. M. S. Mahmud, D. W. Cadotte, B. Vuong, C. Sun, T. W. H. Luk, A. Mariampillai, and V. X. D. Yang, "Review of speckle and phase variance optical coherence tomography to visualize microvascular networks," *Journal of Biomedical Optics* **18**(5), 050901-050901 (2013).

Appendix A

Maximum permissible exposures for ocular safety of OCT systems using broad-band visible light illumination, calculated based on ANSI Z136.1-2000 standard

Currently, there is no laser safety criteria regarding the use of visible light illumination in OCT systems. This chapter seek to provide an insight on the maximum permissible exposure to visible light during regular OCT scans. The calculation presented follows the guideline published by Delori *et al* in 2007 regarding the maximum permissible light exposure for ocular safety, which emphasis on its implication in ophthalmic imaging devices. The guideline itself is based upon the American National Standards Institute (ANSI) Z136.1-2000 standard. All reference listed in this chapter refer to the original publication.

There is no direct method to evaluate the potential hazard from the retinal exposure of OCT, or any ophthalmic imaging devices using scanning laser scheme. Approximation must be made before applying the established ANSI standard. The most straightforward and strict limitation requires that the static laser beam without scanning satisfy the power limitation for class I lasers. Though this is the simplest approach to ensure laser safety, it also has little practical use due to the detection sensitivity limitations. Thus, most laser scanning ophthalmic imaging devices exceed this limit, and thus requires constant moving of the laser spot to ensure safety. Two scenarios are commonly used to approximate the light exposure of OCT. The lowest maximum permissible

beam power (MP Φ) of either model is chosen as the overall MP Φ for visible light exposure during OCT.

Throughout the calculation, the scanning parameters of the visible light OCT (vis-OCT) obeys the following assumptions:

1. The scanning field on the retina is square. To be conservative, the smaller visual field of $10^\circ \times 10^\circ$, or $175 \text{ mrad} \times 175 \text{ mrad}$, is used. Thus, the visual angle of the side, $\alpha_F = 175 \text{ mrad}$.
2. The scanning rate is F frame per second (FPS), which ranges from 0.1 to 10 FPS. Each frame has R horizontal lines, which ranges from 16 to 512 depending specific acquisition requirements. Thus during the following calculation, the combination that yield the lowest MP Φ is chosen to ensure safety.
3. The total exposure duration is T seconds. Two values is chosen for T to corresponding the regular safety limit and worst case scenario. $T = 300 \text{ s}$ (5 mins) represents a realistic duration for most clinical and experimental situations. And $T = 28800 \text{ s}$ (8 hours) represent a worst case scenario for continuous viewing of the scanning beam for an entire work day.

The first scenario, and also the most commonly used one, is to use continuous wave (CW) approximation to model the entire exposure filed. It assume that the laser illumination is uniformly distributed over the entire visual filed. Thus, CW limit can be applied to calculate the thermal and photoacoustic limits using the following formula,

$$\text{MP}\Phi = 6.93 \times 10^{-4} C_T C_E P^{-1} t^{-0.25}, \quad (\text{A.1})$$

when exposure duration t is between 0.07 s and 10000 s, or

$$\text{MP}\Phi = 6.93 \times 10^{-5} C_T C_E P^{-1}, \quad (\text{A.2})$$

For exposure above 10000 s.

For visible light range, $C_T = 1$. C_E is a function of view angle. For $\alpha_F > 100$ mrad, $C_E = \frac{4\alpha_F^2}{\pi\alpha_{min}\alpha_{max}}$, where $\alpha_{min} = 1.5$ mrad and $\alpha_{max} = 100$ mrad are two constants determined by the optics and motion of the eye. In the case the subject underwent pupil dilation, pupil factor $P = 1$. Thus, the MP Φ for 5 mins exposure is 0.0433 W, and 0.0180 W for long term exposure.

Similarly, the photochemical limit is given by

$$\text{MP}\Phi = 5.56 \times 10^{-6} C_B \left(\frac{4}{\pi} \alpha_F^2 \right) t^{-1} \quad (\text{A.3})$$

for 5 mins exposure time, and

$$\text{MP}\Phi = 5.56 \times 10^{-10} C_B \left(\frac{4}{\pi} \alpha_F^2 \right) \quad (\text{A.4})$$

for long term exposures. The coefficient C_B is a wavelength (λ) dependent function, had have the following expression within the visible spectrum range,

$$C_B = 10^{0.020(\lambda-450)}. \quad (\text{A.5})$$

The lower limit for C_B is 1, and is chosen for both expressions. Thus, the photochemical limit is calculated to be 0.0723 W for a 5-min duration and 0.0022 W for long term exposure.

The second scenario more closely mimics the raster scanning process during vis-OCT imaging. As the beam scans across, the exposure is similar to that from a pulsed rectangular beam. The angular width of the rectangular is α_{min} ; the angular length of the raster scan line is $\alpha_s =$

$\min\{\alpha_F, \alpha_F F R t_{min}\}$, where t_{min} is the thermal confinement duration, for visible light, its value is 18×10^{-6} s. The smallest α_s possible in the vis-OCT pattern is thus 0.1613 mrad. Note that this angular length is smaller than α_F , indicating $t = t_{min}$. In addition, it is smaller than α_{min} , so $C_E = 1$ in this case.

The first rule protects against cumulative photochemical damage mechanism. It tests the safety of a continuous-wave equivalent exposure of duration t near the limit of t_{min} ,

$$MP\Phi = 6.93 \times 10^{-4} C_T C_E t^{-0.25} \quad (A.6)$$

for t slight above t_{min} ; and

$$MP\Phi = 1.93 \times 10^{-7} C_T C_J C_E t^{-1} \quad (A.7)$$

for t slightly below t_{min} . For visible light C_T and C_J are both 1. The lower limit is calculated to be 0.0106 W.

There is also a second rule to protect against subthreshold pulse-cumulative thermal injury and applies only to the thermal limits,

$$MP\Phi = \frac{MP\Phi_{av}}{\delta} = n^{-0.25} \frac{\delta^*}{\delta} 6.93 \times 10^{-4} C_T C_E t^{-0.25} \quad (A.8)$$

where δ and δ^* are duty factors and both equal to $F t_{min}$. $n = FT$ is the number of pulses. Thus, this limit ranges from 0.0045 W for 5 mins exposure and 0.0015 W for 8 hour exposure.

The last rule has the lowest $MP\Phi$. Thus, it is established that 0.0045 W is the safety limit for regular examination. For long term exposure, the safety power limit is 0.0015 W.

Vita

Personal information

Name: Siyu Chen
Date of Birth: September 10, 1989
Place of Birth: Shanghai, China

Education

BS, Biomedical Engineering, Shanghai Jiao Tong University (CN), 2008

PhD, Biomedical Engineering, Northwestern University (US), expected in June 2017

Patent list

1. Yi, J., **Chen, S.**, Zhang, H.F., Method of retinal vascular imaging, US provisional patent filed (2015).

Peer reviewed journal publications (* Equal contribution)

1. **Chen, S.**, Shu, X., Nesper, P.L., Liu, W., Fawzi, A.A., Zhang, H.F. (2017), Retinal oximetry in humans using visible-light optical coherence tomography [INVITED], Biomedical Optics Express 8(3), 1415-1429.

2. Liu, R., **Chen, S.**, Spicer, G., Zhang, H.F., Yi, J., & Backman V. (2017) A theoretical model for optical oximetry at the single-cell level: exploring hemoglobin oxygen saturation through backscattering of single red blood cells, *Journal of Biomedical Optics* 22(2), 025002.
3. Liu, W., Wang, S., Yi, J., Zhang, K., Chen, S., Sorenson, C.M., Sheibani, N. & Zhang H.F. (2017) Increased inner retinal oxygen metabolism precedes microvascular alterations in rodent model with Type 1 diabetes, *Investigative Ophthalmology & Vision Science* 58(2), 981-989.
4. Xiao, J., **Chen, S.**, Yi J., Zhang, H.F. & Guillermo A.A. (2017) A cooperative copper metal–organic framework-hydrogel system improves wound healing in diabetes, *Advanced Functional Materials* 27(1), 1604872.
5. Dong, B., **Chen, S.**, Zhou, F., Chan, C., Yi, J., Zhang, H.F. & Sun, C. (2016) Real-time functional analysis of inertial microfluidic devices via spectral-domain optical coherence tomography, *Scientific Reports* 6, 33250.
6. **Chen, S.**, Liu, Q., Shu, X., Soetikno, B., Tong, S. & Zhang, H.F. (2016) Imaging hemodynamic response after ischemia stroke in mouse cortex using visible-light optical coherence tomography, *Biomedical Optics Express* 7(9), 3377-3389.
7. Zhu, Y., Hoshi, R., **Chen, S.**, Yi, J., Duan, C., Galiano, R., Zhang, H.F., & Ammer, G.A. (2016) Sustained release of stromal cell derived factor-1 from an antioxidant thermoresponsive hydrogel enhances dermal wound healing in diabetes, *Journal of Controlled Release* 238(28), 114-122.

8. **Chen, S.**, Shu, X., Yi, J., Fawzi, A.A. & Zhang, H.F. (2016) Dual-band optical coherence tomography using a single supercontinuum laser source, *Journal of Biomedical Optics* 21(6), 066013.
9. Yi, J., **Chen, S.** *, Shu, X., Fawzi, A.A. & Zhang, H.F. (2015) Human retinal imaging using visible-light optical coherence tomography guided by scanning laser ophthalmoscopy, *Biomedical Optics Express* 6(1), 3701-3713.
10. Liu, W., Yi, J., **Chen, S.**, Jiao, S. & Zhang, H.F. (2015), Measuring retinal blood flow in rats using Doppler optical coherence tomography without knowing eyeball axial length, *Medical Physics* 42, 5356-5362.
11. **Chen, S.**, Yi, J. & Zhang, H.F. (2015) Measuring oxygen saturation in retinal and choroidal circulations in rats using visible light optical coherence tomography angiography, *Biomedical Optics Express* 6(8), 2840-2853.
12. Yi, J., Liu, W., **Chen, S.**, Backman, V., Sheibani, N., Sorenson, C., Fawzi, A.A., Linsenmeier R.A. & Zhang, H.F. (2015). Visible light optical coherence tomography measures retinal oxygen metabolic response to systemic oxygenation, *Light: Science & Applications* 4, e334.
13. **Chen, S.**, Yi, J., Liu, W., Backman, V. & Zhang, H.F. (2015). Monte Carlo investigation of optical coherence tomography retinal oximetry, *IEEE Transactions on Biomedical Engineering* 62(9), 2308-2315.
14. Urban, B.E., Yi, J., **Chen, S.***, Dong, B., Zhu, Y., DeVries, S.H., Backman, V. & Zhang, H.F. (2015). Super-resolution two-photon microscopy via scanning patterned illumination, *Physical Review E* 91(4), 042703.

15. Dong, B., Li, H., Zhang, Z., Zhang, K., **Chen, S.**, Sun, C. & Zhang, H.F. (2015). 'Isometric multimodal photoacoustic microscopy based on optically transparent micro-ring ultrasonic detection, *Optica* 2(2), 169-176.
16. **Chen, S.**, Yi, J., Dong, B., Sun, C., Kiser, P., Hope, T.J. & Zhang, H.F. (2014). Imaging endocervical mucus anatomy and dynamics in macaque female reproductive track using optical coherence tomography, *Quantitative Imaging in Medicine and Surgery* 5(1), 40-45.
17. Yi, J., **Chen, S.**, Backman, V. & Zhang, H.F. (2014). *In vivo* functional microangiography by visible-light optical coherence tomography, *Biomedical Optics Express*, 5(1), 3603-3612.
18. Dong, B., **Chen, S.**, Zhang, Z., Sun, C. & Zhang, H.F. (2014). Photoacoustic probe using a micro-ring resonator ultrasonic sensor for endoscopic applications, *Optics Letters*, 39(15), 4372-4375.

Conference presentations

1. "Monitoring mouse cerebral circulation oxygenation after ischemic stroke using visible-light optical coherence tomography", OSA Biophotonics Congress: Optics in the Life Sciences, San Diego, CA, USA (2017)
2. "Imaging ischemic strokes in rodents using visible-light optical coherence tomography", SPIE Photonics West, San Francisco, CA, USA (2017).
3. "Dual-band optical coherence tomography using a single supercontinuum laser source", ARVO annual meeting, Seattle, WA, USA (2016).

4. “Measuring oxygen saturation in retinal and choroidal circulations in rats using visible light optical coherence tomography angiography”, SPIE Photonics West, San Francisco, CA, USA (2016).
5. “Dynamically measuring retinal oxygen saturation at microvascular level using visible-light OCT angiograph”, ARVO annual meeting, Denver, CO, USA (2015).
6. “Measuring absolute microvascular blood flow in cortex using visible-light optical coherence tomography”, IEEE Engineering in Medicine and Biology Society annual international conference (EMBC), Chicago, IL, USA (2014).
7. “Photoacoustic endoscope using a micro-ring resonator ultrasonic sensor”, SPIE Photonics West, San Francisco, CA, USA (2014).